Chapter 7
Nucleation, Growth, and Aggregation of Mineral Phases: Mechanisms and Kinetic Controls

Liane G. Benning[1] and Glenn A. Waychunas[2]

7.1 Introduction

The formation of any phase, whether natural or synthetic (Fig. 7.1), is usually a disequilibrium process that follows a series of steps until a thermodynamically stable state (equilibrium) is achieved. The first step in the process of creating a new solid phase from a supersaturated solution (either aqueous or solid) is called nucleation. A particle formed by the event of nucleation usually has a poorly ordered and often highly hydrated structure. This particle is metastable with respect to ordering into a well-defined phase, which can accompany growth of the particle. This process of initiation of a new phase is defined as a first order transition and can follow various pathways involving a host of mechanisms. One of these pathways occurs when individual nuclei coalesce into larger clusters, a process defined as aggregation, which itself can follow a series of different pathways. The new phase is thermodynamically defined when the growing nucleus or aggregate has distinct properties relative to its host matrix; for example, a well-defined crystal structure, composition and/or density. These processes depend on a plethora of chemical and physical parameters that control and strongly affect the formation of new nuclei, the growth of a new crystal, or the aggregation behavior of clusters, and it is these issues that will be the focus of this chapter. We will discuss the mechanisms and rates of each process as well as the methods of quantification or modeling from the point of view of existing theoretical understanding. Each step will be illustrated with natural examples or laboratory experimental quantifications. Complementary to the information in this chapter, a detailed analysis of the mechanisms and processes that govern dissolution of a phase are discussed in detail in Chap. 5 and more detailed information about molecular modeling approaches are outlined in Chap. 2.

[1] University of Leeds, Earth and Biosphere Institute, School of Earth and Environment, liane@earth.leeds.ac.uk
[2] Lawrence Berkeley National Laboratory, Molecular Geochemistry and Nanogeoscience Group, Geochemistry Department, Earth Sciences Division, Waychunas@lbl.gov

Fig. 7.1 Crystals formed in natural and laboratory settings; (**a**) ice crystals grown on a glass window (Benning unpublished image) and (**b**) hexagonal pyrrhotite platelets grown from an iron sulphide precursor at 200° C; the growth followed a solid state process (see also Hunger and Benning, 2007; image Benning, unpublished, the copyright for the colour image (b) in the online version of this chapter is copyrighted to Eric Condliffe, Leeds)

7.2 Nucleation

Nucleation is the process by which small clusters of a new phase are initiated. The stability of any phase is usually the realm of equilibrium thermodynamics because any phase that is stable under given pressure and temperature conditions at a minimum energy state for infinite time periods is considered at equilibrium. In contrast, here we concentrate on how deviations from equilibrium drive the formation of a new phase from nucleation at the atomic or molecular level all the way to achieving a stable state at some larger growth stage.

In any system, equilibrium is attained when the exchange of heat or mass between initial and end product is approaching zero. The degree to which the process in question departs from this equilibrium state corresponds to the driving force that initiates nucleation of a new phase. When a new phase is forming in solution, this driving force is related to the deviation from saturation state of the system or the difference in chemical potential between the solution and the newly formed phase. This can be expressed as:

$$\Delta\mu_{\mathrm{I}} = \mu_{\mathrm{I,n}} - \mu_{\mathrm{I,s}} \tag{7.1}$$

which describes the difference in chemical potential between $\mu_{\mathrm{I,n}}$ (the chemical potential of component I in the nucleating phase) and $\mu_{\mathrm{I,s}}$ (the chemical potential of component I in the nucleating solution). Nucleation occurs when overall free energy is reduced because part of the system is transformed from a higher to a lower free energy state, and thus when $\Delta\mu_{\mathrm{I}} < 0$ nucleation and growth is favored. A general formula for the driving force is given by:

$$\Delta\mu(a,\mathrm{T}) = \mathrm{k}_B\mathrm{T}\ln[a/a_e(\mathrm{T})] = \mathrm{k}_B\mathrm{T}\ \ln\ \mathrm{S_R} \tag{7.2}$$

where k_B is the Boltzmann constant, T is the absolute temperature and $\mathrm{S_R}$ is the solute supersaturation ratio ($\mathrm{S_R} = a_{(e)}/a$, where $a_{(e)}$ is the activity at equilibrium and a the activity during nucleation and growth).

7.2.1 Classical Nucleation Theory (CNT)

There are two main conditions where nucleation processes can be evaluated: (a) under conditions where the host phase is nearly at equilibrium with the nuclei, and (b) under conditions where the host phase is very distant in stability from the nuclei. The former case is the basis for the Classical Nucleation Theory (CNT), which we will discuss first. CNT includes treatments of nucleation from a purely thermodynamic or statistical mechanics formalism, or via so-called kinetic theories. The latter are generally better equipped to handle dynamic phenomena, such as nucleation rates, and allow some problematic aspects of pure thermodynamics based CNT to be overcome. However, the pure thermodynamic formalisms are useful as both

a starting point for theory development and as a useful tool for gaining insight into these transformation processes.

Nucleation theory began with the work of Volmer and Weber (1925), Farkas (1927), and Becker and Doring (1935), all treating liquid droplet condensation from a saturated gas. Somewhat more generalized treatments were subsequently developed by Zeldovich (1943), Frenkel (1939, 1955), Turnbull and Fisher (1949), and Turnbull (1950, 1956). These workers largely considered *homogeneous* nucleation, i.e., initiation of the new phase within the bulk of the solution or matrix with the only energetic conditions being the host and nucleus volume free energy and the interfacial free energy between host and nucleus. Although homogeneous nucleation is rare in geochemical systems, it is a good starting point for the introduction of nucleation, growth parameters and theory. CNT makes the assumption that nuclei that are formed have the same properties as their analogous bulk phase. This allows the free energy of the nucleus to be estimated as a sum of the bulk and surface free energies depending only on volume and area, respectively, and not on radius, a concept known as the capillarity approximation. Though these assumptions are not accurate on the molecular level (Talanquer and Oxtoby, 1994; Oxtoby, 1992), because nano-sized particles often do not behave like bulk analogs, and their surface energy is dependent on the radius of curvature, nevertheless these assumptions allow for a reasonably accurate analysis.

7.2.1.1 Equilibrium Thermodynamic Analysis

Overall, the total free energy of nucleation, ΔG, can be viewed as the sum of the energy used up in forming a particle by condensation of atoms, $-\Delta G_P$, which is proportional to r^3, and the energy gained by creating the particles surface ΔG_S, which is proportional to r^2. Figure 7.2a shows the free energy versus radius for incipient nuclei. The total free energy of nucleation, ΔG, can thus be expressed as:

$$\Delta G = [4/3\pi r^3 \Delta g] + [4\pi r^2 \sigma], \tag{7.3}$$

where r is the nucleus radius, Δg is the free energy change per unit volume of nucleus, and σ is the free energy per unit area of the nucleus interface.

The free energy of the nucleus is less than that of the corresponding matrix, and thus Δg is negative. There is thus a crossover point where the free energy change added by creation of the nucleus begins to decrease, and this corresponds to the critical nucleus radius. For any growth beyond this point the free energy decreases and growth is progressively more favored. If the derivative $\partial(\Delta G)/\partial r = 0$ is evaluated for Eq. (7.3), we obtain the free energy for the homogeneous critical nucleus formation:

$$\Delta G_{homo} = 16\pi\sigma^3/3(\Delta g)^2 \tag{7.4a}$$

and the critical nucleus radius,

$$r_{homo} = -2\sigma/\Delta g \tag{7.4b}$$

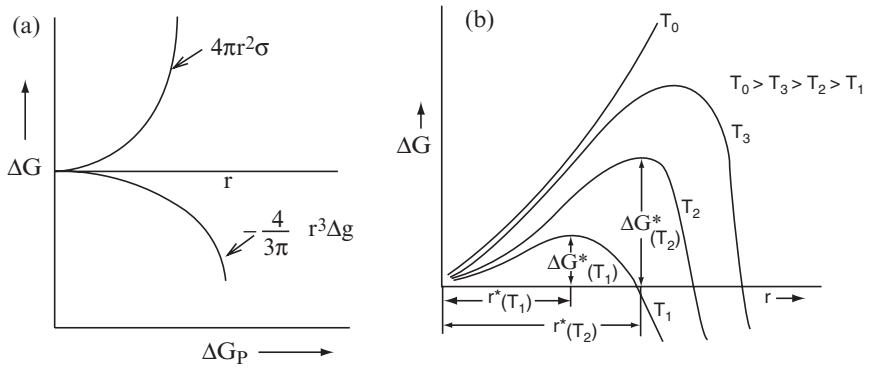

Fig. 7.2 Free energy of a cluster of atoms as a function of radius; (**a**) two main components of energy change in forming a cluster are defined: upper curve is surface free energy due to solid–liquid interfacial energy σ which increases with radius; lower curve is volume free energy that decreases with radius as the nucleation phase is more stable than the matrix and Δg is the difference in volume free energy between matrix and nucleus. (**b**) Sum of total free energy change at different temperatures as a function of radius. The "critical nucleus" free energy is ΔG^*. A larger nucleus is needed for stability at higher temperatures, or conversely nuclei formed at T_1 will cross into instability at T_2

Therefore, the critical energy of nucleation is governed by the magnitude of the free energy at the interface and the driving force. Usually, the smaller this critical energy the easier nucleation can occur. Figure 7.2b shows the effects of temperature on the critical nucleus size. As temperature increases there is less difference in the energy per unit volume of nucleus versus the matrix, thus the nuclei will have to grow larger in size before reaching stability. At some high temperature no nuclei of any size will be stable. This type of behavior can be looked upon as decreasing degrees of supersaturation as temperature increases.

The nucleation rate for such a CNT system can be determined by assuming that a single atom added to the subcritical size nucleus will result in a stable cluster. It is then possible to estimate the number of such subcritical nuclei by using Maxwell–Boltzmann statistics. Given a total number of atoms N_T, the number of critical nuclei can be expressed as:

$$N = N_T \exp(-\Delta G/k_B T) \tag{7.5}$$

Given that the largest subcritical nucleus is surrounded by *s* atoms in the matrix, and that the frequency of lattice vibrations (in a solid) or positional jumps (in a gas or liquid) is $\nu_{<\square\square>}$, then the frequency for which any of these can join the nucleus is:

$$\nu_j = s\nu \exp(-\Delta G_d/k_B T) \tag{7.6}$$

with G_d being the free energy of diffusion across the nucleus/matrix interface and $\nu < \square\square >$ the molar volume of the nucleus. This formulation allows one to include time in the nucleation equation, and hence the normalized homogeneous nucleation

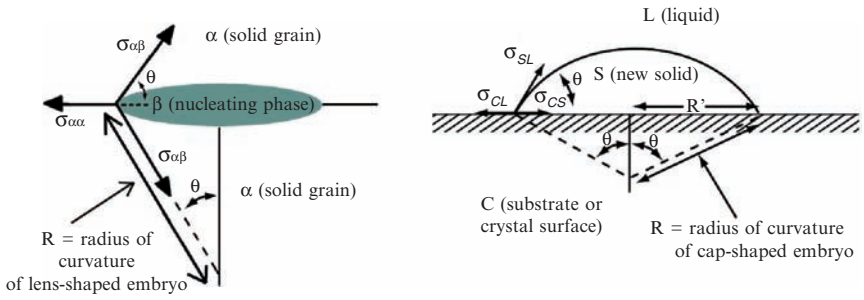

Fig. 7.3 Model geometries for idealized nucleation at grain boundaries (left), and at the solid–water interface (right). In the grain boundary case the nucleus (phase β) is lens-shaped and has all solid–solid interfaces, with the matrix being phase α. The contact angle, θ, is dictated by the surface energy $\sigma_{\alpha\beta}$. At the solid–water interface the nucleus (phase S) is a half-lens with different surface areas contacting the liquid (phase L) and solid (phase C) interfaces. In this case there are three different interface energies to consider, σ_{CL}, σ_{CS} and σ_{SL}

rate, I_{homo}, can be deduced (Raghaven and Cohen, 1975):

$$I_{homo} = N_T s \nu_j \exp[-(\Delta G + \Delta G_d)/k_B T] \tag{7.7}$$

7.2.1.2 Heterogeneous Nucleation

In this volume, some aspects of the formation of new phases on mineral surfaces is discussed in Chap. 3. Nucleation on a surface, usually at defect sites and other regions where the energetics differ from the bulk matrix, is termed heterogeneous nucleation. For the homogeneous nucleation rate discussed above we can devise an analogous heterogeneous nucleation free energy diagram and nucleation rate. Figure 7.3 shows the situation for nucleation at a grain boundary (Clemm and Fisher, 1955), and nucleation on a mineral surface in contact with supersaturated aqueous solutions. These are two important cases for geochemical heterogeneous nucleation, with the former important for metamorphic systems, and the latter for aqueous systems. The key issue is that nucleus growth progressively removes boundary area at the interface of one grain with another. For nucleation from aqueous solution onto a surface, the analogous situation is removal of the surface-solution interface. Intuitively, nucleation in such cases is identical to homogeneous nucleation, except that it includes removal of an interface, and thus must lower the energy of the system more than a homogeneous nucleation event. Hence the energy barrier to nucleation must be reduced.

Heterogeneous nucleation may result in different spatial distributions depending on the shape of the solid–liquid interface. For a spherical or lens shaped interface, nucleation (and/or growth) will progress in three dimensions, while in the case of a disk shaped interface usually the height of the disc remains constant and two dimensional nucleation (and/or growth) takes place. In general it is considered that one-dimensional nucleation does not exist in the realm of heterogeneous nucleation.

However, in the literature 1D nucleation is often invoked when dealing with polymerization and it is described in terms of successive monomer addition. Below we discuss in more detail the case for heterogeneous nucleation on a planar surface and show how the nucleation rate can be derived based on geometrical and energetic considerations.

In Fig. 7.3, R is the radius of curvature of the spherical/lens shaped surfaces of the nucleus, θ is the included angle of the nucleus edge as controlled by surface tension, $\sigma_{\alpha\beta}$ is the matrix/nucleus interfacial energy, and $\sigma_{\alpha\alpha}$ is the grain boundary interfacial energy. The volume and surface area of a lens-shaped nucleus are thus:

$$V = 2\pi R^3(2 - 3\cos\theta + \cos^3\theta)/3 \tag{7.8a}$$

and

$$S = 4\pi R^2(1 - \cos\theta) \tag{7.8b}$$

respectively.

We note here that the total interfacial energy, $\sigma_{\alpha\alpha} = 2\sigma_{\alpha\beta}\ \cos\theta$, and thus the free energy change on nucleation can be derived:

$$\Delta G_{het} = (2/3\pi R^3\Delta g + 2\pi R^2\sigma_{\alpha\beta})(2 - 3\cos\theta + \cos^3\theta) \tag{7.9}$$

From these equations it is then an easy step towards deriving the free energy of critical nucleus formation:

$$\Delta G = 8\pi\sigma^3_{\alpha\beta}(2 - 3\cos\theta + \cos^3\theta)/3(\Delta g)^2 \tag{7.10}$$

In order to obtain the critical radius, *r*, we need to differentiate by R and thus obtain:

$$r = -2\sigma_{\alpha\beta}(\sin\theta)\Delta g \tag{7.11a}$$

and the critical free energy change:

$$\Delta G_{het} = \Delta G_{homo}(2 - 3\cos\theta + \cos^3\theta)/2 \tag{7.11b}$$

the latter obtained by substituting in the free energy for the homogeneous case. This shows that for small θ angles, and thus small interfacial energies, the heterogeneous free energy change is much smaller than the homogeneous case and the nucleating phase will "smear" out along the grain boundary. For $\theta = 90°$, the energy changes are the same, and we obtain spherical nuclei with lowest surface area in both nucleation models.

For the aqueous interface model (Fig. 7.3, right), the same physical quantities can be substituted into the equations above with a slight variation. Here there are three kinds of interfaces, solid nucleus–liquid, substrate–liquid, and substrate–solid nucleus so the energy equations must include the interface area of the solid nucleus–substrate interface. We introduce slightly different designations here: R is the radius of the circle of substrate whereupon the new nucleus resides, and the interfacial energies for the three interfaces are σ_{SL}, σ_{CL} and σ_{CS}, respectively. We need the area under the nucleus, which is $\pi(R')^2$, and must also note that the nucleus has

half the volume and different surface area compared to the grain-boundary case. As $R' = R\sin\theta$, one can derive the analog of Eq. (7.9) as:

$$\Delta G_{aq-het} = \pi R^3/3(2-3\cos\theta+\cos^3\theta)\Delta g + 2\pi R^2(1-\cos\theta)\sigma_{SL} + \pi R^2\sin^2\theta\ \sigma_{CS} \tag{7.12}$$

and by setting $\partial(\Delta G)/\partial R = 0$ and evaluating as before, we get a critical nucleus:

$$r = -4(1-\cos\theta)\sigma_{SL} + 2\sin^2\theta\sigma_{CS/}(2-3\cos\theta+\cos^3\theta)\Delta g \tag{7.13}$$

This expression indicates the trade off between the various interfacial energies for aqueous solution nucleation. For example, in the case of strong hydrophobic interactions σ_{SL} may be significant and increase critical radii, so that precipitation is suppressed. For strong hydrophilic interactions, θ will tend to be small so that the critical radius approaches that for the grain boundary case.

Alternatively, for the grain-boundary nucleation case we can write the critical free energy change in terms of its volume, V, which turns out to be: $\Delta G_{het} = -(\Delta g)V/2$ (Raghavan and Cohen, 1975). This in turn is independent of the number of grain boundaries being absorbed (e.g., double or triple junctions). To obtain a nucleation rate for a heterogeneous nucleation process, it is subsequently necessary to take account of possible nucleation site densities. Note that in the case of homogeneous nucleation the site density was always 100% because nucleation position was unrestricted. Thus, the nucleation rate can be derived as:

$$I_{het} = \sum N_i\sigma_i\nu_j\exp[-(\Delta G_i + \Delta G_d)/k_BT] \tag{7.14}$$

where N_i is the nucleation site density with respect to the critical nucleation energy ΔG. When we compare the rate for heterogeneous nucleation with the nucleation rate for a homogeneous process (Eq. (7.7)) we observe that the pre-exponential term, $[N_i\sigma_i\nu_j]$ in Eq. (7.12) will be smaller than the equivalent term $[N_Ts\nu_j]$ (see Eq. (7.7)), due to the appearance of the interfacial energy term. However, overall this will be offset by the much smaller nucleation barrier energy in a heterogeneous nucleation reaction.

As we have seen above, an equilibrium CNT model lets us derive conditions for formation of nuclei and rates of formation, despite its neglect of atomistic processes and variations, such as the shape, density, and crystallinity of such nuclei. CNT also neglects the fact that a small cluster will have more surface molecules than "bulk" molecules on a volume-normalized basis and thus the difference in surface energy has to be treated independently of the nucleus size. In addition to the failings in the homogeneous case, our development of equilibrium heterogeneous nucleation neglects important aspects of realistic surfaces, such as steps and terraces, dislocations, and other causes of surface strain, and variations in interface energy, some of which were previously discussed in Chap. 3. Examples of CNT that treat these issues can be found in metallurgical and semiconductor applications (Chernov, 1984; Tiller, 1991, 1992). Heterogeneous nucleation is affected by the periodicity of the nucleating phase and the substrate, and is generally enhanced by good registry such

as in near perfect epitaxial relationships, a matter of extreme importance in the nucleation and growth of semiconductor thin films (Venables et al., 1984), and a matter we return to below. However, in cases of greatly dissimilar substrates and nucleating phases (i.e., organic nuclei on ionic substrates) molecular dipole effects and growth anisotropy appear to outweigh lattice matching (Sarma et al., 1997).

7.2.2 Kinetic Nucleation Theory (KNT)

In order to use an equilibrium CNT model to explain precipitation kinetics, we would require good estimates of the interfacial energies, the density of nucleation sites, and the free energy of critical nucleus formation. While interfacial energies are relatively easy to obtain for bulk phases, this is problematic for small nuclei. Even more of a problem is estimation of the free energy of nucleus formation. The one area where modern technology presents a solution is for the density, and even the topology, of nucleation sites (especially relevant for heterogeneous nucleation). KNT provides a way around requiring good estimates of the free energy change on nucleation. An important aspect of the equilibrium CNT formulation is the absence of explicit treatment of backward reactions in determining the nucleation rate. Once formed, the critical nuclei are considered to be stable. However, the critical size nuclei can also dissolve back into the matrix or solution. Hence instead of only considering the rate at which nuclei form and reach stable sizes, a kinetic theory would include the rates of various nuclei dissolving. In the ideal conceptualization, by using KNT we can simply depend on interaction parameters for individual molecules to predict all of the necessary rate equation coefficients, and these parameters might ideally be estimated by the results of quantum mechanics calculations.

KNT originated from the consideration of a chain reaction of clusters of varying size. A general formulation for KNT is (Volmer, 1939; Toschev, 1973):

$$\frac{dc_i}{dt} = \sum_{k=1}^{M} D_{k->i} c_k - \sum_{k=1}^{M} D_{i->k} c_i, \tag{7.15}$$

where $i = 1, 2, 3, \ldots, M$, and the first and second summations represent the formation and dissolution of clusters c_n, of various sizes n, respectively. The D_n operators represent the probability of an exchange occurring. This is a set of equations which is very bulky to handle, so we can simplify it by considering only "monomer" changes, i.e., clusters that change size by loss or gain of single elements (atoms or molecules). For example:

$$i-1 \underset{D_i^-}{\overset{D_{i-1}^+}{\rightleftharpoons}} i \underset{D_{i+1}^-}{\overset{D_i^+}{\rightleftharpoons}} i+1 \tag{7.16}$$

Thus combining with Eq. (7.15) this leads to the formulation:

$$\frac{dc_i}{dt} = \left(D_{i-1}^+ c_{i-1} + D_{i+1}^- c_{i+1}\right) - \left(D_i^+ c_i + D_i^- c_i\right), \tag{7.17}$$

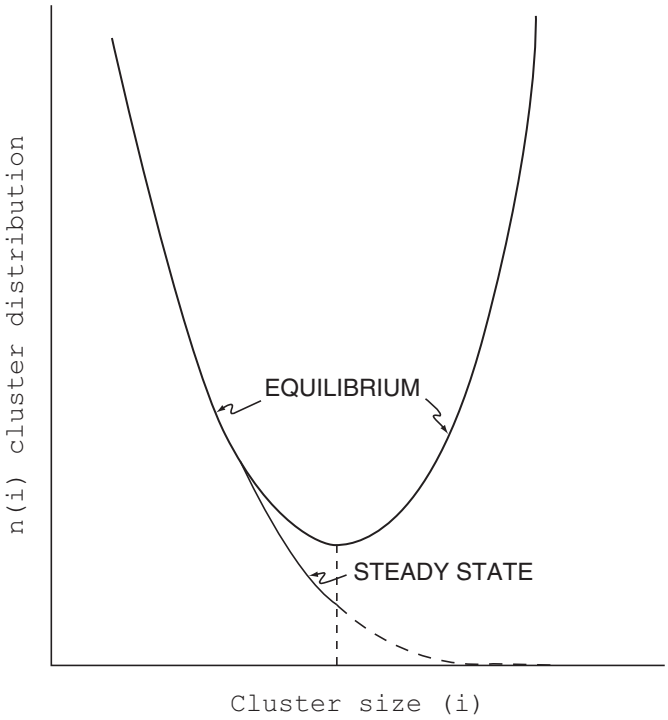

Fig. 7.4 Kinetic theory nucleation rate as a function of normalized cluster size. The critical nucleus is defined here as the cluster size where creation (birth) and dissolution (death) rates are equivalent and no explicit energy is considered. This calculated curve (after Toschev, 1973) is for water nuclei with $i^* = 64$ molecules at 300 K

Au: Please check white boxes here.

where $i = 2,3,\ldots,\ M-1$, with $c_i = 0$ when $M = i$, i.e., the largest clusters are continuously taken out of the system; $D_i^+ = A_i\beta_{<\square\square>}$ and $D_i^- = A_i\alpha_i$, where A_i is the surface area of the i-sized cluster, and $\beta_{<\square\square>}$ and α_i are the numbers of atoms or molecules joining and leaving the cluster per unit time and surface area, respectively. It is useful to consider the ratio $D_i^+/D_i^- = \exp(\frac{\mu^*-\mu_i}{RT})$, where $\mu^* - \mu_i$ is the difference in chemical potential between the critical nucleus and a given cluster as derived by Volmer (1939). For spherical nuclei this can be shown to be equivalent to:

$$\frac{D_i^+}{D_i^-} = \exp\left\{\frac{B}{i^{*1/3}}\left[1-\left(\frac{i^*}{i}\right)^{1/3}\right]\right\} \tag{7.18}$$

where $B = \frac{2\sigma\nu}{RT}N_A^{1/3}(\frac{4\pi}{3\nu})^{1/3}$ with ν being the molar volume of the formed nucleus, N_A the Avogadro's number, and σ the nucleus surface free energy. A plot of this equation (Fig. 7.4) calculated for water droplets shows that subcritical clusters can

only reach the critical size by random fluctuations, rather than grow as might be intuited from equilibrium theory.

The flux of clusters through a given size is:

$$J_i = D^+_{i-1} c_{i-1} - D^-_i c_i. \tag{7.19}$$

Substituting Eq. (7.19) into Eq. (7.17) produces

$$\frac{dc_i}{dt} = J_i - J_{i+1}, \tag{7.20}$$

which represents the rate of flux through a given cluster size. In this terminology, the nucleation rate is equivalent to the flux J_i when the i values considered clusters at the critical cluster size. Two conditions are usually considered, the steady-state nucleation rate, i.e., the case where $\frac{dc_i}{dt} = 0$ (Becker and Doring, 1935) and there is continuous fixed flux of clusters through the various size regimes, and the equilibrium nucleation rate where there is no flux between cluster sizes.

7.2.2.1 Zeldovich-Frenkel Formulation

Zeldovich (1943) and Frenkel (1955) developed equations analogous to Eq. (7.17) and Eq. (7.20), but taking i as a continuous variable. Using the principle of detailed balance (i.e., all elementary reactions must have equal forward and reverse rates at equilibrium) with the relation $D^+(i)n(i) = D^-(i+1)n(i+1)$, where $n(i)$ is the equilibrium distribution function for all clusters i, the dissolution probabilities $D^-(i)$ can be eliminated from the equations. This produces a set of partial differential equations for cluster size evolution in time, and instantaneous fluxes:

$$\frac{dc_{(i,t)}}{dt} = \frac{\partial}{\partial_i}\left\{ D^+(i)n(i)\frac{\partial}{\partial_i}\left[\frac{c(i,t)}{n(i)}\right]\right\} \tag{7.21}$$

$$J(i,t) = -D^+(i)n(i)\frac{\partial}{\partial_i}\left[\frac{c(i,t)}{n(i)}\right] \tag{7.22}$$

At equilibrium the cluster sizes equal the equilibrium distribution function, $c(i) = n(i)$, and it can be shown that:

$$n(i) = N\exp\left(-\frac{\Delta G_i}{k_B T}\right), \tag{7.23}$$

where ΔG_i is the Gibbs free energy change associated with the i^{th} cluster formation, and N is the total number of clusters. For the steady state, one must integrate the partial differential equations over all values of i. The resulting approximate solutions for the total fluxes yields

$$\mathrm{J_o} N \mathrm{D^+ Z} \exp(-\Delta \mathrm{G^*}/\mathrm{k}_B \mathrm{T}), \tag{7.24}$$

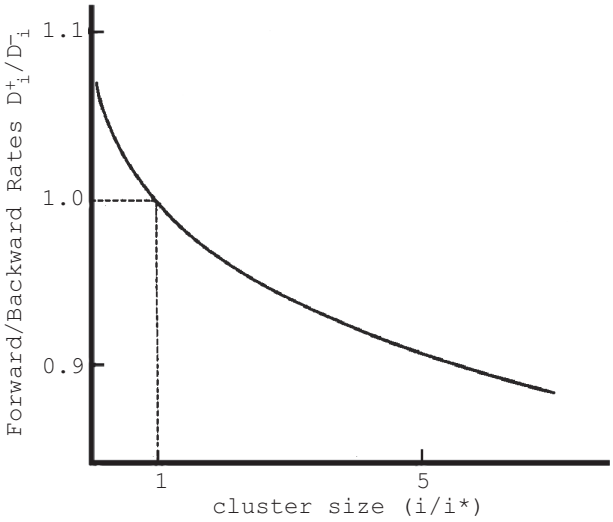

Fig. 7.5 Distribution of cluster sizes as calculated by kinetic theory for equilibrium and steady state conditions. In the equilibrium case critical nuclei are the lowest in abundance, while in the steady state case they have half the equilibrium abundance but larger clusters are still less abundant. (After Toschev, 1973)

where Z, the Zeldovich factor, is approximately $(\Delta G^*/2\pi k_B T)^{1/2}$ and is generally on the order of 0.05. This factor effectively corrects equilibrium classical nucleation rates for steady state situations. In this case the cluster distribution can be calculated from the flux via integral equations of the form $c(i)/n(i) = J_0 \int_i^M di/D^+(i)n(i)$ and the steady state and equilibrium cluster distributions are shown in Fig. 7.5. For the equilibrium case we note that the critical clusters have the lowest concentration, which is in keeping with the experimental problem of observing a critical nucleus. For the steady state the cluster size profile differs near the critical nucleus size, decreasing to half the equilibrium concentration at i^*, and declining for larger cluster sizes. For heterogeneous nucleation, the expressions derived for homogeneous nucleation are often used, with adjustments made for the difference in Gibbs free energy for nucleation. However, the literature consensus seems to be that detailed kinetic theories for heterogeneous nucleation are generally much less accurate than the corresponding homogeneous theory (Wu, 1997), and tests of heterogeneous theory using measured surface energies show poor agreement with experiment (Marasli and Hunt, 1998).

One other aspect of steady state nucleation is the concept of induction time, or time from the initial state until a steady state nucleation process has evolved. This is the period needed for the system to reorganize itself and adopt the steady state condition. A general expression for the induction time, τ, for homogeneous nucleation is:

$$\tau = 0.7b^3 \frac{RT\sigma^3 \nu^2 N_A}{\Delta\mu^4 D^+}, \tag{7.25}$$

where b is a geometrical coefficient equal to $6^{2/3}\pi^{1/3}$ for spherical nuclei, $\Delta\mu$ is the driving force for nucleation, and D^+ is the diffusion coefficient for transfer of atoms to the nucleus. For melts and solutions τ is proportional to the viscosity of the medium due to the D^{-1} dependence. In condensation from vapor, this time is sufficiently small as to be generally negligible, but such is not the case in liquids, glasses and solids. For example, for water condensation from vapor at 300 K $\tau = 3 \times 10^{-8}$ s, but for nucleation of wollastonite from $CaSiO_3$ glass at 1,060 K, τ is on the order of 10^4 s (Granasy et al., 1998). Hence, depending on the precise system being modeled, an assessment of the nucleation rate during the transient time may be crucial in understanding the experimentally measured nucleation rates. It is even possible that complete precipitation can occur before the steady state regime is reached, and hence nucleation rates can continuously change.

We have seen that a discrete cluster kinetic theory can be extended to a continuum partial differential equation formulation. An atomistic version is also possible, but with limitations on the size of clusters that it can consider. In our current vernacular, these treatments equate to molecular dynamics (MD) and kinetic Monte Carlo simulations (KMC). In the MD approach (see Chap. 2) the system is defined by the starting positions and interatomic potentials, with an energy flux related to absolute temperature driving the operations. In MD we can uncover the types of pathways that individual atoms make in producing nuclei whether adding to them or contributing to dissolution, and we can determine cluster statistics as a function of time. This information allows us to consider how and where clusters are formed, and how surfaces (for example) affect cluster formation and growth. Some simplification can be obtained by using transition state theory (TST) wherein we neglect molecular vibrations and just consider the specific diffusion events that characterize system reconfiguration. This is much less general, but much faster in execution computationally.

In the KMC simulation we take into account the spatial aspects of the system and the relevant stochastics, without calculations of complex interatomic interactions. The relevancy of the approach depends on including enough microscopic processes to yield meaningful results and significant time saving. But often this end requires much experimentation to determine what factors are of prime relevance (Ratsch and Venables, 2003). The current most intense use of these methods is in understanding and modeling thin film processes. In semiconductor (integrated circuit) processing, it is crucial to understand how new layers are nucleated and grown so as to limit defects, produce uniform layer thicknesses, and eliminate unfavorable grain boundaries due to the coalescence of two-dimensional islands (nuclei).

7.2.2.2 Density Functional Theory (DFT) Approach

Although DFT methods are frequently used for electronic structure calculations where the electron density of a system is treated (see Chap. 2), on a larger physical scale such as whole atoms or molecules they are important in modeling phase transformations that occur with a diffuse interface. Examples are growth of

compositional fluctuations in a solid solution (e.g., spinodal decomposition, Cahn and Hilliard (1958); Cahn (1962, 1966)), and diffuse nucleation in glasses (e.g., Granasy et al., 1998). For such cases the nature of the interface between matrix and nucleus is not defined, the systems are generally far from equilibrium, and classical methods cannot be applied.

In the DFT approach used in these cases one replaces the atomic or molecular nature of a system with chemical density variation over a continuous medium. One then formulates the free energy of this system as a functional containing local and nonlocal contributions. The approximate equation derived by Cahn and Hilliard (1958) for a cubic solid solution is:

$$F = \int_{\mathrm{v}} \left[f(c) + H(\nabla c)^2 \right] dx \tag{7.26}$$

where $f(c)$ is the local free energy per unit volume, and the second term is the gradient energy, H, that drives the transformation, with H being an approximation of the intramolecular potential, both being functions of the composition, c. Minimizing this integral equation yields the overall density fluctuations in the solution that are most stable. For solid solutions this approach predicts critical nuclei that have finite size and an infinitely sharp interface at equilibrium phase boundaries (e.g., crystal/melt) as in CNT, but have infinite size and a completely diffuse interface at the spinodal. This is in keeping with a process that is occurring far from equilibrium, and the usual form of spinodal decomposition is periodic compositional fluctuations, contrasting with random CNT-type nucleation (DeFontaine, 1975). The growth of these fluctuations is diffusion controlled, based on the local compositional gradients. Annealing of spinodal fluctuations eventually gives rise to coarsening and phase separation, and the appearance of exsolution structures in solid solutions (Yund et al., 1974; Zhu et al., 1999).

Talanquer and Oxtoby (1994) developed a DFT approach for heterogeneous nucleation of droplets with sharp interfaces and compared this with a CNT estimate of nucleation rate. They found that for conditions far from the equilibrium phase boundary, CNT failed drastically, again suggesting the need for a non-classical approach to nucleation at disequilibrium conditions.

7.2.2.3 A Statistical-Empirical Approach: Crystal Size Distribution (CSD) Analysis

From a practical standpoint, we can ask whether we have appropriate experimental information to use any of these theories to allow ab initio prediction of nucleation in geochemical systems. In order to describe nucleation rates over wide conditions for a specific system we would require, above all, good estimates of the interfacial energies, the density of nucleation sites, and the free energy of critical nucleus formation. This is extremely difficult to do (Kelton and Greer, 1988; Kirkpatrick, 1981), for geological systems, and thus nucleation models have been generally treated as empirical fits to the derived mathematical equation form and dimension. However, more

recently it has become possible to model interfacial energies and surface energies (i.e., for surfaces in vacuum) fairly accurately with quantum calculations (Henry, 2003; Bandura et al., 2004).

Regardless of whether we can ever expect to calculate all the parameters we need for the highest-level theoretical approaches, knowledge of the physical theory gives insight into the processes involved and ultimately such atomistic/cluster approaches ought to be applicable to any type of system.

Another approach that treats nucleation and growth kinetics in a statistical manner and allows kinetic parameters to be estimated without the need for accurate interface energies is crystal size distribution (CSD) analysis (Randolph and Larson, 1971). In this approach the distribution of observed crystallite sizes in a sample is measured from thin sections or other petrological/materials sampling to produce a population number density profile which is the numbers of crystals of a given size, $n(L_{CSD})$, divided by the size interval, L_{CSD}. Analysis of this profile is a useful statistical description of, e.g., an igneous crystallization system in a magma chamber, or of sedimentation structures, but can be greatly extended with mathematical analysis (Randolph and Larson, 1971; Marsh, 1988). The information in the $n(L_{CSD})$ versus L_{CSD} profile, as a snapshot of the system in time, is combined with "conservation" differential equations which tie together the change in integrated growth volume with the input and output flux of crystal volume when the system was operating. By using assumptions of various conditions in the system (e.g., flux of crystal mass in = flux out, or growth independent of size, etc.), it is possible with such boundary conditions to evaluate the equations to yield estimates of nucleation and growth rates. Further, the moments of the crystal distribution can be evaluated to yield the most important sizes, masses or lengths of the crystal population, and these, in turn, can be used to extract estimates of nucleation density and other physical attributes (Cashman and Marsh, 1988). CSD analysis appears to be useful because certain reasonable but simplifying assumptions can be made in the analysis, and crystallites once formed appear to have constant growth rates.

7.3 Growth Processes

7.3.1 Classical Growth Theory

As CNT assumed monomer attachment to a growing critical nucleus, classical crystal growth theories assume atom-by-atom or molecule-by-molecule attachment to a growing surface. However the nature of these attachments is rooted in the precise description of the growth surface. Growth in the general case is often presented as an ideal type of epitaxial process, i.e., nucleation occurs with proper registry of new species to the existing atoms on a surface. Nucleation here is somewhat different than in the case of heterogeneous nucleation discussed previously, as the system is supercritical, layers rather than some finite cluster volume are being formed, and direct chemical binding of the new atoms occurs at the interface. Classical theory

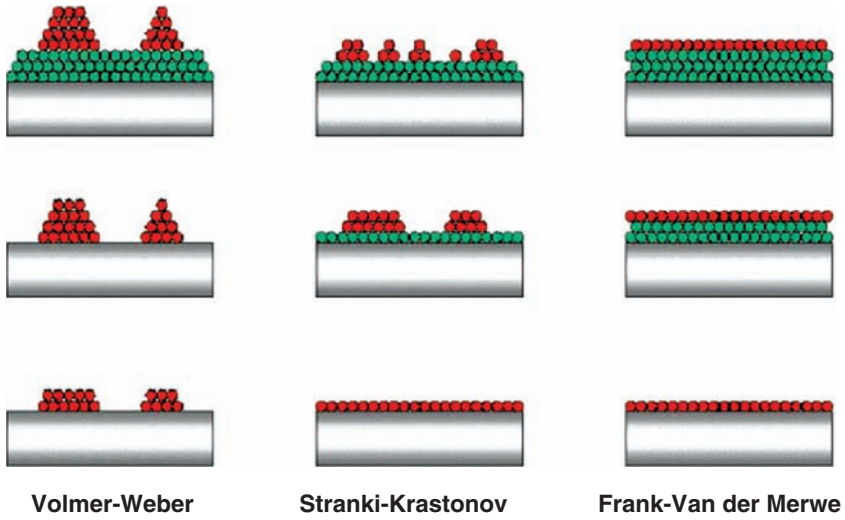

Fig. 7.6 Types of classical growth models. (**a**) Volmer-Weber type (island) growth where interface energy is relatively large. Hence discrete nuclei form and grow before a layer is completed by infilling. (**b**) Stranski–Krastanov type (layer + island) growth where interface energy is comparable to island interaction energy, and hence layer formation competes with nuclei formation. (**c**) Frank-van der Merwe (layer) growth. Here interface energy is relatively low and layers form readily from nearly any size nuclei

often begins with the assumption that growth is occurring under a supersaturated condition, so that the system is not close to equilibrium. Hence we start with that case.

The most common growth model is Frank-Van der Merwe growth, also known as "layer-by-layer" growth. In this model (Fig. 7.6) a layer of atoms is started and completed before another layer starts to grow. The model assumes that attachment of atoms to the edge of a growing layer is far more likely than attachment to the top of the layer, i.e., new nucleation, and hence the latter rarely occurs.

The simplest energetic interpretation is that the atom attaching to the growth layer edge makes two or more bonds while one connecting to the top surface makes only one, and hence reduces the interfacial energy by much more. In a kinetic interpretation the atom attached to the top of the surface will diffuse quickly until it encounters a new layer edge, and, now having two bonds, thereafter will have a much lower probability of moving back to the surface. Similarly, an atom bonded to the edge of the surface layer may diffuse along the edge until it can find additional bonding opportunities at "kink" sites (see also Figs. 7.7 and 7.8 in Chap. 3).

The direct opposite to this type of growth is the Volmer–Weber type (Fig. 7.6), where nucleation of islands is favored over extended growth at layer edges. This can occur if the new precipitating species have a tendency to cluster, i.e., the new atoms bond more strongly with one another than to the surface, or if diffusive processes slow layer growth until new surface nucleation far exceeds it (resulting

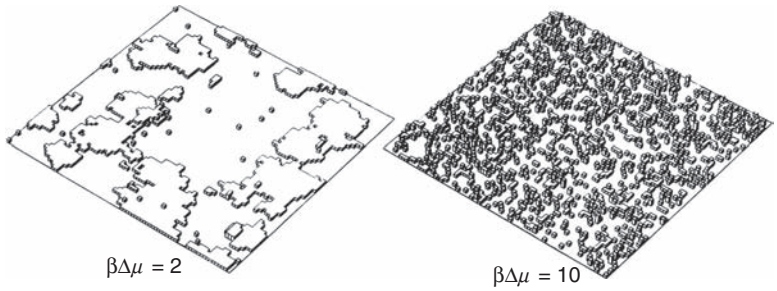

Fig. 7.7 Monte Carlo simulation of interface topology after 25% of a monolayer is deposited on a flat (001) crystal face at the same temperature but different values of the product of inverse energy ($\beta = 1/ < \square > T$), and difference in chemical potential from the equilibrium solid ($\Delta\mu$), which is equivalent to the driving force for growth. For a product of two layer formation is favored, but for ten, nucleation is favored over layer growth. (After Weeks and Gilmer, 1979)

Au: Please check white box in figure caption.

in increased nuclei density). The net effect is that layers are filled in as islands are nucleated and merge. Finally there is a mixed alternative, known as Stranski–Krastonov growth, where growth is initiated as a layer-by-layer mode but shifts to an island mode.

Using these types of surface features in what is called the solid-on-solid (SOS) model, a kinetic equation can be generated that describes the rate of change in occupation of surface sites in any incomplete surface (growth) layer (Weeks and Gilmer, 1979):

$$\frac{dC_n(t)}{dT} = k^+[C_{n-1}(t) - C_n(t)] - k(n,t)[C_n(t) - C_{n+1}(t)] \tag{7.27}$$

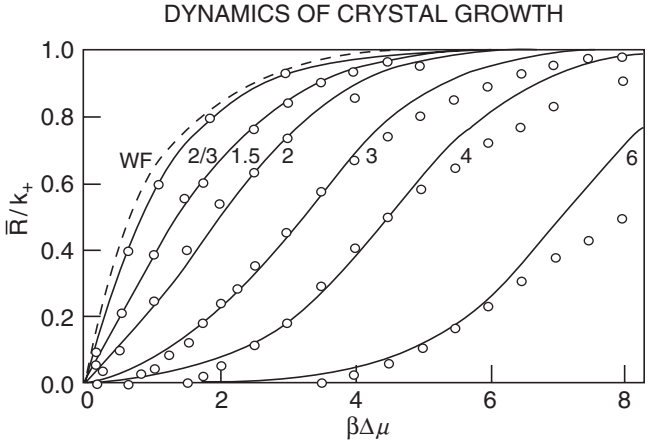

Fig. 7.8 Mean growth rates R normalized by the deposition rate k^+ for the 2-rate model (solid curves) compared to Monte Carlo simulations (circles) for a range of $\beta\Delta\mu$ values (After Weeks and Gilmer, 1979)

Here the $C_n(t)$ are the occupations of the nth layer parallel to the surface, k^+ is the deposition rate of atoms or molecules on the surface, and k^- is the effective evaporation or desorption rate:

$$k(n,t) = \nu_d \sum_{m=0}^{4} \exp(-m\beta\Phi)\, f_{n;m}(t), \tag{7.28}$$

where m is the number of adjacent layer neighbors, $f_{n;m}(t)$ is the fraction of surface atoms in layer n with m neighbors, ν_d is the desorption rate for an isolated surface atom, β is $1/k_B T$, and Φ is the chemical potential change on desorption. Equation (28) shows that the desorption rate is reduced as the number of atom neighbors increases, reflecting bonding with these atoms. With these expressions the growth rate, R_{SOS}, for the surface is now:

$$R_{SOS} = k^+ - \sum_{n=-\infty}^{\infty} k(n,t)\, f_{n;m}(t), \tag{7.29}$$

i.e., the difference between deposition processes and desorption processes, respectively, for all surface layers. Using Monte Carlo methods, Eq. (7.29) can be used to generate a model surface. For example, taking T constant and time interval t where 25% of a surface layer has formed, the atomic arrangement for two different values of $\beta\Delta\mu$ are shown in Fig. 7.7. For large $\beta\Delta\mu$, the desorption rate is low for isolated surface atoms and small islands saturate the surface, whereas for small $\beta\Delta\mu$ the desorption rate is high and only atoms associated with already nucleated layers persist. This approach is extremely basic, including no anisotropy in the surface (i.e., the system is rigorously cubic in symmetry), and making implicit assumptions about how atoms can diffuse (viz. only along layer surfaces). However it is not a poor assumption at high driving force, i.e., high supersaturations or low temperatures.

To improve the model we need to extend the applicability to cases near equilibrium at low driving force. One such theory is that of Weeks et al. (1976), called the "two-rate" model. In this model steady state growth is assumed, i.e., the surface condition at some time t is closely similar to that observed at a later time $t+\gamma$, where γ is the mean time required to deposit a monolayer of atoms. Hence each layer in the surface behaves essentially similarly with time, and a given upper layer looks like a buried one after the appropriate dwell period. For this model two rates for desorption are used, a fast one for layers that are less than half populated, and a slow one for layers that are more than half populated. This considers, in a very simple way, the effect of higher numbers of nearest neighbors on the desorption rate.

Rather than show the derivation of this model here, we just quote the resultant average growth rate:

$$\overline{R} = \frac{(k^+) - k_{eq}^2}{\bar{k} + k^+}, \tag{7.30}$$

where $\bar{k} = (k_{slow} + k_{fast})/2$, and $k_{eq} = (k_{slow} + k_{fast})^{1/2}$. By adding the mean probability, C, that a surface atom can find a neighboring occupied atomic site into this

expression, one obtains the growth rate:

$$\frac{\overline{R}}{k^+} = \frac{2\sinh(\beta\Delta\mu)}{\exp(\beta\Delta\mu)+\cosh(\varepsilon\beta\Phi)}, \tag{7.31}$$

where $\varepsilon = 2(1-2C)$. This is plotted (solid lines) for a range of $\beta\Delta\mu$ values in Fig. 7.8, and compared to the Wilson-Frenkel (WF) rate, which fixes the desorption rate to that of the bulk crystal phase at equilibrium. This theory agrees fairly well with MC simulations (circles) of growth rates at higher temperatures and high deposition rates for simple systems (Weeks et al., 1976). Another type of Monte Carlo growth simulation also agrees well with this type of kinetic approach (Jiang and Ebner, 1989).

7.3.1.1 Effects of Screw Dislocations on Growth

The models discussed above generally produce rather slower kinetics compared to what is commonly observed in natural systems. This is due in large part to the presence of growth defects in real systems that make it easier or unnecessary to nucleate a new growth layer. The most important case is that of screw dislocations, first described by Frank (1949) and Burton et al. (1951). Figure 7.9 shows the development of a spiral growth pattern about a screw dislocation.

MC calculations of growth rates from the SOS model on a perfect crystal and a spiral growth model are shown in Fig. 7.10. In the plot, L/k_B T is a measure of atom-atom binding force, L, versus available energy, k_BT. For lower binding energies there is little difference between the two growth rates, but divergence is notable with increasing binding energy. One can see that at sufficiently low temperatures, layer-by layer growth is quenched relative to spiral growth. The effects of variation in the 2D nucleation of layers and evaporation rate have been considered explicitly by Weeks and Gilmer (1979). More details on this type of growth are available in Chap. 3.

7.3.1.2 Molecular Models

The models described so far do not consider the molecular basis of growth explicitly, and to practically consider the effects of impurity incorporation and the broader range of defects and surface processes a truly molecular model is required. Paquette and Reeder (1995) developed one such molecular model for impurity incorporation in calcite largely based on the concept of the periodic bond chain (PBC) model of Hartman and Perdok (1955). In this model crystal growth is favored by attachment of new species along the directions of the strongest PBCs. Hence analysis of the nature of the PBCs allows prediction of growth rates and habits. For impurity incorporation, the PBCs allow description of the kink sites where attachment of new species occurs, and it also identifies non-equivalent kink sites within the same growth layer (Fig. 7.11). Such inequivalent sites display different binding energies

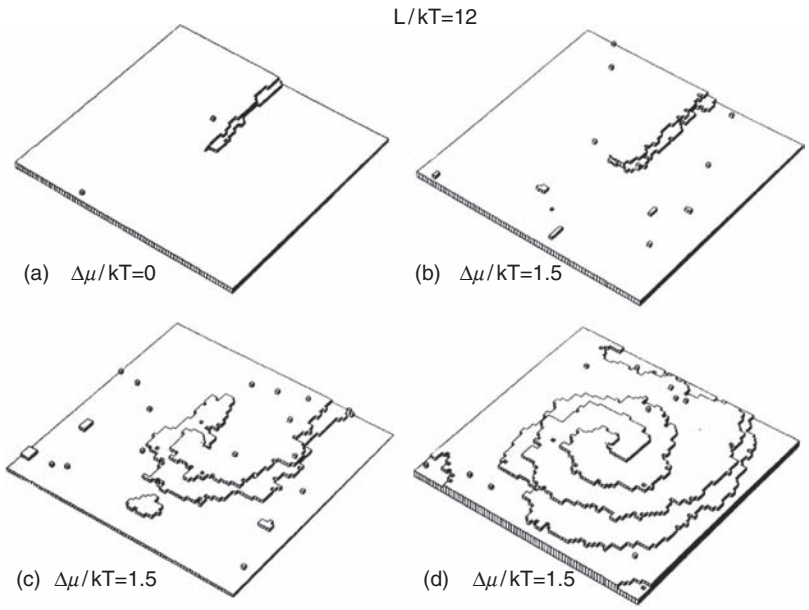

Fig. 7.9 Monte Carlo simulation of evolution of the double spiral type of layer growth produced by a screw dislocation. The temperature is parametrized by L/kT where L is the binding energy per atom in the lattice. (**a**) is the equilibrium state, and (**b**) through (**d**) show progressive evolution of growth with $\beta\Delta\mu = 1.5$ favoring layer growth. (After Weeks and Gilmer, 1979)

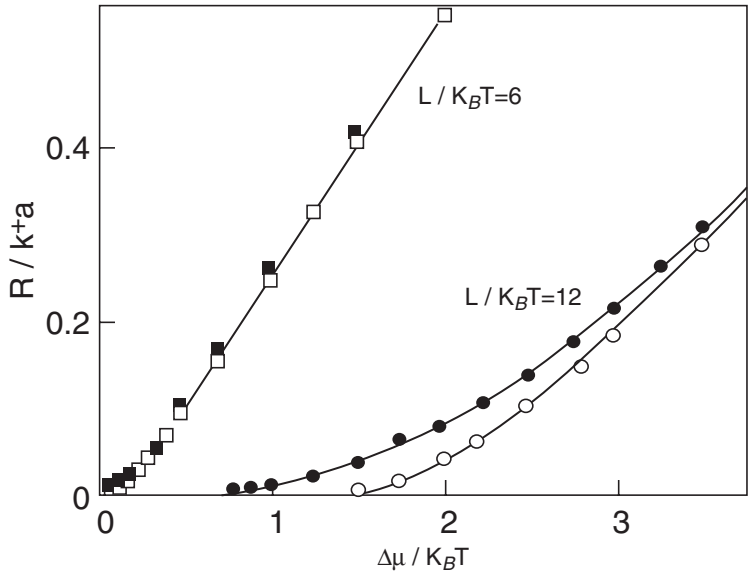

Fig. 7.10 Comparison of growth rates for perfect layer by layer (open symbols) versus spiral growth (solid symbols) for two parameterized temperatures. (After Weeks and Gilmer, 1979)

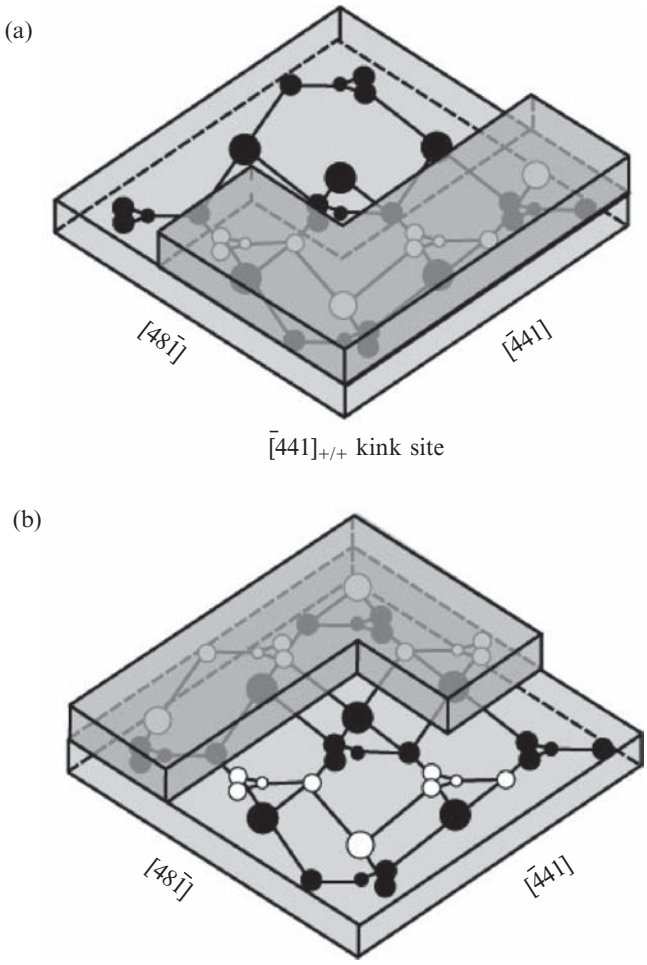

Fig. 7.11 Models of cation kink sites where divalent metals can be incorporated into growth steps on the calcite (10–14) surface. Open circles are atoms that reside in the upper slice, while solid atoms are in the lower slice. Divalent substituent atoms in the kink sites are depicted by arrows. In the $+/+$ kink site the divalent atom is coordinated by three oxygens of the same carbonate layer, whereas in the $-/-$ kink site the three O atoms reside in adjacent carbonate layers. Hence the geometry and effective size of the sites differ as "seen" by a possible substituting divalent atom. (After Paquette and Reeder, 1995)

for particular impurities, forcing these species to segregate in a particular manner, which in turn could be conducive to particular zonation effects.

A related model discussed by Pina et al. (1998) for the aqueous growth of barite considers the underlying atomic structure of the growth surface also with reference to PCBs, and the specific energetics of atomic attachment. AFM observations show that at high supersaturations nucleation on the barite (100) surface is initiated at

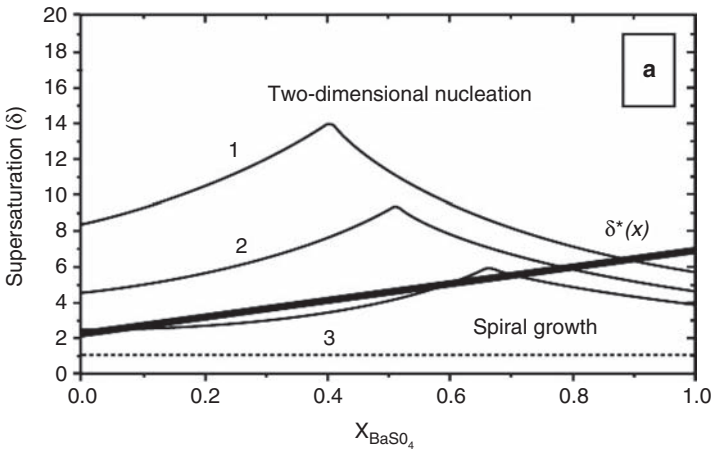

Fig. 7.12 Supersaturation trends for solid solutions $(Ba_x, Sr_{1-x})SO_4$ growing on barite (001) at three different solution compositions (see text). Each possible solid solution composition has a different supersaturation. Changeover from two-dimensional nucleation and layer growth to spiral growth occurs at the heavy line $(\delta^* x)$. (After Pina et al., 2004)

a screw dislocation, but does not proceed classically. Rather the growth spiral is extremely tight resulting in a hillock near the dislocation core with anisotropic lateral layer spreading. The disruption in the spiral mechanism is caused by the strong growth anisotropy, which is created by differing attachment energies for Ba and SO_4 units at particular positions on the growth layer. Effectively, growth dominates along a single direction having a specific polar orientation and hence lower symmetry than would be expected from any more classical growth model.

7.3.1.3 Solid Solutions

Crystal growth from solutions with mixed ions can produce markedly zoned crystals, but growth mechanisms and kinetics have been little treated. The main complication is that the degree of supersaturation of the solution phase, and thus the driving force for crystallization, is a function of the composition of the crystallizing solid phase. Pina et al. (2004) suggested a formulation for the supersaturation of barite-celestite solid solutions that illustrates the issues. Figure 7.12 shows a plot of supersaturation, δ, in this system as a function of barite fraction in the precipitated solid solution. The solution compositions are: (1) $[Ba] = 1\,\mu mol/L, [Sr] = [SO_4] = 3,000\,\mu mol/L$; (2) $[Ba] = 1\,\mu mol/L, [Sr] = [SO_4] = 2,000\,\mu mol/L$; (3) $[Ba] = 1\,\mu mol/L, [Sr] = [SO_4] = 1,100\,\mu mol/L$. The bold solid line is the observed delineation between two-dimensional layer nucleation and growth at higher supersaturations, and spiral growth about dislocation cores. As growth continues the solution changes composition and the solid solution composition having greatest supersaturation also varies, which can lead to a continuous change in the precipitate composition. A further consequence of these compositional dependences is that a

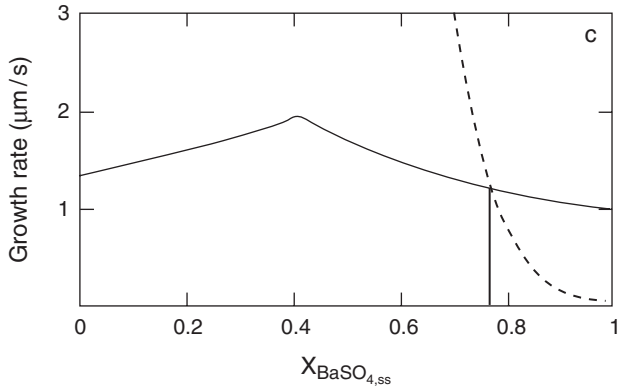

Fig. 7.13 Comparison of growth rates from solution #1 of Fig. 7.12 for different compositions of solid solution. Solid solutions of composition 0.766 barite or greater can only grow by the spiral growth mechanism. (After Pina et al., 2004)

change in growth mechanism can occur at a specific composition of the solid solution. Figure 7.13 shows the growth rates as a function of composition for one of the solutions (#1) shown in Fig. 7.12. Both growth rates calculated for layer growth (solid) and spiral growth (dashed) using classical rate formulations (Ohara and Reid, 1973) are shown. Layer growth is faster at compositions below 0.766% barite, but slower at higher barite fraction where spiral growth takes over.

7.3.1.4 Growth Kinetics as Measured by Volume Transformations

For certain types of systems, especially solid-state transformations in metals, semiconductors and metamorphic rocks, the use of layers (i.e., interface growth rates) is inconvenient. In these cases growth is often modeled by the rate of volume converted into a new phase. Such models are semi-empirical and consist mainly in the way in which certain types of grain growth will fill three-dimensional space as recrystallization or phase transformation proceeds. An example is the approach taken by Johnson and Mehl (1939), and Avrami (1941) for spherical grains and the impingement of transformed regions affecting the rate dependence. For empirical treatments, the volume fraction transformed, α_A, is given by:

$$\alpha_A = 1 - \exp[-(kt)^n], \tag{7.32}$$

where k is the first-order reaction rate constant, and n is the time exponent. Johnson and Mehl (1939) assume that the nucleation rate and the growth rate are independent of time and the amount of volume transformed, and that nucleation is random in position. This yields the formulation:

$$\alpha_A = 1 - \exp(-1/3\pi I U^3 t^4), \tag{7.33}$$

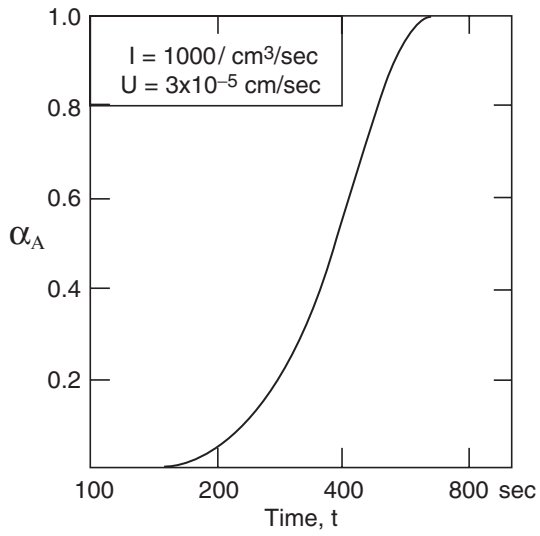

Fig. 7.14 Fraction of volume transformed in a material using the Johnson–Mehl empirical approach. The case shown assumes constant nucleation (I) and growth rates (U) and spherical particles, but other shapes of particles alter the exponent in the growth law and can be extracted from this type of analysis. The method is useful for describing transformation kinetics of various types, e.g., phase transformations, coarsening of grains, but does not include diffusion-controlled processes. (After Raghaven and Cohen, 1975)

with I being the nucleation rate and U the growth rate of individual grains, and α plots as a sigmoid with time (Fig. 7.14).

If we assume that nucleation is unlimited in position and speed, this reduces to the Avrami relation:

$$\alpha_A = 1 - \exp(-1/3\pi N_v U^3 t^3), \tag{7.34}$$

with N_v being the nucleation sites per unit volume. It is popular to use the exponent in the Avrami equation to determine the nature of the growing crystallites, whether plates, discs, rods and so forth (i.e., a smaller exponent leads progressively to plate then rod growth; for an example of such an approach see later in the example in IV: Aggregation processes; Sect. 7.4.4). However, it should be noted that this approach sometimes is of questionable validity unless only very small degrees of transformation occur (Price, 1965; Castro et al., 1999). Moreover, these kinds of empirical equations do not address nonisovolumetric changes during the transformations, and this in turn will lead to errors in their application if not considered.

7.3.1.5 Growth Morphologies

The near-equilibrium geometry of a growing crystal can be shown to be controlled by the relative interface energies of its bounding faces (Wulff, 1901; Herring, 1951). This is based on the assumptions that the overall surface energy of the crystal has to be a minimum but the surface must consist of flat facets. As impurities in the growth solution can change the interaction energies of surfaces, this model demonstrates why such impurities can lead to changes in crystal habit, i.e., the relative importance of the main set of surface facets. Kinetic factors can have large effects on this direct equilibrium picture. Impurity sorbants can interfere with addition of new

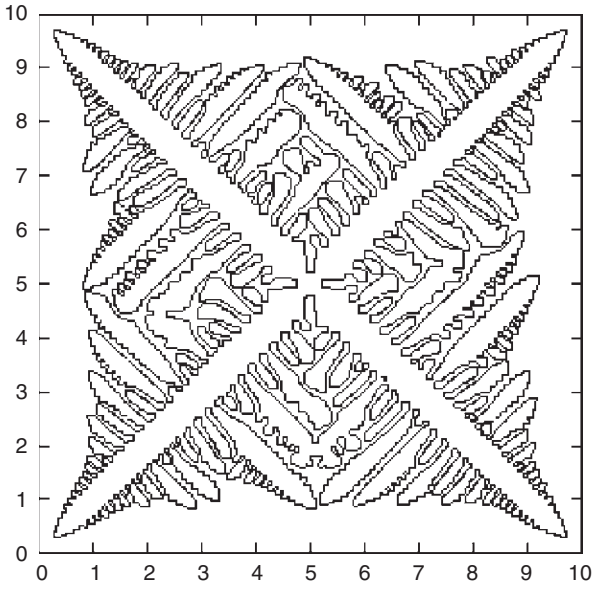

Fig. 7.15 Simulated dendritic crystallization pattern for a cubic alloy

species to a growth step, hence poisoning the growth (Van Enckevort et al., 1996; Kubota and Mullin, 1995). Impurities can also affect growth of secondary phases by influencing nucleation kinetics (Liu et al., 1997). In growth from a melt or aqueous solution the interface structure is also highly dependent on diffusion of species to the interface. For example, dendritic growth occurs when the tip of a growing crystallite exceeds the diffusion rate in the solution or melt. Growth is therefore retarded in certain directions until the diffusing species "catch up", resulting in a dendritic pattern (Fig. 7.15). Thermal effects relating to the dissipation of the heat of crystallization can also produce dendritic growth. Skeletal or "hopper" crystals result both from very rapid growth in particular directions, as may be assisted by screw dislocations, or from severe diffusion limitations.

7.3.2 (Nucleation and) Growth Far from Equilibrium

Growth characteristics may be markedly different at high supersaturation and driving force. We have already mentioned how dendritic growth can occur if a high driving force causes growth to exceed diffusion through a growth medium. This type of growth is actually an extreme case of diffusion-limited-colloid-aggregation (DLCA, see below) at the molecular level (Bunde and Havlin, 1991). But less obvious situations ensue from annealing of solid solutions well below the liquidus, creating the density fluctuations noted above in Cahn and Hilliard's (1958) pioneering work on spinodal decomposition and applied density functional theory. Several

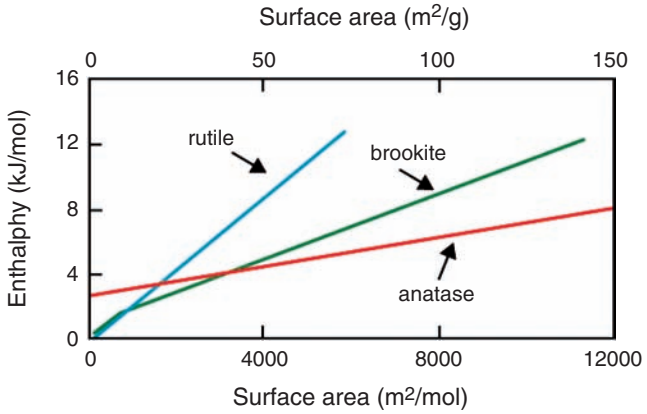

Fig. 7.16 Enthalpy of titania polymorphs as a function of surface area (After Navrotsky, 2004). The first nucleated phase is anatase which becomes unstable relative to brookite when it grows to a size of several nm. The rutile phase then becomes stable with particles on the order of 5 nm

other cases are important to consider: the growth of metastable phases and the Ostwald Step Rule, aggregation type growth processes, and other types of dissipative processes.

7.3.2.1 Metastable Phases and the Ostwald Step Rule

In all discussions above, we have considered that the nuclei that form during crystal growth are of the same phase (i.e., structure) as the equilibrium bulk phase. However, in reality the first crystallites that form may be limited kinetically to those that are most readily nucleated. This is most easily seen in polymorphic phase transformations where the initial nuclei are thought to be those with the lowest surface energies, despite their being absent on the equilibrium phase diagram at the (P, T, x) conditions of formation. The TiO_2 system affords an excellent example. In Fig. 7.16 (Ranade et al., 2002) the enthalpies of the TiO_2 polymorphs are shown as a function of specific surface area (i.e., inverse size regime). This suggests that the structure of the first formed nuclei would be that of anatase, which would become metastable with respect to the brookite structure at larger sizes, and then with respect to rutile at largest sizes. Fast growth would thus favor the creation and likely persistence of anatase, while slow growth would give time for transformations into the appropriate stable polymorphs.

Other systems where a metastable phase is first observed to form include disordered dolomite prior to ordered dolomite (Navrotsky, 1999), vaterite or aragonite prior to calcite, and a silica derivative prior to cordierite (Carpenter et al., 1983). Such observations support the Ostwald step rule, or the notion that the earliest formed phases may be the ones most easily nucleated rather than the most stable (Navrotsky, 2004). Interestingly, both kinetic and thermodynamic arguments support this "rule". The kinetic analog of the surface energy argument is that structures

similar to their host matrix or solution may form faster than a markedly variant structure stable phase.

7.3.2.2 Oriented Aggregation as a Variation on Classical Growth Method

There have been both conjectures and observations that crystal growth on the nanoscale may occur not by the buildup of structures layer by layer, but by the aggregation of clusters that assemble with proper crystallographic orientations. This oriented aggregation (OA) would be decidedly nonclassical inasmuch as the free energy of cluster attachments, probability of attachment and geometric reorientations would need to be considered as a function of impingement trajectory. Hence this type of growth would be intermediate between aggregation "growth" (see section below) and classical approaches.

Direct evidence for OA has been acquired with TEM imaging of anatase (Penn and Banfield, 1999) and sphalerite (Huang et al., 2003) where small assemblies of oriented nano-scale crystallites are clearly observed. Nanogoethite particles on the 50 nm scale also appear to be formed from assembly of 5 nm particles under certain synthesis conditions (Waychunas et al., 2005). Such assemblies are difficult to explain by standard growth or coarsening mechanisms, yet detailed treatment of OA phenomena appear to be neglected in the literature. Changes in the kinetics of crystal growth that could occur due to OA might best be referenced to a kinetic nucleation model. Instead of nuclei growing to the critical size by addition of monomer units, they could reach this stage in a single step from the subcritical size via an OA mechanism. However further assembly may be limited by geometric conditions, e.g., at some small subcritical size any face of a growing unit might be attachable to a similar unit, but once some attachments are made the number of regular attachment surfaces would be decreased. This reasoning suggests that OA may be an important process in a particular size regime, and also that growth kinetics may vary markedly with size even with all other factor equal. OA may also turn out to be important only for supercritical nuclei, ostensibly because these would tend to be stable long enough for aggregation to occur while subcritical nuclei have a more fleeting lifetime.

7.3.2.3 Other Dissipative Processes

At conditions far from equilibrium a system may transform via quite complex stages including large exchanges of matter and energy with the surroundings, high entropy production, or unusual types of organization, possibly highly chaotic. Although it may be kinetically stable for some time period, i.e., in a *stationary* state, such systems can change suddenly and dramatically as they dissipate excess energy and gain entropy (see also Chap. 1). The concept of dissipative systems (DS), was originated by Prigogine (1961), and a large body of work describing biological, chemical and physical DS has followed his groundbreaking ideas (see, for example,

Nicolis and Progogine, 1977). In geochemical systems there are numerous examples of DS (see also Chap. 11), including oscillatory zonation in crystals, flow-driven reaction fronts, Liesegang banding, reaction-driven advection, and reactions featuring instability, feedback and bifurcation. Our only example above of such a system was that of spinodal decomposition treated by finite DFT methods, but aggregation processes, reactions that include an autocatalytic step (such as pyrite oxidation), and many types of biogeochemical precipitation processes may only be treatable as DS via non-equilibrium thermodynamic methodology (see, for example, Katchalsky and Curran, 1965; Trivedi et al., 2002). We mention this here as a reminder that natural growth processes in general are not close to equilibrium, and hence growth formulations that assume such can lead to misleading results.

7.4 Aggregation Processes

As we mentioned above, following nucleation, the newly formed particles can either grow to larger units and/or become more crystalline. Naturally, due to interparticle forces (both attractive and repulsive), the individual nuclei can grow by aggregation of smaller units. The aggregation of colloidal particles is prevalent in most natural environments and occurs in all physical, chemical and biological systems. Overall, aggregation is considered a non-equilibrium process that dominates when larger particles form from smaller ones and the structure of colloidal aggregates is believed to be scale invariant (Weitz et al., 1984) thus allowing for a new dimension to be introduced; the fractal dimension (see, for example, Mandelbrot, 1975 and below). This in turn, permits a more detailed study of aggregation processes via their physical relationships that link cluster structures to aggregation kinetics. In order to understand aggregation, first we need to remind ourselves of the various forces of attraction and repulsion between individual particles: covalent, electrostatic, dipole-charge and dipole, dipole as well as van der Waals and hydrophobic. A detailed description of these forces and their magnitude and range of action is outside the scope of this chapter but average values and examples can be found in Israelachvili (1992) and Waychunas (2001).

7.4.1 Aggregation Regimes: DLCA and RLCA

Similar to the theories that define the reactions during nucleation and growth, a whole series of theoretical and experimental approaches have been developed with the goal to quantify the mechanisms and kinetics of aggregation. Aggregation of monodispersed colloids will provide a specific cluster mass distribution (CMD) due to the fact that the aggregation pathway of the particles is random and this will result in different aggregate sizes. For charge stabilized colloids, usually the Derjaguin–Landau–Verwey–Overbeek (DLVO) model is invoked but the essential characteristics are applicable to all types of colloids. Overall the repulsive forces between

particles are dependent on the repulsive energy barrier between two particles that are approaching. When this barrier is still several k_BT (k_B) = Boltzmann's constant and T = absolute temperature) the particles will be unable to stick to each other and thus they will repulse each other, despite the drive from the diffusion motion. Therefore, in such a system the particles will be stable and not aggregate. When this barrier is reduced aggregation can occur. When the energy barrier is smaller than k_BT and two particles collide, each collision will lead to the two particles sticking to each other (sticking probability = 1) and thus very rapid aggregation will occur. This process is subsequently only limited by the rate of the diffusion-induced collision efficiency and thus the resulting aggregation process is called diffusion-limited colloid aggregation (DLCA). DLCA is more rapid and every collision results in the formation of a new cluster with a relatively open structure. On the other hand if the energy barrier is equal or larger than k_BT, the number of collisions that will lead to sticking between particles is larger and the aggregation rate is limited by the probability of these collisions to overcome the repulsive barrier. This process can be expressed as a power law with:

$$P \sim \exp^{(-\mathrm{E}_b/k_B\mathrm{T})} \tag{7.35}$$

with P being the probability of collision and E_b, the energy barrier. Such a process is much slower and thus is governed by the speed of reaction and is termed reaction-limited colloid aggregation (RLCA). RLCA is slower and only a small fraction of all collisions leads to the formation of a new aggregate. In addition due to the lower sticking probability in a RLCA process relatively denser aggregates form.

In both cases once clusters are formed they continue to diffuse, collide and aggregate and thus both regimes are also examples of cluster-cluster aggregation. Noteworthy, is that once particles or clusters collide and stick, the aggregation is an irreversible process (Lin et al., 1990). Both regimes are characterized by a limited fractal dimensionalities (see below), specific shapes and CMD as well as kinetic rates. For many systems there will be an intermediate regime where the two models overlap but overall, the physical, chemical and mathematical concepts that support the two models are sufficiently well defined to describe the full range of kinetic processes linked to colloid aggregation (Lin et al., 1990).

Diffusion-limited aggregation was first mathematically described by Witten and Sander (1981) as a model in which a particle is added one at a time to a growing cluster. Such a single particle addition model invariably leads to a power law relationship between the number of individual particles and the dimensionality of the resulting cluster. In this case, diffusion is the movement of particles due to temperature fluctuations as seen in Brownian motion and this process can be simulated on a computer as a random walk. An aggregate is defined as a collection of particles that are connected together and the process is termed diffusion-limited when the aggregate increased in size by one particle at a time rather than by bunches (Witten and Sander, 1981). This is occurring because the density of particles is low and thus the particles do not come into contact with each other before reaching the aggregate. The forces between the particles can be either weak or strong. For particles that carry electrical charge (ions), these forces are typically much stronger and thus building

an aggregate is energetically favorable. It thus follows that overall, aggregates are the preferred state compared to individual ions or single particles.

In some cases when aggregates become well ordered, they form crystals. The ordering force is dependent on the shape and charge of the ions, and (almost) always for a distinct set of ions such a process leads to the same final shape (e.g., NaCl typically forms a cube). If no electrical charge exists, the forces are much weaker and thus, usually particles will stick to each other but at distinct opportunities they will separate and move around again. If this process does not lead to an ordering in the electrical field of the charged particles, the aggregates have no distinct shape and each aggregate that forms will be unique and thus such aggregates are very loose or poorly defined (e.g., Ferrihydrite).

A theoretical basis that takes into account diffusion, Brownian motion and aggregation and links them to the CMD was developed by Smoluchowski (1916) who derived a model for the time dependent changes (rates) in the CMD through a statistical approach. His approach takes into consideration the characterization of a reaction kernel (reaction core), $k_{i,j}$, and the aggregation rate of two particles/clusters of different masses. Aggregation modeling began with the development of three main computer simulation approaches: (a) the ballistic deposition model by Vold (1959, 1963), the ballistic cluster-cluster aggregation model by Sutherland (1967) and the surface growth model by Eden (1961). Due to the restricted capability of computer resources at the time these models were rather simple and used only a limited number of units (i.e., particles). In the last 10–15 years however, advances in our understanding of the physics and mathematics of aggregation, new experimental approaches that can deliver more accurate aggregation parameters and the increase in computer speed has allowed these models to be vastly refined and this has lead to the development of more complex concepts that include the fractal geometries (i.e., Mandelbrot, 1967, 1983; Witten and Sander, 1981; Meakin, 1983).

For most aggregation processes, the relationship between the number of clusters N, and the cluster mass, M, can be expressed as (see also Vicsek and Family, 1984):

$$N(M) = {M_n}^{-2}\psi(M/M_n) \tag{7.36}$$

where M_n is a function of the time elapsed since the initial aggregation process started and ψ is a time independent scaling factor that reflects the shape of the cluster mass distribution. The cluster-mass distribution can be expressed as a power law dependent expression with an exponential cutoff:

$$N(M) = \mathrm{A}M^{-\zeta}exp(-M/M_c) \tag{7.37}$$

where the value of ζ is a function of the kernel shape and A is dependent on the relationship between the total mass of particles and the number of primary colloidal particles. For RLCA, Ball et al. (1987) determined a theoretical scaling factor for each kernel and derived a value for ζ of 1.5. However, other theoretical studies suggested values for ζ of 2 (Meakin and Family, 1987).

A recent very elegant approach by Sandkühler et al. (2005) connected the numerical solution for CMD in the Smoluchowski equation (Smoluchowski, 1916) with

experimentally measured angle dependent hydrodynamic radii of the colloids (from dynamic light scattering) in order to model the link between DCLA and RCLA kinetics in colloidal dispersions. Sandkühler et al. (2005) showed that an aggregation rate that accurately described both DLCA and RLCA processes is a simple function that can be expressed as:

$$K_{\mathrm{i,j}} = \mathrm{K_B W^{-1}} B_{ij} P_{ij} \tag{7.38}$$

where $K_{\mathrm{i,j}}$ is the rate constant that determines the coalescing of particles of size i and j, B_{ij} expresses the size dependence of the diffusion coefficient for these particles and P_{ij} accounts for any matrix effects. Furthermore, $\mathrm{K_B}$ accounts for the diffusive Brownian motion of the particles and is equal to $8k_{\mathrm{B}}\mathrm{T}/3\eta$ (k_{B} = Boltzmann constant, T = absolute temperature; η = dynamic viscosity constant). The parameter W is a stability ratio that accounts for the interactions between the primary particles and is equal to the ratio between $\mathrm{K_B}$ and $\mathrm{K_{da}}$, which is the aggregation rate of particles that are partially destabilized during aggregation. This rate is usually smaller than $\mathrm{K_B}$. A fair approximation of W can be calculated from the DLVO theory but preferentially it should be determined directly from experimental data (i.e., scattering or spectroscopy).

For both aggregation regimes stringent analytical solutions have been formulated and additional details on the mathematical derivation of the aggregation equations as well as many examples based on computational and mixed experimental and theoretical cases can be found in Witten and Sander (1981), Ball et al. (1987), Barabasi and Stanley (1995), Everett (1988), Pfeifer and Obert (1989), Lin et al. (1990), Meakin (1998), and Sandkühler et al. (2005) and references therein.

7.4.2 Fractals

In the stochastic characterization of aggregation the fractal dimension is an indispensable but difficult to calculate/quantify concept. The word fractal is derived from the Latin "fractus" meaning "broken or uneven" and a fractal stands for "any of various extremely irregular curves or shapes for which any suitably chosen part is similar in shape to a given larger or smaller part when magnified or reduced to the same size" (Websters On-line Dictionary). Basically, a fractal is any pattern that reveals greater complexity as it is enlarged and is made of parts that are in some way similar to the whole (self-similarity principle, Mandelbrot, 1967; Nicolis and Prigogine, 1977; Whitesides and Grzybowski, 2002; Lehn, 2002)

Fractals were first described mathematically by Mandelbrot (1975, 1983) and a classical example of a Mandelbrot fractal shape is shown in Fig. 7.17a. Additional examples of fractals in nature are ammonite sutures, tree branches, coast lines rivers, sand dunes, ice crystals etc. (Fig. 7.17a–f, see also Fig. 7.1a).

The classical example used to describe fractals is the "coastline". If we want to know "how long a coastline is," a reasonable approach would be to go and measure the length of the coast with some kind of geometric device (i.e., a ruler). However, obviously, as you decrease the size of the measuring device, the length that you

Fig. 7.17 Examples of natural and mad-made fractals; (**a**) classical Mandelbrot fractal image (**b**) lightning fractal (**c**) fractal image of a tree canopy (**d**) fractal coast line, south coast of Norway; (cropped from image of Jacques Descloitres, MODIS Rapid Response Team, NASA/GSFC and Visible Earth; Image: Norway A2002306.1055.367.250m.jpg; source http://visibleearth.nasa.gov; see also Figure 5 in Chap. 3) (**e**) Fractals and Art: (Phoenix Galactic Ammonite; copyright Weed@wussu.com) (**f**) fractal image of ice crystals (reprinted with permission of Poul Jensen); Note: images a, b, and c, and f are all from clipart files derived from the copyright-free public domain

have to measure becomes greater. Yet, as you get closer and closer (better accuracy), the length of the coastline increases without limit, thus showing us its fractal nature. The "coastline" is the classical example of a self-similar fractal. Its length is a function of the size of the ruler and follows a power law (Mandelbrot, 1967). A two-dimensional DLCA aggregation model can serve as an example (Fig. 7.18) because it shows the same density gradient distribution at any length scale. The fractal theory was further developed in the last three decades in order to achieve a better characterization of different phenomena in physics, chemistry, biology, and medicine.

In order to quantify fractals we need to understand the notion of a fractal dimension. Classical geometry tells us that objects have integer dimensions: a point has no dimensions, a line has one dimension (only infinite length), a plane has two dimensions (length and width) and a cube or a sphere has three dimensions (length, width and height). However, due to the self-similarity concept, fractals have a fractional (or fractal) dimension, D_f, which usually lies between 1.4 and 3.

The fractal construct in Fig. 7.18b is a Vicsek fractal (Vicsek, 1992; Beelen et al., 1997), which is constructed by the endless addition of the same figure to the corner points of the original construct. This addition results in a threefold increase in the size of the construct, R_f.

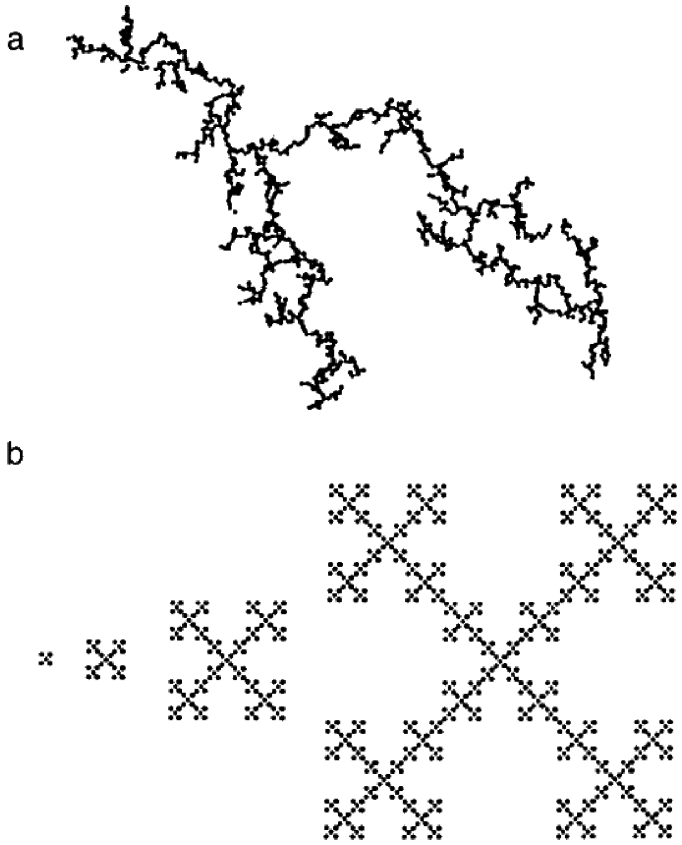

Fig. 7.18 (**a**) Fractal aggregate, constructed by computer-simulated diffusion-limited aggregation. Fractal dimension D = 1.44 (**b**) deterministic Vicsek fractal constructed of 1, 5, 25, and 125 basic units respectively. Fractal dimension D = −1.465. (Reprinted from *Journal of Colloid and Interface Science*, Volume 185, Beelen, T. P. M., Shi, W., Morrison, G. R., Van Garderen, H. F., Browne, M. T., Van Santen, R. A., Pantos, E., Scanning transmission x-ray microscopy; a new method for the investigation of aggregation in silica, pp. 217–227; Copyright (1997), with permission from Elsevier)

However, the number of points (or particles), N, in the fractal is increasing only fivefold (instead of the expected ninefold increase as Euclidian geometry would dictate) and this leads to a relationship between N and R_f that follows a power law $N \sim R_f^{D_f}$, and that links the two parameters via a logarithmic relationship with D_f being the fractal dimension that will be expressed as

$$D_f = \log N / \log R_f \tag{7.39}$$

In the example above we can than calculate D_f as $\log 5 / \log 3 = 1.465$ thus leading to a non-integer "fractal" dimension.

When we are looking at the aggregation of primary particles, we have to take into consideration that the produced fractal objects have fractal dimensions that are related to the number of primary particles. The only direct method to determine the fractal dimension is to analyze images obtained from high-resolution microscopy or from scattering experiments and these approaches will be explained briefly in a later section.

7.4.3 Ostwald Ripening

We have mentioned before briefly the Ostwald step rule. However, here we will slightly expand on the Ostwald ripening concepts. By IUPAC definition, Ostwald ripening is: "The growth of larger crystals from those of smaller size which have a higher solubility than the larger ones."

The history of the theory of Ostwald ripening goes back at least to Ostwald's observations in 1900 (Ostwald, 1900). The first analytical solution for this phenomenon, however, was presented in two papers by Lifshitz and Slyozov (1961) and Wagner (1961) and is thus often found in the literature as the LSW theory. Modern theories are often categorized by how they differ from LSW; yet more recently there have been a large number of papers extending and improving upon the work of LSW, including work by Voorhees and Glicksman (1984), Voorhees (1985), Tokuyama et al. (1986) and Yao et al. (1993, see also Fig. 7.19) with the latter being one of the best reviews on Ostwald ripening.

After small clusters/particles form initially in a system, they will slowly disappear except for a few that grow larger, at the expense of the small units. The smaller ones will act as "nutrients" for the bigger and possibly more ordered particles or crystals. As the larger units grow, the area around them is depleted of smaller units and this is the basis of the Ostwald rule. Thus Ostwald ripening involves a mass transfer from smaller particles to a lesser number of larger particles and this results in a net decrease in the number of particles in the system with the driving force for the process being the change in interfacial energy of the particles (Nielsen, 1964). At a given degree of supersaturation of the starting solution, δ, the critical radius of the resulting particles, r, can be expressed as a function of the molar volume, ν, the bulk solubility, S_{eq}, the density, ρ, and the concentration, a_c, and this represents the Gibbs-Kelvin equation (see also Steefel and Van Cappellen, 1990):

$$r = 2\rho\nu/R_U\, T \ln(c/S_{eq}) \tag{7.40}$$

Ostwald ripening is a spontaneous process that occurs because larger units are more energetically favored than smaller ones. While the formation of many small particles is kinetically favored, (i.e., they nucleate more easily) larger particles/clusters/crystals are thermodynamically more favored. Therefore, from a purely kinetic point of view to nucleate small particles is by far easier. This is specifically true as small

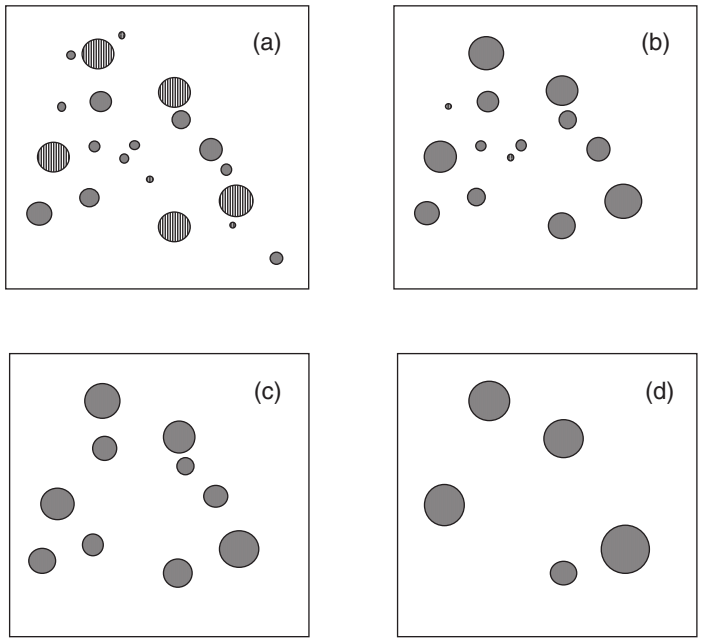

Fig. 7.19 Sketch showing an Ostwald-ripening phenomenon in two dimensions in a time evolution scenario (**a**–**d**). The total number of particles decreases and their average radius increases, but the volume fraction remains constant (Reprinted from *Physical Review B*, Volume 47, Yao, J. H, Elder, K. R., Guo, G., and Gran, M., Theory and simulation of Ostwald ripening, pp. 14110–14125; with permission from the American Physical Society)

particles have a larger surface area to volume ratio and the molecules on the surface of a poorly ordered small particle are energetically less stable than the molecules in the interior. Large particles/crystals have a much larger volume to surface area ratio and as such they represent a lower energy state. Thus, many small particles will attain a lower energy state if they will "transform" into large units.

However, in many systems Ostwald ripening is not occurring. If we want to understand why this happens we have to first think of the fact that the nucleation of a large number of small particles will affect the supersaturation of any solution. This in turn will prevent the formation of large particles or crystals. Basically if supersaturation is the controlling factor and the reactions are fast it is often the case that large particles/crystals never get a chance to appear and often the smaller ones just aggregate but do not grow. The process of Ostwald ripening governs is naturally linked to the "speed" or rate of nucleation and usually it governs the late stages of a first-order phase (trans-) formation. This phenomenon results from the elimination of regions of high curvature in favor of regions of low curvature, thereby decreasing the net interfacial energy through the elimination of surface area. Since this behavior results in an increase in the scale of the patterns formed in such systems, Ostwald ripening is often referred to simply as coarsening.

7.4.4 Example: Silica Aggregation

We finish this section of the chapter with an example illustrating the aggregation behaviour and fractal growth of silica colloids. An introduction to silica origometization and colloid formation kinetics has been introduced in Chap. 1 (Brantley and Conrad) while here the discussion will focus more on aspects of silica aggregation and fractal dimensions.

Soluble silica or monomeric orthosilicic acid (H_4SiO_4), is comprised of a silicon atom tetrahedrally coordinated to four hydroxyl groups and it remains stable in solution at 25° C as long as its concentration is below the equilibrium concentration for amorphous hydrated silica (at 25° C ∼ 100–125 ppm; Iler, 1979, 1980). In active subaerial geothermal systems where concentrations of dissolved silica can reach up to 1,000 ppm (i.e., highly supersaturated), once these solutions reach the surface autocatalytic polycondensation/polymerization of silica monomers will be induced.

The initial step of silica precipitation (oligomerization) is described in several elementary reactions in Chap. 1 (Eqs. (7.23)–(7.26)). Overall the first step in the process occurs via the condensation of two silicic acid molecules and the expulsion of water:

$$H_4SiO_4 + H_4SiO_4 \Leftrightarrow (HO)_3Si - O - Si(OH)_3 + H_2O \qquad (7.41)$$

Following the formation of Si-O-Si siloxane bonds, and of the first critical nuclei, the next step is growth at the expense of other monomers, dimers, etc. (i.e., Ostwald ripening) followed again by growth to form either large nanoparticles (several hundred nm up to 1 μm) or aggregation (e.g., Iler, 1979, 1980; Perry, 2003; Benning et al., 2004a, b and 2005; Icopini et al., 2005; see also Chap. 1 (Eq. (7.69) and associated discussion).

In most geothermal waters, nucleation will occur both in solution but also on any available surface (i.e., both homogeneous and heterogeneous processes). Thus the resulting amorphous silica phase will be highly variable from site to site. Microscopic observations of field-derived samples indicate that the first silica precipitates are made up of tens of nanometer-sized spheroids. These nuclei are bigger than the critical nucleus estimated for experimental silica precipitation studies (∼3 nm, Icopini et al., 2005; Tobler et al., 2006) and thus it is asserted that the observed particles in the field-derived samples represent already aggregates of smaller nuclei. However, it is asserted that once such initial nuclei have formed this will be followed by aggregation, growth or Ostwald ripening. Yet, due to the infinite resupply of aqueous monomeric silica in the geothermal solution, nucleation will be a continuous process. Many experimental studies – both with purely inorganic or mixed organic inorganic solutions – have shown that once silica nanoparticles formed in solution, their growth, ripening or aggregation behavior is strongly affected by pH, ionic strength, temperature (Iler, 1980; Rothbaum and Wilson, 1977; Makrides et al., 1980; Weres et al., 1981; Icopini et al., 2005, Tobler et al., 2006), surfactant type and concentration (e.g., Boukari et al., 1997; Green et al., 2003). Furthermore, the structure and complexity of the formed aggregates can be described by applying concepts of fractal geometry (Pfeifer and Obert, 1989; Lin et al., 1990) with

the condensation of primary monomers into nanoparticles or aggregates producing fractal objects with a fractal dimension D_f.

As mentioned above, this fractal dimension, D_f, is related to the number of primary particles (N) by a power law $N \sim R_f{}^{Df}$, where R_f is the radius of the aggregate spatial dimension which in turn is related to $N \sim R_f{}^3$ (see also Eq. (7.39)). We have also learned that two regimes (diffusion- and reaction-limited aggregation; DLCA and RLCA) can be defined. For silica in a DLCA case, the theoretical values of D_f have been confirmed experimentally (light and x-ray scattering methods) to be $D_f = 1.7$–1.8 (Martin et al., 1990; Lin et al., 1990). On the other hand, in a RLCA case, which is governed by slower condensation, the concentrations of the encountered reactant pairs will be maintained at equilibrium and a significant repulsive barrier will make the "sticking probability" upon particle-particle interaction to be less than 1. Numerous experimental investigations of reaction-limited silica aggregation processes have produced aggregates with $D_f = 2.1$–2.2 indicating that a more compact aggregate structure is formed under conditions of slow aggregation (Martin, 1987; Lin et al., 1990). In general, these fractal dimensions can be associated with a kinetic process, and low fractal dimensions are equated with rapid (diffusion-limited) aggregation and high fractal dimensions with slower (reaction-limited) aggregation.

Most experimental and modeling studies have quantified rates, fractal geometries and mechanisms from either purely inorganic or organic experiments. However, recently Benning et al. (2004b and 2005) derived aggregation rates and mechanisms from a mixed organic – inorganic system. They have studied the changes in infrared spectral features in silicification experiments in the presence of cyanobacterial cells and expressed the change in infrared signals as a function of concentration. The data was fitted using a modified Avrami approach (as described in a previous section and Eq. (7.32)) and, although from their experiments a fractal dimension for the forming silica aggregates can not be evaluated directly, it is possible to infer a fractal dimension from the value for the constant related to the aggregation mechanism, n (Eq. (7.32)). This can be achieved by comparing their values for n, to theoretical values derived by Hulbert (1969) and Gedde (1995). These authors have shown that for a DLCA process and for a particle of low but complex geometry (one or two-dimensional; e.g., fibre or sheath) the values for n vary between 0.5 and 2 with the highest values representing two-dimensional growth, while for a spherical (three-dimensional) macromolecule growing via DLCA, the n value will vary between 1.5 and 2.5. Alternatively, if the same three-dimensional spherical particle grows via a RLCA mechanism, values of 3–4 are expected for n. Based on these theoretical evaluations and using the values for (n) derived by Benning et al. (2004b) it can be concluded that the nucleation, growth and aggregation of silica nano-spheres on cynanobacterial surfaces occurs via a two stage process. Initially when silica polymerizes, a fast, diffusion-limited process dominates (n, values of 1.8 and 2.2). This is followed by a slower, reaction limited process (n of 3.4 and 3.8). The initial step starts with the polycondensation of silica monomers to form small three-dimensional particles and this is than followed by the aggregation of these nanoparticles via a three-dimensional, reaction-limited mechanism.

This aggregation process follows on from the first steps in the oligomerization reaction described in Chap. 1 (Eqs. (7.23)–(7.26)).

Lastly, we briefly compare the aggregation mechanisms derived from the cyanobacterial-silica system (Benning et al., 2004b and 2005) with aggregation in purely inorganic or ionic low molecular weight surfactant (e.g., via the Stöber process, e.g., Stöber et al., 1968). The Stöber process is used in many industrial processes to produce large quantities of highly monodispersed silica colloids that have a wide range of applications. Using an organic silica solution (TEOS, tetraethylorthosilicate) and a surfactant to induce the nucleation, results in a particle size that is relatively small (10^{ns} of Å to max. 10^{ns} of nm) and that has a narrow particle size distribution. However, in the TEOS case equilibrium is usually reached faster (1–1,000 sec) than in any inorganic process, In addition, in such reactions the process is purely diffusion-limited (Pontoni et al., 2002). At a first glance it seems that in both cases (inorganic and organic mediated silica formation) the observed mechanisms that control silica formation are similar. However, in the Stöber process the nucleation and aggregation of silica particles is dependent on a variety of parameters, including the hydration level of the starting organic silica solution (TEOS), the concentration and nature of the solvent (ethanol or methanol etc), the temperature and the salt or impurity concentrations. In addition, it is worth mentioning that in terms of size and fractal dimensions Martin (1987) showed that in the inorganic process when growth was induced from a 1% SiO_2 solution (using Å-size silica seeds) a slow aggregation to 30–700 nm large spherical particles occurred and the particle radius increased exponentially with time via diffusion-limited process, producing a fractal dimension $D_f = 2$. At lower silica concentrations (0.01–0.01 wt % SiO_2) – conditions that are more similar to natural geothermal environments – nano-spheres of about $10^2 - 10^3$ nm grew, but a switch from an initial diffusion- to a reaction-limited mechanisms with a fractal dimension $D_f = 1.7$ (Martin et al., 1990; Lin et al., 1990) was observed. Although, these fractal dimensions are lower, this latter process seems comparable to the aggregation reaction observed in the cyanobacterial silicification reactions (Benning et al., 2005).

7.5 Process Quantification: Direct versus Indirect Methods

The full quantification of the chemical and physical parameters governing nucleation, growth or aggregation reactions requires the use of several complementary approaches which may include simple batch or flow through reactors combined with detailed chemical analyses of the solutions or solid phases, or a combination of conventional or synchrotron-based scattering, diffraction or spectroscopy linked with high resolution microscopy. Some modeling, as well as experimental techniques regarding growth processes at surfaces, has been introduced in Chaps. 2 and 3 and thus below we introduce applications linked to processes occurring in solution. We will focus first on imaging techniques and then delve into x-ray scattering and absorption techniques and applications of these in earth sciences; the main driver for

this approach is that, as we will illustrate, this combination of techniques has been the most helpful in nucleation/growth/aggregation kinetic studies.

It is important to understand that many of the parameters needed for molecular models (i.e., cluster size, nucleation densities, nucleation or growth rates, critical nucleus size as well as cluster size distribution) cannot be quantified in any other way but by careful experimentation and thus the techniques described below are unique and crucial in providing molecular level base data that can than be applied to more and more complex molecular models (i.e., Chap. 2). Only the advances in the techniques described below have allowed the scientific community, in the last decade or so, to better understand and quantify molecular level reactions linked to the formation of particles in solution. For example, if we want to know what the nature of a heterogeneous nucleation site is, whether we really have true homogeneous nucleation, or what the link between aggregates formation and volume change is, etc., we cannot rely on molecular models alone but need the fundamental and ultimately better quantitative data that we can only reliably obtain from experiments. In addition, we will describe some aspects of the developments in *in situ* and *real-time* experimental approaches that allow us to follow and quantify the parameters that affect reactions as they occur (e.g., particles growing in solution at fast time scales etc.). This combination of approaches will ultimately help determine mechanisms of reactions and thus allow the selection of more useful models for predictive purposes for systems beyond those accessible to experimentation.

7.5.1 Imaging Techniques

In any study dealing with phase formation, in a first and very important step, the information gained from solution analyses and the imaging of end-product solid phases can give a good approximation of processes linked to the nucleation or growth reactions. A plethora of modern high-resolution imaging techniques based on non-contact mode principles can be used for the quantification of nucleation and growth on surfaces and some of these non-contact mode surface imaging techniques have been introduced in Chap. 3. However, many of these techniques are particularly adequate for processes and reactions on surface yet only in part useful when dealing with phases that grow free in a solution matrix.

Some of the key problems with imaging of phases forming in solution are related to the fact that in order to produce high-quality and high-resolution images, the samples often have to be dried or coated and subsequently submitted to high vacuum conditions, and thus it is not possible to truthfully determine their state *in situ*, i.e., in equilibrium with the solution in which they have formed. For several systems this is not a problem; for example, drying of ceramics or hard sphere ionic materials does not change upon dehydration or organic solvent evaporation. However, in systems where reactions are followed in aqueous solution drying and dehydration may induce changes in surface properties as well as aggregation. In addition, from such studies only modest amounts of accurate kinetic data can be gained because often only a few intermediates or end-products can be imaged. However, some novel

developments in this field are described below and they will show that high-resolution imaging is a most valued tool in the research field of nucleation and growth of phases because any studies involving phase formation are "blind" without the help of imaging techniques.

A technique that has been used in recent decades to image inorganic or biological specimens from experiments in solution is environmental scanning electron microscopy (E-SEM). Note this is a surface observation technique so samples will only partly be in equilibrium with the solution but, E-SEM requires no coating or high vacuum and thus imaging can be done with no sample treatment. However, again the limitations in resolution ($\sim$100 nm) and the need for high voltage and large beam size (usually $\sim$3–5 μm) for elemental analyses, usually prevents detailed elemental analyses of small newly formed particles using the E-SEM (i.e., Goldstein et al., 2003 and references therein).

High-resolution transmission electron microscopy (HR-TEM) is another imaging technique that has been extensively used in characterizing precipitated phases both in the chemical, earth, materials sciences or biological sciences (e.g., McLaren, 1991; Buseck, 1992; Hochella and Banfield, 1995; Banfield and Zhang, 2001; Fultz and Howe, 2002; Hayat, 2004). The main limitations of conventional TEM is the need for sample handling (depositing a liquid sample on a grid and drying, or embedding and microtoming), as well as beam damage from the high voltage used in imaging and naturally the high vacuum requirement.

The new generation of transmission electron microscopes, are based on field-emission gun electron source technology (both FEG–SEM, see Fig. 7.1b, and FEG–HR–TEM), and are usually equipped with energy dispersive spectrometers that are capable of both high-resolution imaging (e.g., by Z contrast imaging) as well as fine probe chemical analysis thus allowing elemental analysis and mapping of the formed phases. In addition, they usually have good capabilities to do high-resolution diffraction (selected area electron diffraction, SAED), spectral analyses (energy-filtered, EF-TEM, or electron energy loss spectroscopy, EELS) or even high angle annular dark field scanning TEM (HAADF-STEM) combined with energy dispersive spectrometry (EDX). All these techniques have been successfully applied to earth materials to characterize both the crystallographic and elemental composition as well as beam damage issues related to small particles (see for example: Buseck, 1992; Banfield and Zhang, 2001; Hochella, 2002a and b; Brydson, 2001; Utsunomiya and Ewing, 2003; Palenic et al., 2004, Pan et al., 2006).

The best SEM and TEM-based approaches for nucleation and growth imaging in an "as-*in-situ*-as-possible" mode are based on fast cryo-quench freezing of samples. These techniques, that will be described in brief below, have in part overcome some of the limitations related to *in situ* and realtime "capture" and imaging of precipitates at both high spatial- and spectral resolution because ultra-rapid cryo-freezing is extremely well suited for quenching samples of complex mixtures of fluids and solids (both inorganic and biological) that have a high water- (or solvent) content. Once flash-frozen, such samples can subsequently be imaged in cryo-mode, using special cryo-transfer stages and TEM systems that can run at -165°C. Both cryo-SEM and cryo-HR-TEM can be useful when phases need to be imaged during a

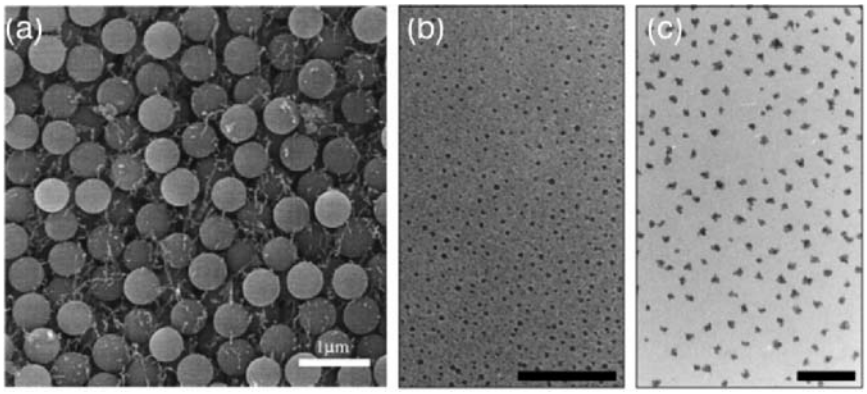

Fig. 7.20 (**a**) Cryo-SEM image of frozen stable silica suspension. Small filaments between particles are from the high concentration of surfactant used (Reprinted from *Journal of Non-Crystalline Solids*, Volume 248, Wyss, H. M., Huetter, M., Mueller, M., Meier, L. P., and Gauckler L. J., Quantification of microstructures in stable and gelated suspensions from Cryo-SEM, pp. 340–346; Copyright (2002), with permission from Elsevier) (**b**) and (**c**) cryo-TEM images of iron dispersions with increasing average particle radius; (**b**) radius $= 2.1 \pm 0.3$; (**c**) radius $= 6.9 \pm 1.0$. Scale bar in latter two images $= 100$ nm. (Reprinted from *Nature Materials*, Volume 2, Butter, K., Bomans, P. H. H., Frederik, P. M., Vroege, G. J., and Philipse, A. P., Direct observation of dipolar chains in iron ferrofluids by cryogenic electron microscopy, pp. 88–91; Copyright (2003), with permission from Macmillan)

process. Cryo-SEM techniques have extensively been used in earth science related research, specifically in freeze-fracture imaging of rock deformation processes by salt formation at grain boundaries (i.e., Mann et al., 1994; Samson and Walker, 2000; Schenk et al., 2006). However, cryo-SEM is naturally limited by resolution (Fig. 7.20a; Wyss et al., 2002) and thus not very suited for phases at the nanoscale.

Advances in cryo-TEM capabilities (both in terms of speed of quenching and high-resolution imaging) have made this a new tool that is extremely useful in following processes of nucleation and growth as a function of time and as *in situ* as possible. For example, envisage a reaction where two aqueous solutions are mixed and new phases nucleate and grow in the mixture. If at specific time frames in the reaction a drop (usually $< 10\,\mu$l of a very dilute sample) of such a mixture is pipetted onto a TEM grid that is held in a vitrobot (see below) this will form a thin liquid film that is then immediately cryo-quench frozen (this can be achieved in less than 1 s) by plunging it into liquid propane or ethane. A vitrobot is basically a guillotine plunging device that can instantly vitrify a sample deposited on a TEM grid. After depositing the sample the vitrobot automatically blots the liquid on the grid with filter paper producing a sample that is thin in the middle and thicker at the edges of the holes. This grid is than plunged into the cryo-solution of choice and this way only vitreous ice is formed and this vitrification prevents phase separation and ice crystal growth. Propane or ethane is usually used for vitrification because of their high boiling points and high thermal conductivity (0.22 and 0.24 J/m s K). These solvents are much better than liquid nitrogen, which has a higher conductivity

(0.13 J/m s K) yet in some cases liquid nitrogen is also used if the sample may interfere with other cryo-preservation solutions (i.e., some other organics may dissolve in propane or ethane). However, when a warm object is plunged into liquid nitrogen for vitrification usually a thin boiling film and a thin insulating layer of nitrogen gas is produced (Leidenfrost phenomena), thus reducing drastically the cooling rate. For this reason propane and ethane are used as they allow for a faster and more reliable vitrification. Once the samples are vitrified they are transferred to a liquid nitrogen dewar for storage and than imaged at cryogenic temperatures (i.e., -165° C) using a TEM cryo-stage. This cryo-freezing process naturally also arrests any thermal or mechanical diffusion of the phase on the time scale of the vitrification thus allowing for quasi-real time *in situ* observations of nucleation and growth processes. A discussion of the advantages or disadvantages of the various cryo-preservation methods can be found in Fouchandour et al. (1999) and Frederik et al. (2002) and extensive literature on cryo-TEM imaging techniques can be found in Binks (1999). Here we mention two studies that were linked to earth based materials (silica and iron oxides) and that have used flash-freezing of the reacting solution and subsequent cryo-TEM imaging. These are (a) TEOS-based silica particles (Bailey and Macartney, 1992) and (b) surfactant-based magnetite iron oxide nanoparticles (Fig. 7.20b and 7.20c; Butter et al., 2003). However, many more studies are in progress and *in situ* and realtime high-resolution cryo-imaging will become more and more a vital tool in studies dealing with nucleation and growth of mineral phases from solution.

A vision for the future of in situ and realtime imaging and spectral/diffraction analyses of nucleation and growth processes in solution would be to combine cryo-quench freezing with a (cryo-?) focused ion beam (FIB) sample handling system (e.g., Heaney et al., 2001) and high-resolution cryo-TEM imaging and spectral analyses to study freshly precipitated samples in various stages of the nucleation and growth process. Such a combination would tremendously improve our ability to follow nucleation and growth reactions as they occur and together with the techniques explained below we could than get a more quantitative and realistic understanding of these processes and of the mechanisms that control them.

7.5.2 SAXS/WAXS

7.5.2.1 General Introduction and Basic Concepts

The size, shape and crystallinity of "particles" are of fundamental interest for the understanding of microstructure of heterogeneous materials or complex inorganic or biological systems. Small-angle and Wide-angle x-ray scattering (SAXS/WAXS) are key techniques used in the study of inorganic and biological particles that exhibit poor structural ordering or nanosize properties. Overall, the larger the diffraction or scattering angle the smaller the length scale that can be probed, and thus WAXS is used to determine crystal structure on the atomic length scale while SAXS is used to explore structure on the nanoscale. Applications are as wide-ranging as alloys, melts, polymers, biological macromolecules, nanoparticulate or porous mate-

rials (e.g., Glatter and Kratky, 1982; Singh et al., 1993; Svergun and Koch, 2003; Waychunas et al., 2005; Shaw et al., 2000 and references therein). SAXS and WAXS can be performed with different x-ray sources. Synchrotron radiation emitted by particle accelerators provides an added advantage over laboratory sources in that the emitter source has a high flux and brightness. For SAXS this is specifically important as it provides a capability of low divergence, thus allowing SAXS measurements to be taken at low angles. This in turn permits high quality data to be extracted for particle formation reactions and specifically the kinetics and mechanisms of processes can be followed *in situ* (i.e., in equilibrium with the reacting medium) and in realtime (with time resolutions down to milliseconds). SAXS has been extensively used in the last two decades for the study of biological macromolecules under near physiological conditions but not necessarily for kinetic studies (see for example review by Svergun and Koch, 2003). In inorganic systems, the combination of SAXS and WAXS is particularly important in systems where the structural changes, for example, linked to nucleation, growth or crystallization of particles respond to variations in external conditions (i.e., chemical or physical changes) and reactions need to be followed *in situ* (i.e., in solution or melt phase as solid state reactions) due to changes that occur in the pathways and progress of the reactions.

A simple and comprehensive textbook on SAXS/WAXS theory, data acquisition, processing and interpretation is sadly lacking. We refer the reader to several books or review papers that detail the basics of the SAXS/WAXS theory (e.g., Guinier, 1939; Guinier and Fournet, 1955; Glatter and Kratky, 1982; Glatter, 1992; Bras et al., 1993; Bras and Ryan, 1998). Only in the last decade have SAXS and WAXS been also applied to geological or environmental problems and a recent review applied to geomedia is discussed in Waychunas (2001) and Waychunas et al. (2001).

7.5.2.2 Basic Concepts

A schematic diagram, idealized scattering patterns and the relevant equations representing a dilute and non-dilute system are shown in Fig. 7.21. The simple way to describe scattering of x-rays is to think that scattering occurs due to the electron density contrasts at the samples. Overall, the x-ray scattering amplitude represents the Fourier transform of the electron density distribution in the matrix. The scattered intensity, $I(q)$, is measured in terms of the scattering vector, q, which in turn is a function of the scattering angle 2θ, and the radiation wavelength λ:

$$q = 4\pi \sin\widetilde{\theta}\lambda. \tag{7.42}$$

and at small angles and for homogenous particles the scattered intensity $I(q)$ can be expressed as:

$$I(q) = N/V\ V_p^2(\rho_p - \rho_o)^2 P(q)\ S(q) \tag{7.43}$$

where N represents the number of scatterers per volume of V of sample, V_p represents the volume of the individual scattering entity, ρ_p and ρ_o the density of the particle and density of the matrix, while $P(q)$ represents the form factor

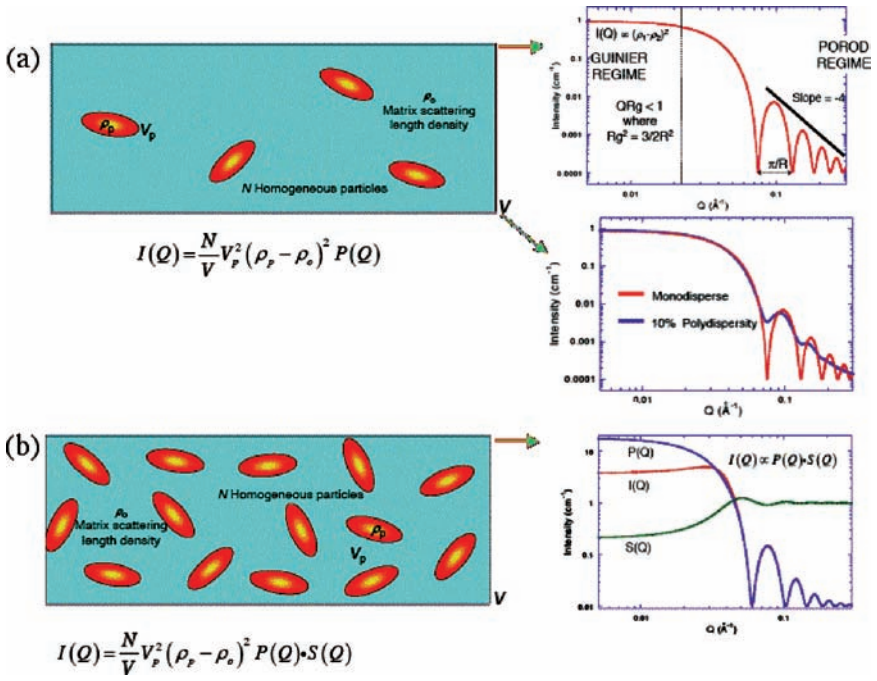

Fig. 7.21 Schematic diagram, relevant equation and corresponding scattering patterns for a dilute (**a**) and a concentrated (**b**) system; in (a) shown is also the effect of polydispersity in a dilute system. Details see text. (Modified and reprinted with permission of Jamie Shulz, ANSTO, Australia)

(containing information about shape, size and internal structure of the particles) and $S(q)$ represents the structure factor (containing information of the interactions between particles and their spatial arrangements). Both $P(q)$ and $S(q)$ are dimensionless parameters that are used in dilute systems $[P(q)]$ and non-dilute systems $[S(q)]$ for the evaluation of properties linked to the scatterers in the matrix (Fig. 7.21 and below).

In dilute systems there are no particle-particle interactions (Fig. 7.21a left panel) and thus the total scattering intensity is the sum of the individual particle scattering, and the structure factor, $S(q)$, does not play a role (see equation in Fig. 7.21a). As mentioned above, to a first approximation, the scattering curve is simply a Fourier Transform of the scattering density, which is related to the number of electrons (for x-ray scattering) in a particular region of space, and thus to the structure that causes the scattering pattern. In a dilute system (Fig. 7.21a, right side) the scattering pattern contains information about the idealized radius of gyration, R_g, which represents the distance from the "centre of the scattering density". This R_g is not equal to the true radius, but it can be related to the true radius of the particle depending on the particle shape (e.g., for spheres $R_g^2 = 3/5\,r^2$; see Guinier, 1939 for other shapes). In a purely monodispersed systems, the best way to evaluate the particle size is from the minima in the scattering patterns (Fig. 7.21, right side). Although the Guinier approximation does not strictly apply to monodisperse systems, one can also get an estimate of the

R_g from the slope of the scattering pattern in the lowest q region, $q \rightarrow 0$ (Guinier regime) via:

$$\ln I(q) = \ln I(0) - 4\pi^2/\lambda^2 R_g^2 (2\theta)^2 \tag{7.44}$$

Overall, the Guinier approximation can be viewed as "the poor-man's approximation" that can be applied to systems that have a certain degree of polydispersity or when the measured q range does not allow the evaluation of the minima in the spectra at higher q. The intensity at $q = 0, I(0)$, is also related to the volume fraction of t5e particles within the sample. Complementary to this, in the high q region (Porod regime) information about the interfaces present in the sample is contained and here the scattered intensity is expressed as (see for example Bras et al., 2005):

$$I(q) = K_1 + K_2/q^{\alpha} \tag{7.45}$$

where K_1 represents the thermal background and K_2 is the Porod constant which is linked to the dimension and surface roughness of the particle while the exponent α is linked to the slope of the scattering curve in the Porod region (Fig. 7.21a). Lastly, the decay in intensity of the scattering in the Porod region also contains information about the degree of polydispersity in the system (right side, middle panel Fig. 7.21; and Megens et al., 1997).

In a dilute monodispersed system (where $P(0) = 1, S(q) = 0$ and $P(q) \neq 1$), the form factor $P(q)$ basically represents the link between the reciprocal space of the measurement and the real space of the particle and can be expressed as:

$$P(q) = 4\pi \int_0^{\infty} p(r)(\sin(qr)/qr)\, dr \tag{7.46}$$

where $p(r)$ is the pair distribution function, or PDF. PDF analysis is a method of extracting structure-related information from SAXS and WAXS data and the evaluation takes into account both the Bragg (in non-dilute systems) as well as diffuse scattering (in dilute systems, related to short-range order effects). This sensitivity to the local structure has made the PDF analysis the tool of choice for structural studies of amorphous materials (e.g., Glatter, 1992; Bras and Ryan, 1998 and references therein). The scattering length distribution function $p(r)$, which is equal to the total scattering length of the atoms per unit volume of matrix are shown for various particle shapes in a Fig. 7.22a.

We can look at a PDF plot essentially as a histogram of all of the distances, d, within a particle and it can be calculated by an indirect Fourier transform of the full scattering pattern. From a PDF, the R_g can also be derived and this is usually more accurate than from the Guinier approximation mentioned above because it uses the entire scattering pattern, not only the lowest q angles. However, one needs to be careful as most solutions (with the exception of some biological samples) will indeed not contain 100% mondispserse particles. Overall a $p(r)$ versus intra particle length plot contains the same information as the scattering intensity $I(q)$, but the real space representation (i.e., the inverse Fourier transform) is more intuitive. A

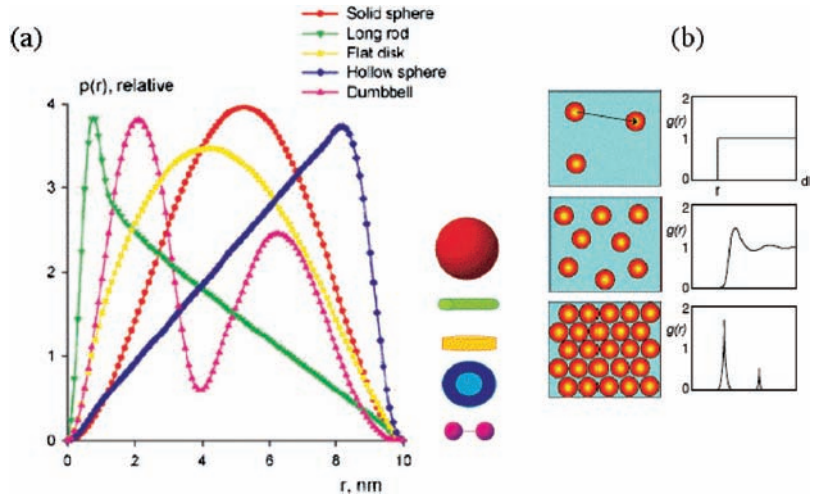

Fig. 7.22 (**a**) Idealized SAXS profiles of various geometrical bodies in dilute monodispersed systems, the corresponding p(r) and particle shapes as a function of particle radius (after Svergun and Koch, 2003) and (**b**) schematic diagrams of the pair correlation functions G(r) for a system at a series of increasing concentrations plotted in real space. (Modified and reprinted with permission of Jamie Shulz, ANSTO, Australia)

few possible curve shapes of $p(r)$ and the corresponding particle shapes are shown in Fig. 7.22a. For example, spherical particles display Gaussian-shaped $p(r)$ curves with a maximum at about the maximum radius (see curve for solid spheres), while elongated particles have skewed distributions with a maximum at small distances which can be related to the radius of the cross-section of the elongated particle (curve for long rod); lastly, particles consisting of well-separated subunits (curve for dumbbell) can display multiple maxima, the first one representing the intrasubunit distances, with the other maxima giving information about the separation between the subunits (dumbbell example).

If the system is polydispersed, the scattering curve can yield information about the average idealized particle radius, R_g (from the Guinier regime), and if the final shape of the particles in a system is known (via for example quantification with a different method, e.g., high resolution imaging see above) the R_g can be linked to the real space average particle radius and particle size distribution. However, because the scattering intensity correlates with the shape and the size of the forming particles the integral of I(q) is defined as the invariant Q, which is sometimes also called "the Porod invariant" (although this is not a constant – see examples). Q, basically represents the total scattering power law of the sample and it can be used to quantify the electron density contrast independent of particle shape or number and it is specifically useful in systems that are not monodispersed and that contain mixed particle shapes; where Q will change as a function of reaction time and changes in particle properties (see examples below). For example for a two-phase system, Q

can be expressed as:

$$\mathrm{Q} = \int (\mathrm{I}(q)q^2 \mathrm{d}q = \phi(1-\phi)(\Delta\rho)^2 \tag{7.47}$$

where $\Delta\rho$ is the electron density difference, q the scattering vector and ϕ the fraction of one phase with a maximum predicted when ϕ is equal to 50%, thus allowing the proportions of the different shaped particles to be evaluated.

Finally, for non-dilute systems, where inter-particle effects play an important role (see examples below), the structure factor $[\mathrm{S}(q)]$ is used for evaluation of the scattering parameters (Fig. 7.21b and 7.22b). The $\mathrm{S}(q)$ is related to the real-space pair distribution or correlation function, $G(r)$, via the Fourier sine transform and it includes effects due to strain and disorder effects. It can be expressed as:

$$\mathrm{G(r)} = 2/\pi \int_{\mathrm{o}}^{\mathrm{x}} \mathrm{q}[\mathrm{S}(q) - 1] \sin(qr)\ \mathrm{dq} \tag{7.48}$$

where $\mathrm{G}(r)$ describes the "local" density of particles and the spatial arrangement defined by the direct as well as indirect interactions between particles (i.e., electrostatic interactions). As we mentioned above, in dilute systems $\mathrm{S}(q)$ does not play a role as it is equal to one (no particle – particle interactions) while in non-dilute systems it differs from one and can sometimes be used to derive the PDF via the equation for $\mathrm{G}(r)$. A simple schematic of the $\mathrm{G}(r)$ as a function of the complexity of the system can be seen in Fig. 7.22b and specific examples are discussed below.

7.5.2.3 Examples of Nucleation and Growth SAXS/WAXS Analysis

As a first example we discuss the quantification of the reaction processes linked to the formation of CdS nanoparticles in dilute solutions based on data from *in situ* and real time synchrotron-based SAXS experiments (Meneau et al., 2003). The growth of CdS particles from solutions that were mixed just prior to commencement of the experiments $(\mathrm{t_o} = 3\,\mathrm{min})$ is shown as a time-resolved 3D stacked plot in Fig. 7.23a. The gradual increase in intensity in the low q area and the three maxima observed after 6 h (Fig. 7.23b) indicating changes in the scattering intensity, $\mathrm{I}(q)$, which can be linked to the emergence of a form factor (i.e., a change in particle shape) and show a monodisperse product with no aggregation component. Furthermore, at $\mathrm{t_o}$ already particles with an $\mathrm{R_g}$ of 90 ± 9 Å are present indicating an almost instantaneous nucleation of the first particles (Fig. 7.23c). After about 45 min $\mathrm{R_g}$ reached a value of 133 ± 13 Å (vertical dashed line in Fig. 7.23c) and the observed change in slope of $\mathrm{R_g}$ (note two straight line fits) indicate a change in the growth process. The observed change demonstrates a switch from an initial spherical particle (before $\mathrm{t_o} + 40\,\mathrm{min}$) to a cylindrical particle (after $\mathrm{t_o} + 40\,\mathrm{min}$). Finally, the relationships between $\mathrm{R_g}$ and the spherical and cylindrical radii ($\mathrm{R_s}$ and $\mathrm{R_c}$) and the cylinder length,

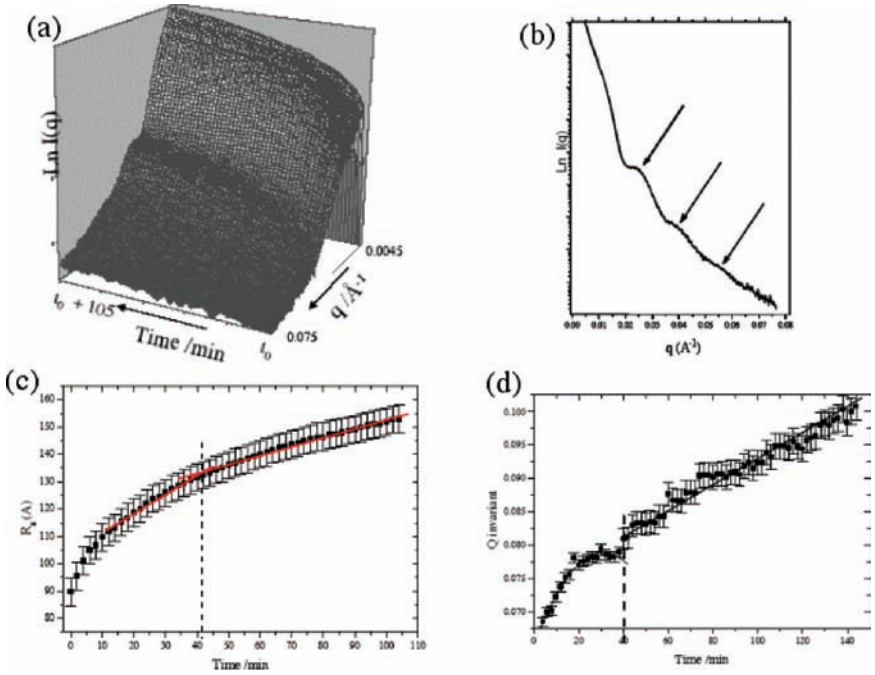

Fig. 7.23 (**a**) 3D plot of stacked *in situ* SAXS data for the formation of CdS nanoparticles (**b**) SAXS profile showing First, Second and third order maxima (arrows) suggesting highly monodispersed particles (**c**) Time resolved plot of the changes in the Guinier radius of gyration, R_g, for the CdS forming reaction; A change in slope at ~ 40 min (vertical line) indicates a change in growth process (details see text); (**d**) Plot of invariant, Q versus time showing the change from spherical to cylindrical crystal growth (details see text). (After Maneau et al., 2003, Reprinted with permission from IUCr)

$L_c[R_g^2 = 3/5\,R_s^2$ and $R_g^2 = (R_c^2/2) + (L_c^2/12)]$, were used to determine the real dimensions of the particles. Modeling of the data showed that the R_g of the spherical particles was about 10 Å smaller that that evaluated from the Guinier regime (81 ± 16 Å versus 90 ± 9 Å), while the cylindrical particles had a final R_g of 271 ± 22 Å which was slightly bigger than the ones evaluated before from the Guinier plot. This difference was interpreted as a small contribution of polydispersity. The observed change in shape also makes sense when compared with DFT calculations (Hamad et al., 2002) and with the expected shape of the end CdS crystals (wurtzite, from standard XRD). Initially a spherical, poorly crystalline phase nucleates and grows and after ~ 40 min the growth into standard wurtzite structure (cylindrical shape) occurs. The change from spherical to cylindrical growth is also supported by the Porod invariant, Q, which also indicates at ~ 40 min a change in growth process (Fig. 7.23d).

Although Meneau et al. (2003) derived the change in R_g versus time (Fig. 7.23c), from the Guinier region; they could not evaluate the pair size distribution function. As mentioned above in a dilute system, where no interparticle intereactions exist (i.e., no structure factor effect), R_g values evaluated from the Guinier slope give

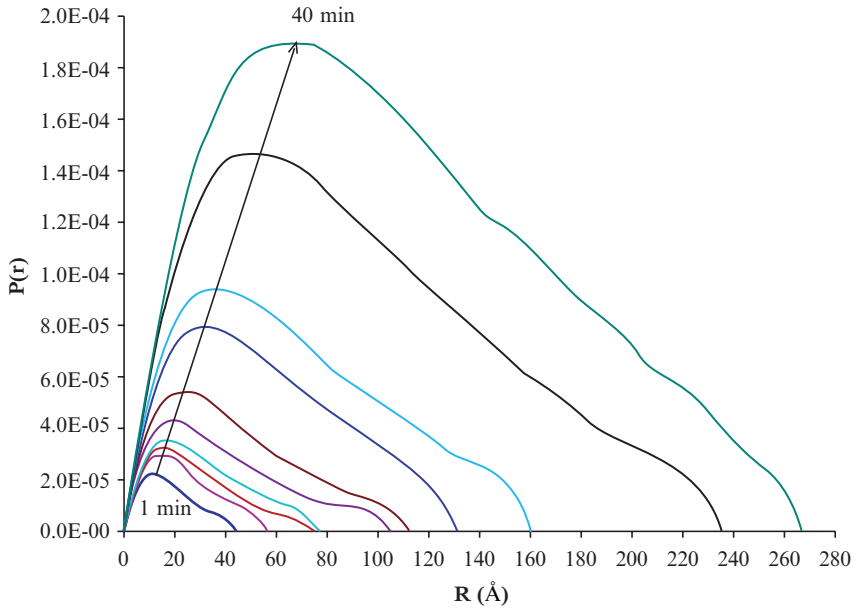

Fig. 7.24 Time resolved pair size distribution function plot for the formation of Cr-oxihydroxide colloids in aqueous suspensions determined from scattering patterns from 1 to 40 min (Shaw, Benning et al., unpublished data)

only a rough approximation of the particle sizes. A more accurate way to derive R_g is to use the full scattering pattern and derive the PDF and this can be done for example using a program like GNOM (Svergun, 1992).

In order to illustrate the usefulness of PDF in dilute solution SAXS, we use an example from an experiment that followed the formation of CrOOH colloids in alkaline solutions (Henderson, 2002; S. Shaw, personal communication). The PDF's extracted from the individual scattering patterns from a time resolved *in situ* solution SAXS experiment are plotted in Fig. 7.24. The fact that already in the first pattern (1 min) the PDF curve is skewed to the left indicates that the forming CrOOH particles are slightly elongated with an average particle radius of ~ 13 Å. With increasing time the overall shape of the PDF and thus the elongated shape of the particles does not change but the average radius increases and reaches ~ 80 Å at 40 min.

Using such PDF analyses it is subsequently also possible to confirm the real particle shape by using modeling approaches (e.g., Svergun, 1999). This can be done for example by using the program DAMMIN (Svergun, 1999) that was developed for biological macromolecule shape determination from dilute SAXS data. The DAMMIN approach uses the PDF's from each pattern and calculates $I(q)$ by fitting experimental data and finding a dummy atom model – DAM-configuration corresponding to the minimal value of an energy function. This process is iterative and follows the minimization of the discrepancies between experimental data and DAM-evaluated scattering curves via simulated annealing. The resulting DAMMIN

shapes from each PDF can thus provide corroborating information on shapes at each step in the reaction. The combination of these approaches allows ultimately the evaluation of nucleation and growth reaction kinetics that are clearly linked to size and shape of particles in aqueous solution. A similar study by Davidson et al. (2005) followed the formation of schwertmannite in aqueous solution in a pure system and in the arsenic-contaminated system. Their PDF and DAMMIN evaluations showed that arsenate affects the shape of schwertmannite particles and it causes an increase in asymmetry of the $p(r)$, reflecting a more elongate particle in the presence of arsenate. These results fit well with the EXAFS analyses of Waychunas et al. (1995) who showed that arsenate does not get incorporated into the schwertmannite tunnel structure but that it binds via an inner sphere process to the surface of schwertmannite crystallites.

In the second example we discuss the work of Gilbert et al. (2004) who have used SAXS/WAXS analyses combined with XAS and molecular dynamics (MD) simulations to study the solid-state transformation in 3 nm ZnS nanoparticle properties during hydration (Fig. 7.25). They have observed a large increase in crystallinity and particle radius upon water addition and the analyses of their WAXS derived PDF showed a split and peak sharpening in the structure factor $S(q)$ [related to the PDF or $G(r)$ via Eq. (7.45) upon water addition]. This indicates a reduction in structural disorder within the original ZnS nanoparticles and the appearance of new peaks also supports an increase in crystallinity. Figure 7.25 also shows the good agreement between the modeled patterns (MD simulations) and the experimental data and from previous work of the same group (Zhang et al., 2003) it was known that the particles are fairly monodispersed and spherical in shape. However, the PDF was not fully Gaussian in shape and this may indicate that asymmetry in the bond length distribution could also have contributed to the observed increase in radius. When they compared the WAXS analyses with the XAS data however, the agreement was not so good although the WAXS and molecular dynamic modeling fitted better (see also examples below in the XAS section and Beale et al., 2006).

In the last example the high temperature nucleation, growth and crystallization (devitrification) of cordierite glass is discussed (Bras et al., 2005). Cordierite glass ceramics have many special characteristics (e.g., low thermal expansion, high chemical resistance), which makes them desirable as specialized materials for example in exhaust catalysts or tunable laser. Bras et al. (2005) followed the devitrification process via a combination of *in situ* SAXS, WAXS and *ex situ* EXAFS (see next section) measurements. Their time resolved SAXS and WAXS results (Fig. 7.26a and 7.26b) clearly show the increase in I(0) as a function of time with the associated formation of Bragg peaks in the WAXS for two phase (spinel – sp, and quartz, sq). For example, the combined SAXS and WAXS data from an experiments at 970° C (Fig. 7.26c) shows the changes in integrated peak intensity for the two main crystalline phases (Fig. 7.26c, panel (i)), the growth in R_g and I(0) with time (Fig. 7.26c, panel (ii)), the evolution of the Porod constants and slope (Fig. 7.26c, panel (iii)), and finally the development of the invariant, Q (Fig. 7.26c, panel (iv)). This clearly points towards the fact that the devitrification

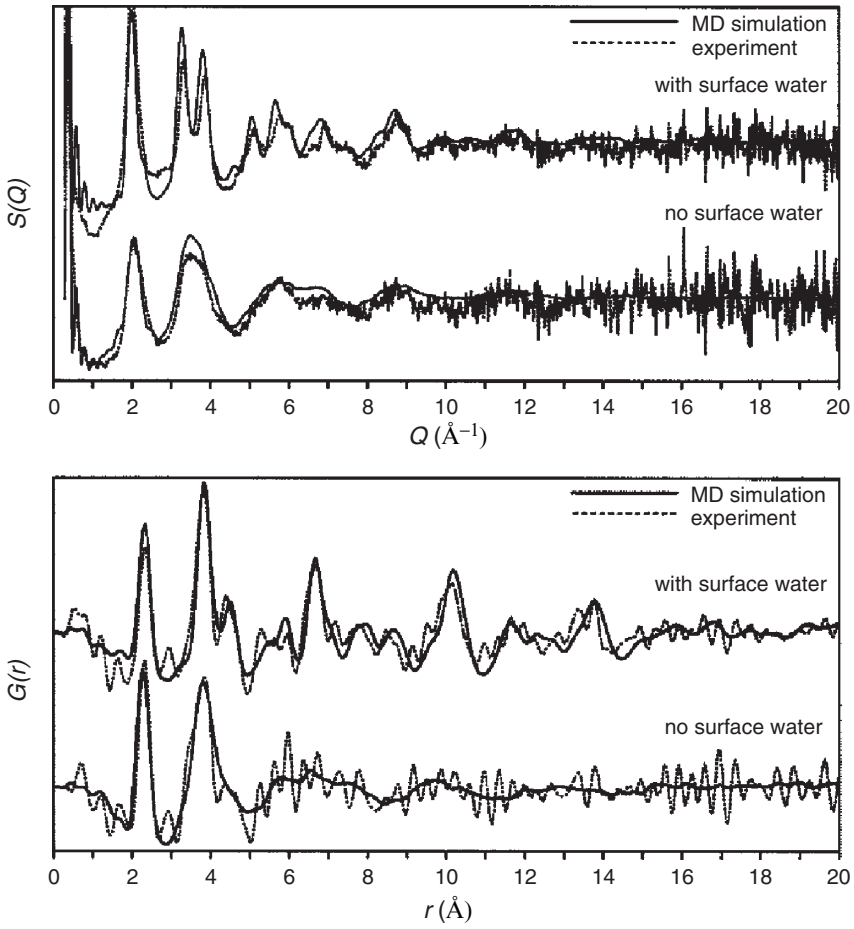

Fig. 7.25 WAXS PDF analyses for non-dilute solutions and structure factor S(q) effect relationships for ZnS particles (Reused from *Journal of Chemical Physics*, Volume 120, Gilbert, B., Huang, F., Zhang, H., Ren, Y., Haskel, D., Lang, J. C., Srajer, G., Jürgenssen, A., Waychunas, G., and Banfield, J. F., Analysis and simulation of a nanoparticle structures observed in a surface-driven transition, pp. 11785–11795; Copyright (2004), with permission from American Institute of Physics)

process produced monodispersed spherical crystallites of alumino-chromate spinel composition that grew from Cr nucleating sites. Interestingly the final spherical particle size reached $210 \pm 20\,\text{Å}(R_g = 180 \pm 20\,\text{Å})$, and the surface of the crystallites changed during the process from rough to smooth. In addition, the linear relationship between R_g^2 and time indicated clearly that the growth of the particles was governed by a diffusion-limited process that was solely dependent on the availability of Cr in the starting glass (Fig. 7.26d).

Lastly, from the EXAFS data they determined that the composition of the resulting spinel phase is directly correlated to the Cr content of the starting glass and

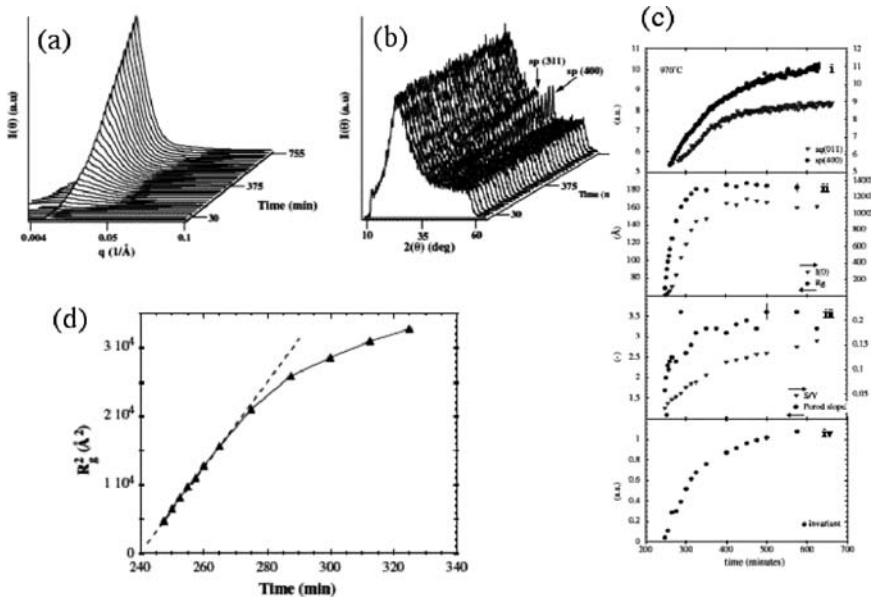

Fig. 7.26 Three-dimensional plots of the development of the scattering profiles in the SAXS (**a**) and WAXS (**b**) regions during isothermal crystallization at 920° C; (**c**) Parameters derived from the isothermal crystallization of cordierite glasses at 970° C; top panel (i) integrated peak intensity from representative peaks of spinel (sp) and quartz (sq); (ii) size development of R_g and I(0); (iii) evolution of the constants derived from the Porod equation; (iv) development of the invariant Q. (**d**) The development of R_g^2 versus time for the sample isothermally crystallized at 970 C. (Reprinted from *Journal of Non-Crystalline Solids*, Volume 135, Bras, W., Greaves, G.N., Oversluizen, M., Clark, S.M. and Eeckhaut G., The development of monodispersed aluminochromate spinel nanoparticles in doped cordierite glass, studied by in situ x-ray small and wide angle scattering, and chromium x-ray spectroscopy, pp. 2178–2193; Copyright (2005), with permission from Elsevier)

from the WAXS data they quantified the crystallization kinetics for the devitrification. This work also nicely exemplifies the power of combined SAXS/WAXS/and EXAFS analyses in order to elucidate the nanostructure, crystallinity and local structure of particle formation processes, examples of which are described more in detail below.

7.5.3 XAS

X-ray absorption spectroscopy [XAS = XANES (near absorption edge structure) + EXAFS (extended fine structure)] is a powerful tool for the extraction of short range structural and chemical information in almost any physical system (gases, liquids, solids, glasses). The main advantages or XAS are its element selectivity, i.e., spectra are collected from specific x-ray absorption edges holding information on only those species and their surroundings, and insensitivity to long range

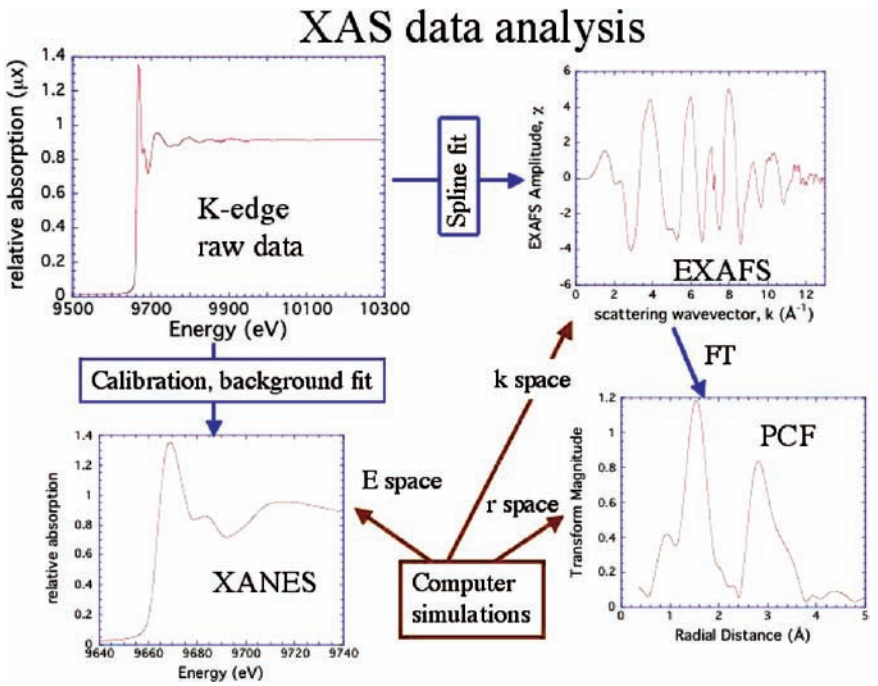

Fig. 7.27 XAS data and analysis scheme. Upper left: raw data with background subtracted to show the XANES (9660–9700 eV) and EXAFS (9700–10300 eV) regions at the Zn K-edge. Lower left: recalibrated XANES data ready for simulations by multiple scattering codes such as Feff. Upper right: extracted EXAFS region weighted by wavevector k^3. Ready for analysis by fitting of various shells of backscattering atoms about Zn absorber in k space. Lower right: Fourier transform of the EXAFS region showing the pair correlation function (PCF) which can be fitted by real-space analysis software. First peak is due to Zn–O shell and second peak to Zn–Zn and further Zn–O shells of neighbors. (After Waychunas, 2001)

order (and thus highly complementary to x-ray diffraction). Hence it is particularly useful for the study of complexation reactions from solution (Brown and Sturchio, 2002), the very beginnings of precipitation (Waychunas, 2001), and studies of localized reactive complexes in biochemical systems (Naqui et al., 1986; Kisker et al., 1997). It is also possible to employ XAS methods for extreme surface sensitivity by use of grazing-incidence synchrotron beams (Waychunas, 2002), for fast reaction processes using flow reactors (Grunwaldt et al., 2004), and at extreme conditions of pressure and temperature (Bassett et al., 2000; Badro et al., 1997).

7.5.3.1 Basic Concepts of EXAFS and XANES Analysis

Many thorough reviews of XAS analysis are available, e.g., Mottana, 2004; Galoisy, 2004; Brown et al., 1988; Stöhr, 1992, so here we limit our discussion to applications. Figure 7.27 shows a cartoon of EXAFS and XANES analyses schemes.

All elements have unique electron binding energies, so that their x-ray absorption edges occur at unique energies. Inner shell absorption involving K electrons give rise to K-edge spectra, while L-electrons give rise to L-edge spectra and so forth. EXAFS features, which occur in the x-ray spectrum above the absorption edge, arise because the x-ray energy is high enough to eject an electron from the atom as a photoelectric wave. This wave can then scatter off of adjacent atoms, with the waves returning to the absorbing atom creating interference and slightly modulating the absorption amplitude. This effect appears as an oscillating function in the edge from a few eV above the edge energy up to 1,500 eV above the edge. Each interatomic distance between the absorber atom and its neighbors produces a different frequency of these oscillations, and an amplitude depending on the number of scatterers and their atomic numbers. There is additionally a phase shift in the scattered waves, which is dependent on the atomic number of both absorber and backscatterer. Hence above the edge a complex oscillatory pattern is seen which records the first several shells of atoms about a particular absorber, i.e., the one whose edge is being investigated. For more distant shells of atoms the spacing becomes progressively closer and the individual frequencies tend to cancel one another out. Hence EXAFS analysis is mainly limited to the first few shells of atoms about an absorber. Analysis of the EXAFS is done by extracting the oscillations and taking a Fourier transform, thus generating a pair correlation function (PCF) with the absorbing atom as the center (origin). As this analysis can be done potentially for any element in a structure, one can extract independent structural information, even if the elements reside in the same nominal structural sites.

A related method, DAFS, or diffraction anomalous fine structure, can separate the EXAFS as a function of crystallographic site as well as by elemental identity (Pickering et al., 1993). For exacting analysis the EXAFS and PCF functions can be calculated and compared with the raw data or Fourier transform, respectively, or a least squares fitting procedure can be used. The output of this analysis is the number and distances of the first several shells of atoms and their disorder. By disorder we mean the damping of the EXAFS oscillations with increasing energy. The damping is caused by static disorder and vibrational disorder. Static disorder means that the shell of atoms has many interatomic distances, and thus contributes a range of frequencies to that shell's EXAFS. Vibrational disorder similarly contributes a range of interatomic distances with time. The more frequencies present in the EXAFS spectrum, especially within a given shell, the more the overall EXAFS will be damped out with increasing energy above the edge.

The XANES part of the XAS spectrum occurs both below and above the absorption edge, and is due to two processes. The lower energy "pre-edge" XANES are connected with excitation of electrons into bound states residing on the atom or on a localized molecular orbital. As these states are lower in energy than complete ejection of the electron from the atom, the features reside below the edge. Other XANES features occur on the edge and into the EXAFS region, and are due to multiple scattering effects, i.e., the ejected photoelectric wave makes at least two "bounces" off nearby atoms before returning to the absorber and creating interference. The interatomic paths for XANES are thus longer than those for single scattering, and

thus at higher frequencies. The resulting oscillations tend to damp out more quickly than the EXAFS, and as such are seen mainly near the absorption edge. XANES bound state transitions are very sensitive to the final state molecular orbital constitution, and thus can exhibit amplitude and energy changes indicative of valence, coordination and bonding changes. XANES analysis is often done empirically by comparison with model compounds. This is due to the complexity of accurately calculating the XANES spectra, compared to EXAFS calculations. However in recent years XANES calculations have improved (Waychunas, 2003) and many edges can be calculated, though direct fitting of spectra may still be a distant goal.

7.5.3.2 EXAFS Analysis of Nucleation and Precipitation

EXAFS is an excellent technique for the study of the initiation of nucleation and precipitation reactions, as it is in this regime that average short range structure about a given atom species in the sample may change the most. One recent illustrative study is that of Thoral et al. (2005) where solutions of Fe^{2+} and As^{3+} are oxidized and the precipitates examined by XAS. The precipitates change in character with time as oxidation proceeds, as shown in Figs. 7.28 and 7.29. Figure 7.28 shows the evolution of the EXAFS Fe K edge PCF for both the pure Fe^{2+} system and the mixed Fe^{2+}/As^{3+} system. In the pure Fe^{2+} system the PCF changes mainly due to the increase in the second shell coordination (and probable reduced disorder) as more aged precipitates are examined. The precipitates are presumably becoming larger and more ordered with time. In the mixed Fe^{2+}/As^{3+} system the initial state is very similar, but with time the second shell decreases in size. The analysis of this second shell requires several contributions, but in essence the attachment of $FeO_6 - AsO_3$

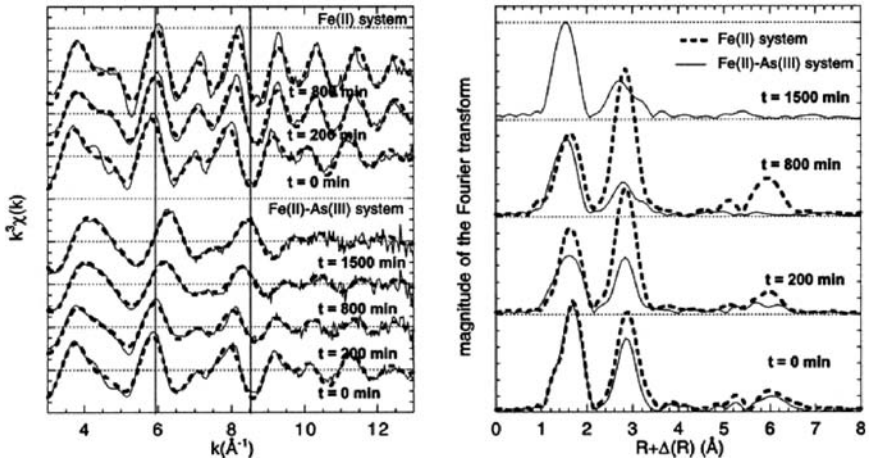

Fig. 7.28 Example of Fe K-edge EXAFS analysis of the oxidation of Fe^{2+} and Fe^{2+}–As^{3+} solutions as a function of time. Left: fitted EXAFS (dashed line-fit). Right: corresponding PCFs (dashed line-Fe^{2+} system). See text for further explanation. (After Thoral et al., 2005)

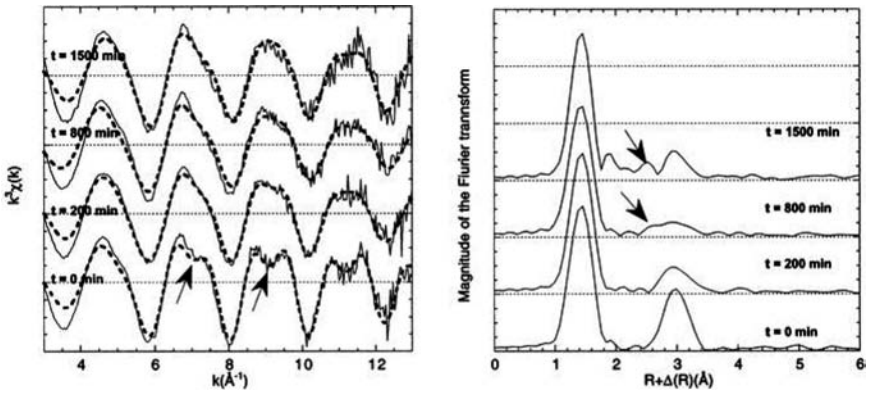

Fig. 7.29 The Fe^{2+}–As^{3+} system studied by EXAFS analysis on the As K-edge. Left: fitted EXAFS. The arrows indicate the higher frequency EXAFS oscillation due to Fe-As neighbors. Right: PCFs. Arrows indicate the appearance of a second As–Fe peak with continued oxidation due to formation of Fe^{3+}–As^{3+} neighbors. (After Thoral et al., 2005)

polyhedra must retard the development of the more organized Fe oxide. In Fig. 7.29 the analogous As K-edge EXAFS and PCFs are shown. Initially the arsenite attaches to small Fe oxide units yielding a well-defined $Fe^{2+} - As^{3+}$ second shell peak. With time this second shell broadens and splits into two contributions, the second being due to $Fe^{3+} - As^{3+}$ attachments. Hence several competing reactions are occurring. Although the authors do not go further to develop a quantitative model for the reaction kinetics, it is clear that such types of oxidative reactions can be characterized using XAS, while x-ray diffraction methods would have yielded little due to the poor crystallinity of the precipitates.

A different example with catalytic materials is shown by the work of Ressler et al. (2002). In this study the reversible change of MoO_2 into MoO_3 was detailed by a fast XAS experiment (60 s resolution) where data could be collected on a continuously reacting solid sample. Figure 7.30 shows a plot of the time evolution of the XANES spectra over periods of oxidation, reduction and oxidation, as well as a plot of the phase proportions for another reaction series. If done at varied temperatures a series of oxidation reaction curves are produced (Fig. 7.31) which can be analyzed over their linear early regions with an Arrhenius plot to yield activation energies (Fig. 7.32) for the initial process. This is seen to clearly change at about 700 K to a much lower value, and it is suggested that the reaction changes from an oxygen-diffusion controlled reaction at lower temperatures into a nucleation and growth regime. Activation energies can also be derived from the longer duration somewhat non-linear parts of the oxidation curves, and indicate higher activation energies.

Another example is EXAFS analysis in the identification and characterization of phase transitions at high pressures. Badro et al. (1997) examined changes in the quartz-structure compound $\alpha - GaAsO_4$ at room temperature with pressures up to 30 Gpa. The crucial information derived from EXAFS analysis is the individual

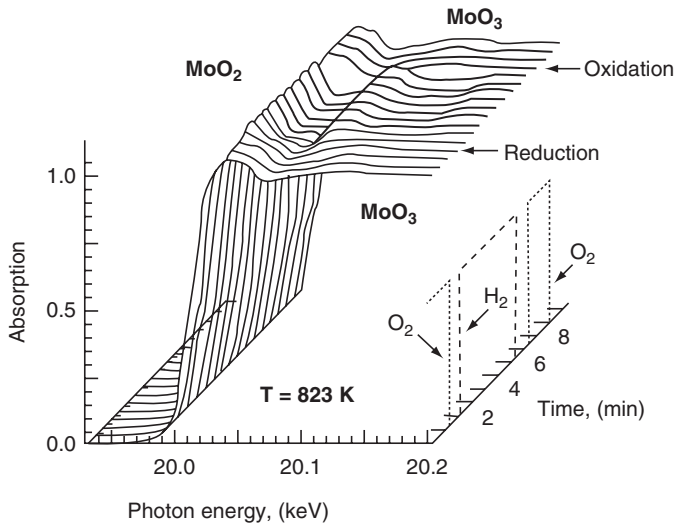

Fig. 7.30 Time-resolved Mo K-edge EXAFS measurements of redox changes in MoO_x catalysts over a programmed reaction series. From these data it is possible to extract the amount of new phase created as a function of time, as well as short range order and average valence. (After Ressler et al., 2002)

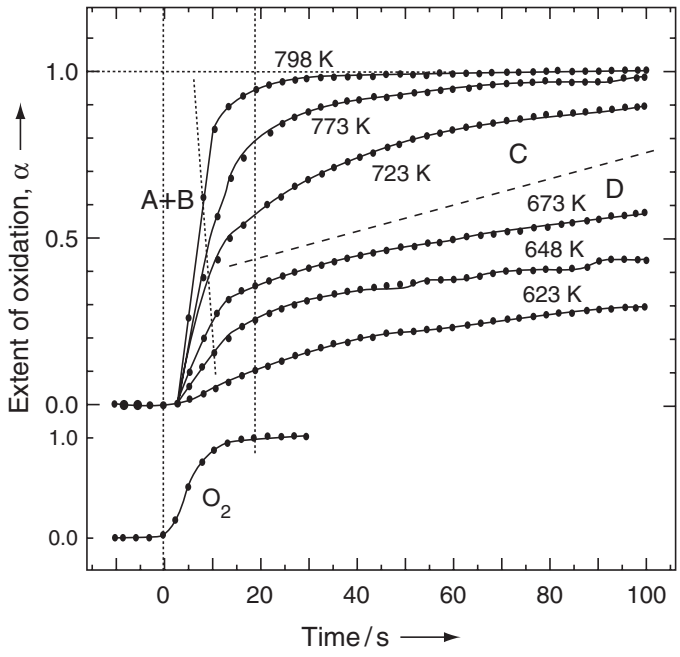

Fig. 7.31 Extracted oxidation change from MoO_2 to MoO_3 at varying temperature from data of the type shown in figure 31. In region A + B there is a linear increase with time, while region C shows an exponential dependence and region D a power-law dependence. (After Ressler et al., 2002)

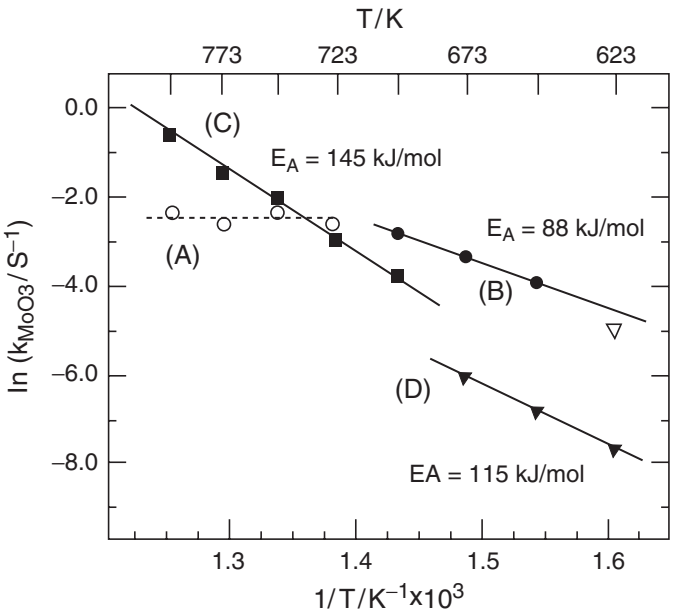

Fig. 7.32 Arrhenius plot for the data in the various regions of Fig. 7.32 plus that from two other temperatures (748 and 698 K) with corresponding activation energies. (After Ressler et al., 2002)

Ga–O and As–O interatomic distances, which decrease as pressure is increased and then increase dramatically as a coordination change occurs (Fig. 7.33). Interestingly, two separate transformation regimes are observed, the lower pressure one coinciding with all of the Ga changing from tetrahedral to octahedral coordination over the range 8–13 GPa, with the As partially converted to octahedral coordination. Above 13 GPa the As converts completely to sixfold coordination. These two regimes have consequences for the quench product. Samples quenched from the lower pressure regime return to the all tetrahedral coordination starting structure, but quenching from the higher pressure regime results in a partly or entirely amorphous material, i.e., the polyhedral deformations and rotations induce a glassy state which cannot readily recrystallize. XRD studies support these conclusions.

A final example is the EXAFS analysis of surface precipitates. The study of Waychunas et al. (1999) examined precipitates of Fe oxides formed on quartz single crystal substrates from acidic aqueous solution. The precipitates were nanosized, and of such a low density that most analysis methods would have not allowed characterization. However, by doing grazing-incidence EXAFS (GIXAFS), both the structure and the relationship to the quartz surface could be determined. A powerful advantage here is that a polarized experiment can be done (Fig. 7.34), where we can orient the sample with the electric vector of the synchrotron x-ray beam pointing either along the surface or normal to the surface. This effectively determines the "probe" direction of the EXAFS experiment, and identifies preferred

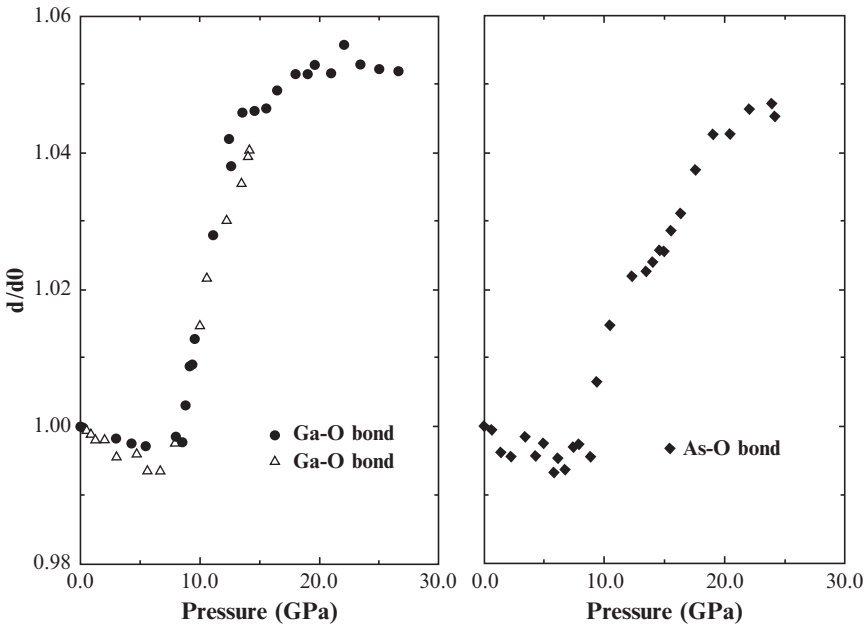

Fig. 7.33 Relative bond length changes derived from EXAFS analysis for Ga–O and As–O in berlinite as a function of increasing pressure at room temperature. A well-defined phase transformation is initiated at about 9 GPa with lengthening of the Ga–O bond due to coordination change from 4 to 6. The As–O bond length goes through a more complex transformation with a break at about 12.5 GPa at which point most of the Ga has changed coordination but the As is in both 4 and 6 coordination. Further pressure shifts all As to sixfold coordination at about 21 GPa. (After Badro et al., 1997)

orientation or epitaxial relationships should they be present. The Fe oxide precipitates in this case show very different PCFs depending on polarization direction. In particular, the short Fe–Fe distance characteristic of the shared $FeO_6 - FeO_6$ polyhedral faces along the c-axis in hematite are seen in the normal polarization PCF, but are missing from the in-plane PCF. This means that the precipitates are hematite-like rather than a FeOOH-type phase, and have their c-axes along the sample surface normal. Further analysis also revealed the precipitate minimum mean size of about 1 nm. Using this methodology it would be possible to observe nanoscale precipitation and aggregation processes at all types of mineral interfaces.

7.5.3.3 Complementarity of EXAFS, WAXS, and SAXS

EXAFS and wide-angle x-ray scattering (WAXS or "powder diffraction") are uniquely complementary as they yield short-range and long-range structure,

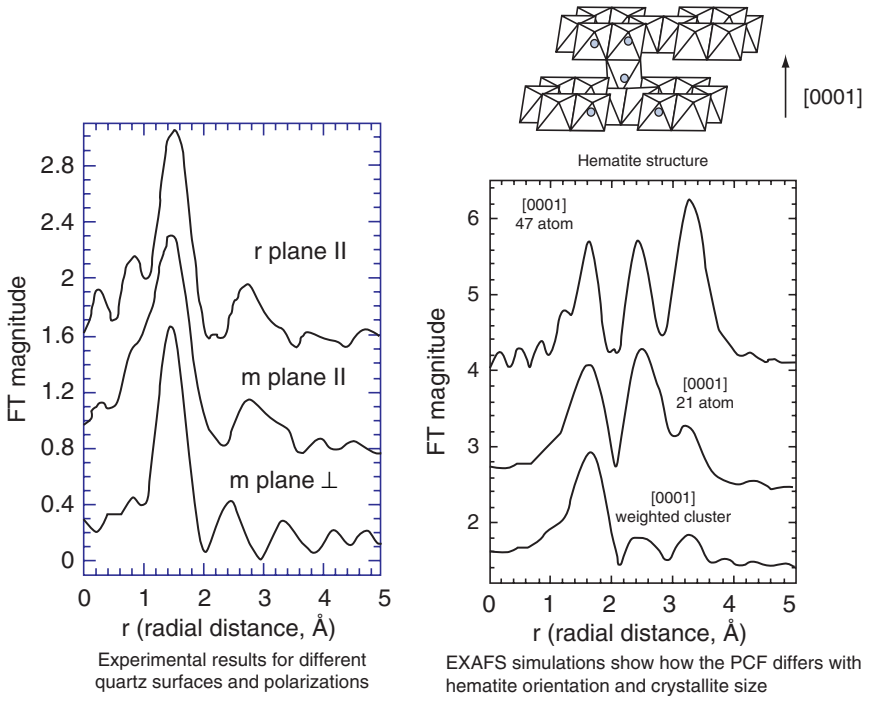

Fig. 7.34 Polarized (grazing-incidence) EXAFS analysis of hematite-like precipitates on quartz surfaces. The PCFs show very similar form when the electric vector (and thus EXAFS probe direction) is in the plane of the quartz whether it is the r- or m-plane surface. But the perpendicular electric vector orientation for the r-plane surface shows quite different structure. These differences are due to varied near neighbor Fe–Fe distances and numbers as a function of direction in hematite single crystals and suggest highly oriented nanocrystallites on the surface. The left side of the figure shows simulations of the r-plane perpendicular electric vector EXAFS for different cluster sizes with best agreement for roughly 1 nm diameters weighted for appropriate reduced Fe–Fe coordinations at the surface of the clusters. (After Waychunas, 2002)

respectively. Hence EXAFS can be used to characterize materials whose XRD pattern is poor, such as fine particles and nanoparticles, glasses, and even liquids or melts. On the other hand, WAXS measurements can yield quantitative measurement of the amount of product formed in a reaction as long as this phase is well crystallized. Use of both techniques together can then potentially allow characterization of reaction products from nucleation though crystal growth and coarsening. Small angle scattering (SAXS) yields no direct atomic structural information but can detect precipitate growth or aggregation and follow these processes quantitatively. Particularly in the case of aggregation, where the WAXS pattern may change negligibly, SAXS and EXAFS are highly complementary. A new technique, grazing-incidence SAXS (GISAXS) is now becoming available for the study of growth and aggregation processes and kinetics at surfaces and interfaces, and

should be extremely useful for heterogeneous nucleation and surface-mitigated processes.

7.6 Synthesis and the Future

Many of the processes and molecular scale techniques described in this chapter complement the knowledge illustrated in several other chapters in this book that relate various theoretical concepts and models (e.g., Chap. 2) with kinetic rate laws (e.g., Chaps. 1 and 11) and mechanistic concepts describing both dissolution (e.g., Chap. 5) or precipitation pathways (Chap. 3), both at the macro as well as molecular scales. In this chapter, we have summarized the theoretical basis and introduced some specific experimental approaches and examples that underpin and explain our current knowledge base related to processes and mechanisms that govern the reactions that lead to the nucleation, growth and aggregation of mineral phases in and from solution.

It is important to note the differences – and to distinguish – between nucleation and growth reactions that occur in solutions versus those that occur at surfaces or interfaces. However, regardless of the process, their quantification will always rely on rigorous experimental and molecular modeling approaches, which can only be obtained in combination with each other and only this way will it further advance our knowledge in this field. We have shown that several direct and indirect methods can help acquire and quantify the critical parameters needed to model such processes. In certain cases we are now able to determine very accurately the size and shapes of critical nuclei, and thus derive energetic information of nucleation and growth; we can extract information about pair size distribution of nuclei in solutions or in the bulk aggregates; we can image these processes using high-resolution microscopic approaches and we are able to determine very accurately the bonding environment in dispersed or aggregated samples or on surfaces. Yet, despite all this, it is crucial to be aware of possible pitfalls as well as of the limitations of each of these approaches. We hope to have made it clear that only a complementary, multi-dimensional and intra-disciplinary approach can further our knowledge of the kinetics in such systems and that there is no single pathway that we can suggest to the reader to follow if they want to study such complex processes.

For example, with aqueous interfaces many techniques for characterizing the system are limited by the need to specially prepare or alter the sample and remove all moisture (TEM, SEM, STM), which can dramatically alter the system under study (although developments in cryo-imaging can help). Similarly, atomic force microscopy (AFM) cannot achieve the needed resolution under water in a reacting system (although they can provide unique data that are not achievable otherwise). Thus, such imaging techniques must always be complemented by atomic-scale spectroscopy, or other methods, if atomistic/molecular processes are to be considered.

In the last decade or so, more and more methods that can follow and quantify processes *in situ* and in a *time resolved* mode (and in the case of live materials also *in vivo*) have been tested and developed. Ultimately, only such well designed and painstakingly tested approaches will help us quantify reactions and mechanisms governing processes occurring from the atomistic all the way to the bulk scale and combine this with molecular modeling.

Despite all these advances, it is a bit disappointing that in most cases we cannot readily apply our most sophisticated theoretical models to the physical systems under study. This is due, on the one hand, to the inability to measure particular parameters for very small nuclei such as interaction energies at interfaces and surfaces, accurate densities and water contents, and molecular geometries, and on the other hand, to failures of elegant theory to model actual physical processes acceptably (suggesting more development is still required). However, we do expect that as computer cluster power increases and is more readily available, it will be possible to get better estimates for the at present still unmeasureable parameters via *ab initio* simulations. We hope thus to gradually see a convergence between the more and more complex idealized theoretical models and the *in situ* and *realtime* derived quantitative data from experiments and thus to provide crucial parameters for a series of relevant applications.

Another consequence of faster and more accurate computer simulations is the ability to test theoretical models involving large numbers of atoms that approach the size of critical nuclei. This is especially important for cases where nuclei are unlikely ever to be observed due to their low number density and fleeting existence, and for systems involving mineral–water interfaces where water structure and the complexities of the electrical double layer (EDL) must also be considered. We thus look toward a future with more options for detailed theoretical development, better testing of theory applied to physical systems, and ultimately a much better description of the rate and rate dependences of precipitation and growth processes.

Acknowledgements

First and foremost the authors wish to thank the editors for their infinite patience with our continual delays as well as for supporting and encouraging us to finish this chapter. LGB acknowledges financial support for this work from the UK Natural Environmental Research Council (grant no: NER/A/S/2002/00761, and NE/C004566/1) and The Leverhulme Trust grant (Ref. #F/00122/F). GAW acknowledges support from the Department of Energy, Office of Biological and Environmental Research to LBNL, connected with the Center for Environmental Kinetics Analysis (an NSF-funded Environmental Molecular Sciences Institute at Pennsylvania State University). Comments from colleagues and students as well as two anonymous reviewers have tremendously helped shape this chapter.

Glossary of Symbols

a	chemical activity
a_c	concentration
A	function of total particle mass and number
A_i	surface area of an i-sized cluster
B_{ij}	size dependent diffusion coefficient for colloids
c	composition
c_i	number of clusters of size i
C	mean probability of adatom finding adjacent surface adatom
C_n	occupation of nth layer by adatoms
$D_{i->j}$	probability operator (exchange of i to j)
D^+, D^-	probability operators (growth, dissolution, respectively)
D_f	fractal dimension
$D(i)$	probability operator for cluster of size i (continuous distribution i)
E_b	energy barrier to colloid collision
f_c	local free energy per unit volume
$f_{n:m}$	fraction of surface atoms in layer n with m neighbors
F	free energy functional for Cahn-Hilliard equation
Δg	free energy change per unit volume of nucleus
G_d	free energy of diffusion across the nucleus matrix interface
$G(r)$	radial pair distribution function
ΔG	difference in free energy
ΔG^*	free energy change for critical nucleus formation
H	intramolecular interaction parameter for gradient energy in Cahn-Hilliard DFT
I	nucleation rate
$I(q)$	x-ray scattering intensity
$I(0)$	x-ray scattering intensity at $q = 0$
J_0	total cluster flux at steady state
J_i	flux of clusters growing through size i
k	first order rate constant
k^+, k^-	deposition, evaporation rates, respectively, for atom additions to growth surface
k_B	Boltzmann constant
K_B	function of diffusive Brownian motion
K_{da}	aggregation rate of particles partially destabilized during aggregation
K_1, K_2	thermal background and Porod constant related to scattering intensity $I(q)$
$K_{i,j}$	rate constant for coalescence or aggregation of particles i and j
L	atom-atom binding force
L_{CSD}	size interval for growing crystals in CSD analysis
L_c	cylinder length
m	number of adjacent layer nieghbors
M	total mass of clusters
n	time exponent related to mechanisms in Avrami equation
$n(i)$	equilibrium distribution function of all clusters in a system
$n(L_{CSD})$	number of growing crystals of a given size interval, L_{CSD}
N	number of critical nuclei or number of scatterers per volume of sample
N	total number of clusters or particles
N_A	Avogardo's number
N_T	total number of atoms in a system
N_i	site density for heterogeneous nucleation
N_V	nucleation sites/unit volume
$p(r)$	scattering length or pair distribution function
P	probability of a collision between colloids

$P(q)$	x-ray scattering form factor
P_{ij}	matrix effects related to aggregation rate $K_{i,j}$
q	x-ray scattering wave vector
Q	Integral of x-ray scattering intensity over q space; also termed Porod invariant
r	critical radius
R_U	universal gas constant
R	radius
R_{SOS}	growth rate for surface in SOS model
$\overline{R}$	mean growth rate
R_g	radius of gyration
R_s	radius of sphere
R_c	radius of cylinder
R_f	size of a fractal construct
s	number of atoms in matrix
S_R	solute supersaturation ratio
S_{eq}	bulk solubility
S	surface area
$S(q)$	x-ray scattering structure factor
t	time
T	absolute temperature
U	growth rate of individual grains in Avrami model
V	volume
V_p	volume of an individual scattering element
W	stability ratio for interactions between primary particles
Z	Zeldovich factor
α	factor related to slope of scattering profile in Porod region
α_A	volume fraction transformed in Avrami model
α_t	number of atoms of molecules leaving a cluster per unit time and surface area
β	thermal energy scaling factor, equal to $1/k_BT$
β_t	number of atoms of molecules joining a cluster per unit time and surface area
ε	reduced probability parameter in Week's adtom growth model $= 2(1-2C)$
η	dynamic viscosity constant
θ	x-ray scattering angle or angle between a nucleus edge and the underlying surface
λ	x-ray wavelength
μ	$\chi\eta\varepsilon\mu\iota\chi\alpha\lambda\ \pi\omega\tau\varepsilon\nu\tau\iota\alpha\lambda$ <Comp: Please check the font type in all such instances.>
$\Delta\mu$	difference in chemical potential or driving force for nucleation
ν	molar volume of a nucleus
ν_δ	desorption rate for an isolated surface atom
ν_φ	frequency of diffusion jumps or lattice vibrations
ρ	density
ρ_π	density of a particle
ρ_o	density of the matrix
$\Delta\rho$	electron density difference
σ	free energy per unit area of surface
$\sigma_{\alpha,\beta}$	interfacial free energy (two phases)
$\sigma_{\alpha,\alpha}$	interfacial free energy (grain boundaries)
σ_{SL}	interfacial free energy (solid nucleus-liquid)
σ_{CL}	interfacial free energy (substrate-liquid)
σ_{CS}	interfacial free energy (substrate-solid nucleus)
τ	induction time
γ	the mean time required to deposit a monolayer of atoms
ζ	constant related to kernel shape in aggregation processes δ supersaturation
ϕ	fraction of one phase in the linked to the Porod invariant, Q
Φ	chemical potential change with atom desorption
χ	EXAFS function
ψ	time independent scaling factor

References

Avrami M. (1941) Kinetics of phase change III. *J. Chem. Phys.* **9**, 177–184.

Badro J., Gillet P., McMillan P. F., Polian A., and Itie J. -P. (1997) A combined XAS and XRD study of the high-pressure behavior of $GaAsO_4$ berlinite. *Europhys. Lett*. **40**, 533–538.

Bailey J. K. and Macartney M. L. (1992) Formation of colloidal silica particles from alkoxides. *Coll. Surf.* **63**(1–2), 151–161.

Ball R. C., Weitz D. A., Witten T. A., and Leyvraz F. (1987) Universal kinetics in reaction-limited aggregation. *Phys. Rev. Lett*. **58**, 274–277.

Bandura A. V., Sykes D., Shapovalov V., Truong T. N., and Kubicki J. D. (2004) Adsorption of water on the TiO_2 (rutile) [110] surface: A DFT study. *J. Phys. Chem. B* **108**, 7844–7853.

Banfield J. F. and Zhang H. (2001) Nanoparticles in the environment, In *Revs. in Miner. & Geochem.* **44**, 1–58. Mineralogical Society of America, Washington, DC.

Barabasi A. L. and Stanley H. E. (1995) *Fractal Concepts in Surface Growth*. Cambridge University Press, Cambridge.

Bassett W. A., Anderson A. J., Mayanovic R. A., and Chou I. M. (2000) Modified hydrothermal diamond anvil cells for XAFS analyses of elements with low energy absorption edges in aqueous solution at sub- and supercritical conditions. *Zeit. Krist.* **215**, 711–717.

Beale A. M., van der Eerden A. M. J., Jacques S. D. M., Leynaud O., O'Brien M. G., Meneau F., Nikitenko S., Bras W., and Weckhuysen, B. M. (2006) A combined SAXS/WAXS/XAFS setup capable of observing concurrent changes across the nano-to-micrometer size range in inorganic solid crystallization processes. *J. Am. Chem. Soc*. **128**, 12386–12387.

Becker R. and Doring W. (1935) Kinetische behandlung der keimbildung in übersättigten dampfen. *Ann. Phys*. **24**, 719–752 (in German).

Beelen T. P. M., Shi W., Morrison G. R., Van Garderen H. F., Browne M. T., Van Santen R. A., and Pantos E. (1997) Scanning transmission x-ray microscopy; a new method for the investigation of aggregation in silica. *J. Coll. Interface Sci.* **185**, 217–227.

Benning L. G., Phoenix V., Yee N., and Tobin M. J. (2004a) Molecular characterization of cyanobacterial cells (I): a synchrotron-based infrared study. *Geochim. Cosmochim. Acta* **68**, 743–757.

Benning L. G., Phoenix V. R., Yee N., and Konhauser K. O. (2004b) The dynamics of cyanobacterial silicification: an infrared micro-spectroscopic investigation. *Geochim. Cosmochim. Acta*. **68**, 729–741.

Benning L. G., Phoenix V., and Mountain B. W. (2005): Biosilicification: the role of cyanobacteria in silica sinter deposition. In Society of General Microbiology Symposium book *Micro-Organisms and Earth Systems – Advances in Geomicrobiology* (Eds. G. M. Gadd, K. T. Semple and H. M. Lappin-Scott), pp. 131–150.

Binks B. P. (Ed.) (1999) *Modern Characterization Methods of Surfactant Systems*. Surfactant Science Series, Vol. 83. Marcel Dekker, New York, Basel. 616 pp.

Boukari H., Lin J. S., and Harris M. T. (1997) Probing the dynamics of the silica nanostructure formation and growth by SAXS. *Chem. Mater.* **9**, 2376–2384.

Bras W., Derbyshire G. E., Ryan A. J., Mant G. R., Felton A., Lewis R. A., Hall C. J., and Greaves G. N. (1993) Simultaneous time resolved SAXS and WAXS experiments using synchrotron radiation. *Nucl. Instr. Methods Phys. Res. A* **326**, 587–591.

Bras W. and Ryan A. J. (1998) Sample environments and techniques combined with small angle x-ray scattering. *Adv. Coll. Interface Sci.* **75**, 1–43.

Bras W., Greaves G. N., Oversluizen M., Clark S. M., and Eeckhaut G. (2005) The development of monodispersed alumino-chromate spinel nanoparticles in doped cordierite glass, studied by in situ x-ray small and wide angle scattering, and chromium x-ray spectroscopy. *J. Non-Cryst. Solids* **351**, 2178–2193.

Brown G. E. and Sturchio N. C. (2002) An overview of synchrotron radiation applications to low temperature geochemistry and environmental science. *Rev. Mineral* **49**, 1–116.

Brown G. E., Calas G., Waychunas G. A., and Petiau J. (1988) X-Ray absorption spectroscopy: Applications in mineralogy and geochemistry. *Rev. Mineral*. **18**, 431–512.

Brydson R. (2001) *Electron energy loss spectroscopy*. Springer, New York, 160 pp.

Bunde A. and Havlin S. (1991) *Fractals and Disordered Systems.* Springer-Verlag, Berlin.

Burton W. K., Cabrera N., and Frank F. C. (1951) The growth of crystals and the equilibrium structure of their surfaces. *Phil. Trans. Royal Soc. London A* (*Math. Phys. Sci.*) **243**, 299–358.

Buseck P. R. (Ed.) (1992) *Minerals and Reactions at the Atomic Scale: Transmission Electron Microscopy*, Mineralogical Society of America, Washington, DC, 508 pp.

Butter K., Bomans P. H. H., Frederik P. M. Vroege G. J., and Philipse A. P. (2003) Direct observation of dipolar chains in iron ferrofluids by cryogenic electron microscopy. *Nat. Materials* **2**, 88–91.

Cahn J. W. and Hilliard J. E. (1958) Free energy of a non-uniform system. I. Interface free energy. *J. Chem. Phys*. **28**, 258–267.

Cahn J. W. (1962) Coherent fluctuations and nucleation in isotropic solids. *Acta Met*. **10**, 907–913.

Cahn J. W. (1966) The later stages of spinodal decomposition and the beginnings of particle coarsening. *Acta Met*. **14**, 1685–1692.

Carpenter M. A., Putnis A., Navrotsky A., and McConnell J. D. C. (1983) Enthalpy effects associated with Al, Si ordering in anhydrous Mg-cordierite. *Geochim. Cosmochim. Acta* **47**, 899–906.

Cashman K. V. and Marsh B. D. (1988) Crystal size distribution (CSD) in rocks and the kinetics and dynamics of crystallization II. Makaopuhi lava lake. *Contrib. Mineral Petrol* **99**, 292–305.

Castro M., Dominguez-Adame F., Sanchez A., and Rodriguez T. (1999) Model for crystallization kinetics: Deviations from Kolmogorov-Johnson-Mehl-Avrami kinetics. *Appl. Phys. Lett*. **75**, 2205–2207.

Chernov A. A. (1984) *Modern Crystallography III, Crystal Growth*. Springer, Berlin.

Clemm P. J. and Fisher J. C. (1955) The influence of grain boundaries on the nucleation of secondary phases. *Acta Met*. **3**,70–73.

Davidson L, Benning L. G., Shaw S., and Terrill N. J. (2005) The effect of arsenic on the nucleation and growth of schwertmannite: An in situ SAXS study. *Geochim. Cosmochim. Acta* **69/10S**, A773 (abstr).

DeFontaine D. (1975) Clustering effects in solid solutions. *Treatise on Solid State Chemistry*, Vol. 5 (Eds. N. B. Hannay), Plenum, New York, p. 129.

Eden M. (1961) In Proceedings of the *Fourth Berkeley Symposium on Mathematical Statistics and Probability*, Vol. IV (Ed. F. Neyman). University of California, Berkeley, p. 233.

Everett D. H. (1988) *Basic Principles of Colloid Science.* Royal Society of Chemistry Paperback*s*, London.

Farkas L. (1927) Keimbildungsgeschwindigkeit in übersättigten Dämpfen. *Z. Physik. Chem.* **125**, 236–242. (in German).

Fauchadour D., Pouget T., Lechaire J.-P., Rouleau L., and Normand L. (1999) Evaluation of cryotechniques for TEM observation of sols – application to boehmite sols used in catalysts forming. *Oil Gas Sci. Technol. Rev. IFP* **54**(4), 513–524.

Frank F. C. (1949) The influence of dislocations on crystal growth. *Disc. Farad. Soc*. **5**, 48.

Frederik P. M., Bomans P. H. H., Laeven P. F. J., and Nijpels F. J. T. (2002) Device for preparing specimens for a cryoelectron microscope. Netherlands Industrial Property Office (RO/NL).

Frenkel J. (1939) A general theory of heterophase fluctuations and pretransition phenomena. *J. Chem. Phys.* **7**, 538–547.

Frenkel J. (1955) *Kinetic Theory of Liquids*. Dover, New York.

Fultz B. and Howe J. M. (2002) *Transmission Electron Microscopy and Diffractometry of Materials*, 2nd edition; Series: Advanced Texts in Physics, Springer.

Galoisy L. (2004) X-ray absorption spectroscopy in geosciences: information from the EXAFS region. In *Spectroscopic Methods in Mineralogy* (Eds. A. Beran and E. Libowitzky), Eötvös University Press, Budapest.

Gedde U. W. (1995) *Polymer Physics*. Kluwer Academic Publishers, Dordrecht, The Netherlands.

Gilbert B., Huang F., Zhang H., Ren Y., Haskel D., Lang J. C., Srajer G., Jürgenssen A., Waychunas G., and Banfield J. F. (2004) Analysis and simulation of a nanoparticle structures observed in a surface-driven transition. *J. Chem. Phys.* **120**, 11785–11795.

Glatter O. (1992) Small-angle scattering. In: *International Tables for Crystallography* (Ed. A. J. C. Wilson), Kluwer Academic Publishers, Dordrecht, The Netherlands, pp. 89–112.

Glatter O. and Kratky O. (1982) *Small Angle X-ray Scattering.* Academic Press, London.

Goldstein J., Newbury D. E., Joy D. C., Lyman C. E., Echlin P., Lifshin E., Sawyer L. C., and Michael J. R. (2003) *Scanning Electron Microscopy and*

X-ray Microanalysis, 3rd edition. Kluwer Academic Plenum Publishers, New York, 586 pp.

Granasy L., Wang T., and James P. (1998) Kinetics of wollastonite nucleation in $CaO \cdot SiO_2$ glass. *J. Chem. Phys.* **108**, 7317–7326.

Green D. L., Lin J. S., Lam Y-F, Hu M. Z. -C., Schaefer D. W., and Harris M. T. (2003) Size, volume fraction, and nucleation of stober silica nanoparticles. *J. Coll. Interface Sci.* **266**, 346–358.

Grunwaldt J. D., Caravati M. Hannemann S. ,and Baiker A. (2004) X-ray absorption spectroscopy under reaction conditions: suitability of different reaction cells for combined catalyst characterization and time-resolved studies. *Phys. Chem. Chem. Phys.* **6**, 3037–3047.

Guinier A. (1939). La diffraction des rayons X aux tres petits angles: Application al'étude de phénomenes ultramicroscopiques. *Ann. Phys.* **12**, 161–237.

Guinier A and Fournet G. (1955) *Small-Angle Scattering of X-Rays*. Wiley, New York.

Hamad S. Cristol C., and Catlow R. A. (2002) Surface structures and crystal morphology of ZnS: Computational study. *J. Phys. Chem. B* **106**(42), 11002–11008.

Hartman P. and Perdok W. G. (1955) On the relations between structure and morphology of crystals. *Acta Cryst*. **8**, 49–52.

Hayat M. A. (2000) *Principles and Techniques of Electron Microscopy: Biological Applications*. Cambridge University Press, p. 543.

Heaney P. J., Vicenzi E. P., Gianuzzi L. P., and Livi K. J. T. (2001) Focused ion beam milling: a method of site-specific sample extraction for microanalysis of earth and planetary materials. *Am. Mineral.* **86**, 1094–1099

Henderson C. M. B. (2002) Earth and environmental sciences synchrotron research in the UK: Ongoing work and future prospects. *Geochem. News* **110**, 14–17.

Henry M. (2003) First-principles derivation of vacuum surface energies from crystal structures. *Solid State Sci.* **5**, 1201–1205.

Herring C. (1951) Some theorems on the free energies of crystal surfaces. *Phys. Rev.* **82**, 87–93.

Hochella M. F. Jr. (2002a) Nanoscience and technology: the next revolution in the earth sciences. *Earth Planet. Sci. Lett.* **203**, 593–605.

Hochella M. F. Jr. (2002b) There's plenty of roomat the bottom: nanoscience in geochemistry. *Geochim. Cosmochim. Acta* **66**, 735–743.

Hochella M. F., Jr. and Banfield J. F. (1995) Chemical weathering of silicates in nature: a microscopic perspective with theoretical considerations. In *Chemical Weathering Rates of Silicate Minerals* (Eds. A. F. White and S. L. Brantley). *Reviews in Mineralogy*, Vol. 31, Mineralogical Society of America, Washington DC, pp. 353–406.

Hof M., Hutterer R., and Fidler V. (Ed.) (2005) *Fluorescence Spectroscopy In Biology: Advanced Methods and Their Applications to Membranes, Proteins, DAN and cells*. Springer Series on Fluorescence. Series Editor O. S. Wolfbeis, Springer, 305 pp..

Huang F., Zhang H., and Banfield J. F. (2003) Two-stage crystal growth kinetics observed during hydrothermal coarsening of nanocrystalline ZnS. *Nano Lett.* **3**, 373–378.

Hulbert S. F. (1969) Models for solid-state reactions in powder compacts: A review. *J Br. Ceramic Soc.* **6**, 11–20.

Icopini G. A., Brantley S. L., and Heaney P. J. (2005) Kinetics of silica oligomerization and nanocolloid formation as a function of pH and ionic strength at 25° C. *Geochim. Cosmochim. Acta* **69/2**, 293–303.

Iler R. K. (1979) *The Colloid Chemistry of Silica and Silicates*, Cornell University press, Ithaca, NY.

Iler R. K. (1980) Isolation and characterization of particle nuclei during the polymerization of silicic acid to colloidal silica. *J. Coll. Interface Sci* **71**, 138–148.

Israelachvili J. (1992) *Intermolecular and Surface Forces.* Academic Press, London.

Jiang Z. and Ebner C. (1989) Dynamical Monte Carlo study of crystal growth in a solid-on-solid model. *Phys. Rev. B* **40**, 4833–4837.

Johnson W. A. and Mehl R. F. (1939) Reaction kinetics in processes of nucleation and growth. *Trans. Amer. Inst. Min. Engrs*. **135**, 416–458.

Katchalsky A. and Curran P. F. (1965) *Nonequilibrium Thermodynamics in Biophysics.* Harvard University Press, Cambridge, MA, 248 pp.

Kelton K. F. and Greer A. L. (1988) Test of classical nucleation theory in glasses. *Phys. Rev*. B **38**, 10089–10092.

Kirkpatrick R. J. (1981) Kinetics of crystallization in igneous rocks. In *Kinetics of Geochemical Processes. Reviews in Mineralogy* (Eds. A. C. Lasaga, R. J. Kirkpatrick (eds), Mineralogical Society of America Vol. 8, pp. 321–398.

Kisker C., Schindelin H., and Rees D. C. (1997) Molybdenum-cofactor-containing enzymes: Structure and mechanism. *Ann. Rev. Biochem*. **66**, 233–267.

Kubota N. and Mullin J. W. (1995) A kinetic model for crystal growth from aqueous solution in the presence of impurity. *J. Cryst. Growth* **152**, 203–208.

Lehn J-M. (2002) Toward self-organization and complex matter. *Science* **295**, 2400–2403.

Lifshitz I. M. and Slyozov V. V. (1961) The kinetics of precipitation from supersaturated solid solutions. *J. Phys. Chem. Solids* **19**, 35–50 (translated by R. D.Lowde).

Lin M. Y., Lindsay H. M., Weitz D. A., Ball R. C., Klein R., and Meakin P. (1990) Universal reaction-limited colloid aggregation. *Phys Rev. A* **41/4**, 2005–2020.

Liu X. Y., Maiwa K., and Tsukamoto K. (1997) Heterogeneous two-dimensional nucleation and growth kinetics. *J. Chem. Phys*. **106**, 1870–1879.

Makrides A. C., Turner M., and Slaughter J. (1980) Condensation of silica from supersaturated silicic acid solutions. *J Coll Interf. Sci*. **73**, 345–367.

Mandelbrot B. B. (1967) How long is the coast of Britain? Statistical self-similarity and fractional dimension. *Science* **156**, 636–638.

Mandelbrot B. B. (1975) *Les Objets Fractals: Form, Hasard et Dimension*. Flamarion, Paris.

Mandelbrot B. B. (1983) *The Fractal Geometry of Nature*. W. H. Freeman and Co., New York, 495 pp.

Mann U., Neisel J. D., Burchard W. G., Heinen V., and Welte D. H. (1994) Fluid–rock interfaces as revealed by cryo-scanning electron microscopy. *First Break*, **12**, 131–36.

Marasli N. and Hunt J. D. (1998) The use of measured values of surface energies to test heterogeneous nucleation theory. *J. Cryst. Growth* **191**, 558–562.

Marsh B. D. (1988) Crystal size distribution (CSD) in rocks and the kinetics and dynamics of crystallization. I. theory. *Contrib. Mineral. Petrol* **99**, 277–229.

Martin J. E. (1987) Slow aggregation of colloidal silica. *Phys. Rev. A* **36/7**, 3415–3426.

Martin J. E., Wikcoxon J. P., Schaefer D., and Odinek J. (1990) Fast aggregation of colloidal silica. *Phys. Rev. A* **41/8**, 4379–4391.

McLaren A. C. (1991) *Transmission Electron Microscopy of Minerals and Rocks*. Cambridge University Press, p. 399.

Meakin P. (1998) *Fractals, Scaling and Growth Far from Equilibrium*. Cambridge University Press, Cambridge.

Meakin P. (1983) Formation of fractal clusters and networks by irreversible diffusion-limited aggregation. *Phys. Rev. Lett*. **51**, 1119–1122.

Meakin P. and Family F. (1987) Structure and dynamics of reaction-limited aggregation. *Phys. Rev.* A **36**, 5498–5501.

Megens M., van Kats C. M., Bösecke P., and Vos W. L. (1997) In situ characterization of colloidal spheres by synchrotron small-angle x-ray scattering. *Langmuir* **13**, 6120–6129.

Meneau. F., Cristol S., Sankar S., Dolbnya I. P, Bras W., Catlow C. R. A., Thomas J. M., and Greaves G. N. (2003) *In situ* study of the formation of CdS nanoparticles by small-angle x-ray scattering. *J. Appl. Cryst.* **36**, 718–721.

Mottana A. (2004) X-ray absorption spectroscopy in mineralogy: Theory and experiment in the XANES region. In *Spectroscopic Methods in Mineralogy* (Eds. A. Beran and E. Libowitzky), Eötvös University Press, Budapest.

Naqui A., Chance B., and Cadenas E. (1986) Reactive oxygen intermediates in biochemistry. *Ann. Rev. Biochem*. **55**, 137–166.

Navrotsky A. (2004) Energetic clues to pathways to biomineralization: Precursors, clusters, and nanoparticles. *Proc. Natl. Acad. Sci. USA* **101**, 12096–12101.

Navrotsky A. (1999) High temperature reaction calorimetry applied to metastable and nanophase materials. *J. Therm. Anal. Cal*. **57**, 653–658.

Nielsen A. E. (1064) *The Kinetics of Precipitation*, McMillan, New York, p. 151.

Nicolis G. and Prigogine I. (1977) *Self-organization in non-equilibrium systems: From dissipative structures to order through fluctuations*. Wiley & Sons, New York.

Ohara M. and Reid P. C. (1973) *Modelling Crystal Growth Rates from Solution*. Prentice Hall, Englewood Cliffs, NJ.

Ostwald W. (1900) Über die vermeintliche isomerie des roten und gelben quecksilberoxyds und die oberflächenspannung fester körper. *Zeitschrift fur Physikalische Chemie, Stochiometrie und Verwandschaftslehre*, **34**, 495–503.

Oxtoby D. W. (1992) Homogeneous nucleation: Theory and experiment. *J. Phys. Condensed Matter* **4**, 7627–7650.

Palenik C. S., Utsunomiya S., Reich M., Kesler S. E., Wang L.,and Ewing R. C. (2004) "Invisible" gold revealed: Direct imaging of gold nanoparticles in a Carlin-type deposit. *Am. Mineral*. **89**, 1359–1366.

Pan Y., Brown A., Brydson R., Warley A., Li A., and Powell J. (2006) Electron beam damage studies of synthetic 6-line ferrihydrite and ferritin molecule cores within a human liver biopsy. *Micron* **37**(5), 403–411.

Paquette J. and Reeder R. J. (1995) Relationship between surface structure, growth mechanism, and trace element incorporation in calcite. *Geochim. Cosmochim. Acta* **59**, 735–749.

Penn R. L. and Banfield J. F. (1999) Morphology development and crystal growth in nanocrystalline aggregates under hydrothermal conditions: Insights from titania. *Geochem. Cosmochim. Acta* **63**, 1549–1557.

Perry C. C. (2003) Silicification: the processes by which organisms capture and mineralize silica. In *Biomineralization* (Eds. P. M. Dove, J. J. De Yoreo and S. Weiner) *Reviews in Mineralogy and Geochemistry*, **54**, 291–327.

Pfeifer P. and Obert M. (1989) *The Fractal Approach to Heterogeneous Chemistry: Surfaces, Colloids, Polymers*. (Ed. D. Avnir) Wiley, New York.

Pickering I. J., Sansone M., Marsch J., and George G. N. (1993) Diffraction anomalous fine structure: a new technique for probing local atomic environment. *J. Am. Chem. Soc.* **115**, 6302–6311.

Pina C. M., Putnis A., and Astilleros J. M. (2004) The growth mechanisms of solid solutions crystallizing from aqueous solutions. *Chem. Geol*. **204**, 145–161.

Pina C. M., Becker U., Risthaus P., Bosbach D., and Putnis A. (1998) Molecular-scale mechanisms of crystal growth in barite. *Nature* **395**, 483–486.

Pontoni D., Narayanan T., and Rennie A. R. (2002) Time-resolved SAXS study of nucleation and growth of silica colloids. *Langmuir* **18**, 56–59.

Price F. P. (1965) Some comments on the "Avrami" equation. *J. Appl. Phys*. **36**, 3014–3016.

Prigogine I. (1961) *Introduction to the Thermodynamics of Irreversible Processes*. Interscience, New York.

Raghavan V. and Cohen M. (1975) Solid State Phase Transformations. In *Treatise on Solid State Chemistry*, *Vol. 5. Changes of State* (Ed. N. B. Hannay). Plenum Press, New York, pp. 67–128.

Ranade M. R., Navrotsky A., Zhang H. Z., Banfield J. F., Elder S. H., Zaban A., Borse P. H., Kulkarni S. K., Doran G. S., and Whitfield H. J. (2002) *Proc. Natl. Acad. Sci. USA* **99**(Suppl. 2), 6476–6481.

Randolph A. D. and Larsen M. A. (1971) *Theory of Particulate Processes*. Academic Press, New York, 251 pp.

Ratsch C. and Venables J. A. (2003) Nucleation theory and the early stages of thin film growth. *J. Vac. Soc. Technol.* A **21**, S96–S109.

Ressler T., Wienold J., Jentoft R. E., Neisius T., and Gunter M. M. (2002) Kinetics of solid-state reactions in heterogeneous catalysis from time-resolved x-ray absorption spectroscopy. *Topics Catalysis* **18**, 46–52.

Rothbaum H. P. and Wilson R. D. (1977) Effect of temperature and concentration on the rate of polymerisation of silica in geothermal waters. In: *Geochemistry*

1977. **218**, 37–43. New Zealand Department of Scientific and Industrial Research Bulletin.

Samson I. M. and Walker R. T. (2000) Cryogenic Raman spectroscopic studies in the system NaCl–CaCl2–H2O and implications for low-temperature phase behavior in aqueous fluid inclusions. *Can. Mineral.* **38**, 35–43.

Sandkühler P., Lattuada P., Wu H., Sefcik J., and Morbidelli M. (2005) Further insights into the universality of colloidal aggregation. *Adv. Coll. Interface Sci.* **113**, 65–83.

Sarma K. R., Shlichta P. J., Wilcox W. R., and Lefever R. A. (1997) Epitaxy versus oriented heterogeneous nucleation of organic crystals on ionic substrates. *J. Cryst. Growth* **174**, 487–494.

Shaw S., Henderson C. M. B., and Komanschek B. U. (2000) Dehydration/recrystallization mechanisms, energetics, and kinetics of hydrated calcium silicate minerals: an in situ TGA/DSC and synchrotron radiation SAXS/WAXS study. *Chem. Geol.* **167**, 141–159.

Schenk O., Urai J. L., and Piazolo S. (2006) Structure of grain boundaries in wet, synthetic polycrystalline, statically recrystallizing halite – evidence from cryo-SEM observations. *Geofluids* **6**(1), 93–104.

Singh M. A., Harkless C. R., Nagler S. E., Shannon R. F., and Ghosh S. S. (1993) Time-resolved small angle x-ray scattering study of ordering kinetics in diblock styrene-butadiene. *Phys. Rev. B* **47**(14), 8425–8435.

Smoluchowski M. V. (1916) Drei vortrage uber diffusion, brownsche bewegung und koagulation von kolloidteilchen. *Physik. Zeit*. **17**, 557–585. (in German).

Steefel C. I. and Van Cappellen P. (1990) A new kinetic approach to modeling water-rock interaction: The role of nucleation, precursors, and Ostwald ripening. *Geochimica et Cosmochimica Acta* **54**, 2657–2677.

Stöber W., Fink A., and Bohn E. (1968) Controlled growth of monodisperse. Silica spheres in the micron size range *J. Coll. Interface Sci.* **26**, 62.

Stöhr J. (1992) *NEXAFS Spectroscopy*. Springer-Verlag, Berlin.

Sutherland D. N. (1967) Theoretical model of floc structure. *J. Coll. Interface Sci*. **25**(3), 373–380.

Svergun D. I. (1992) Determination of the regularization parameter in indirect-transform methods using perceptual criteria. *J. Appl. Cryst.* **25**, 495–503.

Svergun D. I. (1999) Restoring low resolution structure of biological macromolecules from solution scattering using simulated annealing. *Biophys. J.* **76**, 2879–2886.

Svergun D. I and Koch M. H. J. (2003) Small-angle scattering studies of biological macromolecules in solution. *Rep. Prog. Phys.* **66**, 1735–1782.

Talanquer V. and Oxtoby D. W. (1994) Dynamical density functional theory of gas-liquid nucleation. *J. Chem. Phys*. **100**, 5190–5200.

Thoral S., Rose J., Garnier J. M., Van Geen A., Refait P., Traverse A., Fonda E., Nahon, D., and Bottero J. Y. (2005) XAS Study of iron and arsenic speciation during Fe(II) oxidation in the presence of As(III). *Environ. Sci. Technol*. **39**, 9478–9485.

Tiller W. A. (1991) T*he Science of Crystallization: Microscopic Interfacial Phenomena*. Cambridge University Press, New York.

Tiller W. A. (1992) *The Science of Crystallization: Macroscopic Phenomena and Defect Generation*. Cambridge University Press, New York.

Tobler D. J., Benning L. G., and Shaw S. (2006) Nucleation and growth of silica nanoparticles: An *in-situ* SAXS and DLS study. *Geochim. Cosmochim. Acta* 70/18: A652, (abstr).

Tokuyama M., Kawasaki K., and Yoshihisa E. (1986) Kinetic equations for Ostwald ripening. *Physica A*, **134**(2), 323–338.

Toschev S. (1973) Homogeneous Nucleation. In *Crystal Growth: An Introduction* (Ed. P. Hartman). Elsevier, Amsterdam, pp. 1–49.

Trivedi R., Liu S., and Williams S. (2002) Interface pattern formation in nonlinear dissipative systems. *Nat. Mater.* **1**, 157–159.

Turnbull D. (1950) Formation of crystal nuclei in liquid metals. *J. Appl. Phys*. **21**, 1022–1028.

Turnbull D. (1956) Phase changes. *Solid State Phys.* **3**, 224–306.

Turnbull D. and Fisher J. C. (1949) Rate of nucleation in condensed systems. *J. Chem. Phys.* **17**, 71–73.

Utsunomiya S. and Ewing R. C. (2003) Application of high-angle annular dark field scanning transmission electron microscopy, scanning transmission electron microscopy-energy dispersive x-ray spectrometry, and energy-filtered transmission electron microscopy to the characterization of nanoparticles in the environment. *Environ. Sci. Technol*. **37**, 786–791.

van Enckevort W. J. P., van der Berg A. C. J., Kreuwel K. B. G., Derksen A. J., and Couto M. S. (1996) Impurity blocking of growth steps: Experiments and theory. *J. Cryst. Growth* **166**, 156–161.

Venables J. A., Spiller G. D. T., and Hanbücken M. (1984) Nucleation and growth of thin films. *Rep. Prog. Phys*. **47**, 399–459.

Vicsek T. and Family F. (1984) Dynamic scaling for aggregation of clusters. *Phys. Rev. Lett.* **52**, 1669–1672.

Vicsek T. (1992) *Fractal Growth Phenomena*. World Scientific, Singapore.

Vold M. J. (1959) Sediment volume and structure in dispersions of anisometric particles. *J. Phys. Chem*. **63**, 1608–1612.

Vold M. J. (1963) Computer simulation of floc formation in a colloidal suspension. *J. Coll. Sci*. **8**(7), 684–695.

Volmer M. (1939) *Kinetik der Phasenbildung*. Steinkopf Verlag, Leipzig-Dresden (in German).

Volmer M. and Weber A. (1925) Keimbildung in übersättigten gebilden. *Z. Phys. Chem.* **119**, 277–301. (in German).

Voorhees P. W. and Glicksman M. E., (1984) Solution to the multiparticle diffusion problem with applications to Ostwald ripening. I.theory. *Acta Meta*. **32**(11), 2001–2011.

Voorhees P. W. (1985) The theory of Ostwald ripening. *J. Statist. Phys.* **38**(1–2), 231–252.

Wagner C. (1961) Theorie der Alterung von Niderschlagen durch Umlosen (Ostwald Reifung). *Zeitschrift fur Electrochemie* **65**, 581–591.

Waychunas G. A, Ning Xu, Fuller C. C., Davis J. A., and Bigham J. M., (1995) XAS study of AsO_4^{3-} and SeO_4^{2-} substituted schwertmannites. *Physica B* **208/209**, 481–483.

Waychunas G. A., Kim C. S., and Banfield J. F. (2005) Nanoparticulate iron oxide minerals in soils and sediments: unique properties and contaminant scavenging mechanisms. *J. Nanopart. Technol.* **7**, 409–433.

Waychunas G., Davis J., and Reitmeyer R. (1999) Grazing-incidence EXAFS study of Fe^{3+} sorption on single crystal quartz substrates. *J. Synchrotron Radiation* **6**, 615–617.

Waychunas G. A., Myneni S. C. B., Traina S. J., Bigham J. M., Fuller C. F., and Davis J. A., (2001) Reanalysis of the schwertmannite structure and the incorporation of SO_4-Groups: an IR, XAS, WAXS and simulation study. Conference-abstract: Eleventh annual V.M. Goldschmidt Conference.

Waychunas G. A. (2001) Structure, aggregation and characterization of nanoparticles. In Nanoparticles and the environment, Vol. 44 (Eds. J. F. Banfield and A. Navrotsky), pp. 105–166. *Reviews in Mineralogy and Geochemistry*, Mineralogical Society of America, Washington, DC.

Waychunas G. A. (2002) Grazing-incidence x-ray absorption and emission spectroscopy. In *Applications of Synchrotron radiation in Low-Temperature Geochemistry and Environmental Science*, Vol. 49 (Eds. P. A. Fenter, M. L. Rivers, N. C. Sturchio and S. R. Sutton), pp. 267–316. *Reviews in Mineralogy and Geochemistry*, Mineralogical Society of America, Washington, DC.

Waychunas G. A., Rehr J. J., Fuller C. C., and Davis J. A (2003) Surface complexation and precipitate geometry for aqueous Zn(II) sorption on ferrihydrite: II. XANES analysis and simulation. *Geochim. Cosmochim. Acta* **67**, 1031–1043.

Weeks J. D. and Gilmer G. H. (1979) Dynamics of crystal growth. *Adv. Chem. Phys.* **40**, 157–228.

Weeks J. D., Gilmer G. H., and Jackson K. A. (1976) Analytical theory of crystal growth. *J. Chem. Phys*. **65**, 712–720.

Weeks, E. R., Crocker, J. C., Levitt, A. C., Schofield, A., Weitz, D. A., (2000) Three-dimensional direct imaging of structural relaxation near the colloidal glass transition. *Science* **287**(5453), 627–631.

Weitz D. A., Huang J. S., Lin M. Y., and Sung J. (1984) Dynamics of diffusion-limited kinetic aggregation. *Phys. Rev. Lett*. **53/17**, 1657–1660.

Weres O., Yee A., and Tsao L. (1981) Kinetics of silica polymerization. *J. Coll. Interf. Sci*. **84**, 379–402.

Whitesides G. M. and Grzybowski B. (2002) Self-assembly at all scales. *Science* **295**, 2418–2421.

Witten T. A. Jr. and Sander L. M. (1981) Diffusion-limited aggregation, a kinetic critical phenomenon. *Phys. Rev. Lett*. **47**, 1400–1403.

Wu D. T. (1997) Nucleation theory. *Solid State Phys.* **50**, 37–187.

Wulff G. (1901) Zur frage der geschwindigkeit des wachstums und der auflösung der kristallflachen. *Zeitschrift für Kristallographie* **34**, 449–530. (in German).

Wyss H. M., Huetter M., Mueller M., Meier L. P., and Gauckler L. J., (2002) Quantification of microstructures in stable and gelated suspensions from Cryo-SEM. *J. Coll. Interface Sci.* **248**, 340–346.

Yao J. H, Elder K. R., Guo G., and Gran M. (1993) Theory and simulation of Ostwald ripening. *Phys. Rev. B* **47**, 14110–14125.

Yund R. A. J., McLaren A. C. J., and Hobbs B. E. J. (1974) Coarsening kinetics of the exsolution microstructure in alkali feldspar. *Contrib. Min. Pet*. **48**, 45–55.

Zeldovich J. B. (1943) On the theory of new phase formation: cavitation. Zhur. Eksper. Teor. Fiz. **12** (1942), pp. 525ff (in Russian); *Acta Physicochim. URSS*, **18** (1943), pp. 1–22 (in English).

Zhu J., Chen L.-Q., Shen J., and Tikare V. (1999) Coarsening kinetics from a variable-mobility Cahn-Hilliard equation: Application of a semi-implicit Fourier spectral method. *Phys. Rev. E* **60**, 3564–3572.

Zhang H., Gilbert B., Huang F., and Banfield J. F. (2003) Water-driven structure transformation in nanoparticles at room temperature. *Nature* **424**, 1025–1029.